2009

AERODYNAMICS OF WIND BORNE PLATE DEBRIS

Bahareh Kordi

AERODYNAMICS OF WIND BORNE PLATE DEBRIS

(Thesis Format: Integrated-Article)

by:

Bahareh Kordi

Department of Civil and Environmental Engineering
Faculty of Engineering Science

A thesis submitted in partial fulfillment
of the requirements for the degree of
Doctor of Philosophy

The School of Graduate and Postdoctoral Studies
The University of Western Ontario
London, Ontario, Canada

THE UNIVERSITY OF WESTERN ONTARIO
THE SCHOOL OF GRADUATE AND POSTDOCTORAL STUDIES

CERTIFICATE OF EXAMINATION

Supervisor

Dr. Gregory A. Kopp

Examiners

Dr. Craig Miller

Dr. F. Michael Bartlett

Dr. Nusha Keyghobadi

Dr. Christopher Baker

The thesis by
Bahareh Kordi

Entitled

AERODYNAMICS OF WIND BORNE PLATE DEBRIS

is accepted in partial fulfillment of the
requirements for the degree of
Doctor of Philosophy

Date_____

Chair of the Thesis Examination Board

CO-AUTHORSHIP

- Parts of chapter 1 has been published, accepted for publication, and submitted for publication in the following papers:

  Kordi, B., and Kopp, G.A. (2009b). "Evaluation of the quasi-steady theory applied to windborne flat plates in uniform flow." *ASCE J. Eng. Mech.*, 135, No. 7, 657-668.

  Kordi, B., and Kopp, G.A. (2009c). "Effects of Initial Conditions on the Flight of Windborne Plate Debris." *J. Wind Eng. Ind. Aerodyn.* (submitted)

  Kordi, B., Traczuk, G., Kopp, G. A. (2009d). "Effects of wind direction on the flight trajectories of roof sheathing panels under high winds." *Wind and structures*, special issue on wind –borne debris. (accepted for publication)

- A version of chapter 2 has been published in the following paper:

  Kordi, B., and Kopp, G.A. (2009b). "Evaluation of the quasi-steady theory applied to windborne flat plates in uniform flow." *ASCE J. Eng. Mech.*, 135, No. 7, 657-668.

- Parts of chapter 3 has been accepted and submitted for publication in the following papers:

  Kordi, B., and Kopp, G.A. (2009c). "Effects of Initial Conditions on the Flight of Windborne Plate Debris." *J. Wind Eng. Ind. Aerodyn.* (submitted)

Kordi, B., Traczuk, G., Kopp, G. A. (2009d). "Effects of wind direction on the flight trajectories of roof sheathing panels under high winds." *Wind and structures*, special issue on wind –borne debris. (accepted for publication)

- A version of chapter 4 has been submitted for publication in the following paper:

  Kordi, B., and Kopp, G.A. (2009c). "Effects of Initial Conditions on the Flight of Windborne Plate Debris." *J. Wind Eng. Ind. Aerodyn.* (submitted)

- A version of chapter 5 has been accepted for publication in the following paper:

  Kordi, B., Traczuk, G., Kopp, G. A. (2009d). "Effects of wind direction on the flight trajectories of roof sheathing panels under high winds." *Wind and structures*, special issue on wind –borne debris. (accepted for publication)

  Note: In this paper, the results of the experiments conducted by Traczuk (2007) were re-examined.

- Parts of chapter 6 have been accepted and submitted for publication in the following papers:

  Kordi, B., and Kopp, G.A. (2009c). "Effects of Initial Conditions on the Flight of Windborne Plate Debris." *J. Wind Eng. Ind. Aerodyn.* (submitted)

  Kordi, B., Traczuk, G., Kopp, G. A. (2009d). "Effects of wind direction on the flight trajectories of roof sheathing panels under high winds." *Wind and structures*, special issue on wind –borne debris. (accepted for publication)

ACKNOWLEDGEMENT

I would like to gratefully thank Dr. Gregory A. Kopp for giving me the opportunity to work in his group, for guiding me to the appropriate direction, and for having endless patience, and providing unlimited support.

Financial support for this work was provided by the Institute for Catastrophic Loss Reduction, the Natural Sciences and Engineering Research Council (Canada), and the University of Western Ontario. Some of the equipments were provided through grants from the Canada Foundation for Innovation and the Ontario Innovation Trust.

The experimental part of this work was sponsored by Applied Research Associates. I gratefully acknowledge many useful insights brought into the work by Drs. L. Twisdale and P.J. Vickery.

I would like to express thanks to all of my colleagues and friends for their kindness and support. I would also like to thank the Alan G. Davenport Wind Engineering group at the University of Western Ontario for their generous contribution during the wind tunnel experiments.

I would like to express my affectionate appreciation to my family for their unwavering faith and continuous support during my long academic education. I would like to specially thank my husband, Saeed, for his unlimited support and patience.

TABLE OF CONTENTS

LIST OF TABLES

LIST OF FIGURES

LIST OF APPENDICES

LIST OF SYMBOLS

A	plate area, $l \cdot B$;
AR	aspect ratios, B/l
B	width of plate perpendicular to flow (span);
C_{DS}	static drag coefficient;
$\bar{C}_{DS}$	mean static drag coefficient over every half revolution;
C_{DR}	rotational drag coefficient;
C_{DR0}	mean drag coefficient at the point of stable autorotation;
C_{LS}	static lift coefficient;
C_{LR}	rotational lift coefficient;
C_{LR0}	mean lift coefficient at the point of stable autorotation;
C_{MS}	static moment coefficient;
C_{MR}	rotational moment coefficient;
$\bar{C}_M$	average moment coefficient over every half revolution;
C_N	static normal force coefficient on the plate;
c	plate center of pressure;
D	drag force;
d	distance between houses in one row;
Fr	Froud Number;
g	gravitational acceleration;
h	plate thickness;
I	plate mass moment of inertia, $m \cdot (l^2+h^2)/12$;

I^*	non-dimensional mass moment of inertia of a plate, $32\ I/(\pi.\rho_f.l^4.B)$;
I'	fixture strength integrity
k_{MR}	rotational pitching moment constants;
k'_{MR}	anti-rotational pitching moment constants;
L	lift force;
L_{House}	length of the house;
L_x	streamwise integral length scale of the boundary layer flow;
l	length of plate parallel to flow (chord);
M	pitching moment;
m	plate mass;
S	spin parameter (tip speed ratios of the plate), $\omega \cdot l/(2U_{rel})$;
S_0	spin parameter of the plate at the point of stable autorotation, $\omega_0 \cdot l/(2U_{rel})$;
T	integral time scale of the boundary layer flow;
t	flight time;
$\bar{t}$	non-dimensional flight time;
t_g	gust duration;
t_r	response time of the debris;
Ta	Tachikawa Number, $1/\Omega$;
U_w	horizontal wind velocity;
U_{ref}	horizontal mean wind velocities at the reference height;
U_H	horizontal mean wind velocities at mean roof height;
$U_{H,gust}$	gust wind speed at the mean roof height that the debris is flying with;

$\hat{U}_H$	horizontal failure wind velocity;
$\hat{U}_{3sec}$	ratio of 3-sec gust speeds to the hourly mean wind speed;
$\hat{U}_{600sec}$	ratio of 600-sec gust speeds to the hourly mean wind speed;
U_{rel}	relative wind velocity, $((U_w-u)^2+(V_w-\mathrm{v})^2)^{0.5}$;
$\bar{U}_{rel}$	non-dimensional relative wind velocity;
u	horizontal plate velocity;
$\bar{u}$	non-dimensional horizontal plate velocity;
$\bar{u}_{asymptotic}$	non-dimensional asymptotic horizontal plate velocity;
u_{mag}	magnitude of plate velocity, $\sqrt{u^2+\mathrm{v}^2+w^2}$;
$\bar{u}_{mag}$	non-dimensional magnitude of plate velocity;
$u_{mag\text{-}eave}$	magnitude of plate velocity at the eave height;
$\bar{u}_{mag\text{-}eave}$	non-dimensional magnitude of plate velocity at the eave height;
$u_{mag\text{-}ground}$	magnitude of plate velocity at the ground level;
$\bar{u}_{mag\text{-}ground}$	non-dimensional magnitude of plate velocity at the ground level;
V_w	vertical wind velocity;
v	vertical plate velocity;
$\bar{\mathrm{v}}$	non-dimensional vertical plate velocity;
$\bar{\mathrm{v}}_{\mathrm{asymptotic}}$	non-dimensional asymptotic vertical plate velocity;
w	lateral plate velocity;
X	horizontal (longitudinal) impact location of the debris;
x	horizontal plate displacement;

$\bar{x}$	non-dimensional plate horizontal displacement, $x \cdot \phi / l$;
y	vertical plate displacement;
$\bar{y}$	non-dimensional plate vertical displacement, $y \cdot \phi / l$;
$\bar{y}_{eave}$	non-dimensional eave height;
$\bar{y}_{ridge}$	non-dimensional ridge height;
Z	lateral impact location of the debris;
z	lateral plate displacement;
z_o	aerodynamic roughness length of the boundary layer simulation;
α	angle of attack of the relative wind velocity to the plate;
β	angle of attack of the relative wind with respect to the horizontal axis;
Δ	plate inertia, $m \cdot l^2 / I$;
δ_{max}	end deflection of a cantilever beam;
ϕ	buoyancy parameter, $0.5 \rho_f \cdot A \cdot l / m$;
λ_F	force scale;
λ_L	length scale;
λ_m	mass scale;
λ_ρ	density scale;
λ_v	velocity scale;
ρ_f	fluid density;
ρ_{air}	air density;
ρ_p	plate density;

τ	thickness ratios, h/l;
θ	plate angular rotation;
θ_0	initial plate angular rotation;
$\bar{\theta}$	non-dimensional plate angular rotation, $\theta . \phi$;
Ω	weight coefficient, $m \cdot g/(0.5 \rho_f \cdot A \cdot U_w^2)$;
ω	angular plate velocity;
ω_0	angular plate velocity at the point of stable autorotation;
$\bar{\omega}$	non-dimensional angular plate velocity, $\omega \cdot l / U_w$;
$\bar{\omega}_{\text{asymptotic}}$	non-dimensional asymptotic angular plate velocity;

1 INTRODUCTION

Windborne debris is a major cause of damage in strong wind events. Following wind-induced failures, building components (or portions of components) can fly through the air like missiles and penetrate adjacent, otherwise safe, structures. When debris breaches a building envelope, this can lead to significant internal pressures and greatly increased the net loading (Kopp et al., 2008), which can cause subsequent failures (e.g., Minor, 1994; Sparks et al., 1994; Leitch et al., 2007). One such example is shown in Fig. 1.1 where tiles from one house have impacted the roof of a neighbouring house. This has recently led to an increased interest in the aerodynamic aspects of windborne debris.

(a) (b)

Fig. 1.1: Photographs of (a) roof tile failures caused by a hurricane, and (b) impact damage on a roof due to tile impacts (courtesy of Dr. Tim Reinhold).

Roofing materials such as gravel, shingles, tiles, sheathing and structural members (such as 2x4s) are the most common sources of windborne debris. Information pertaining to "how far" and "how fast" windborne debris travels are two of the most important issues to be addressed, since these are directly related to the probability of downstream structures being hit and the probability of failure due to impact when they do hit.

Therefore, such information is critical for the development of vulnerability models and appropriate test standards for impact tests. Fig. 1.2 shows a typical example of flight for 4ft by 4ft plywood sheet, which in this case travelled about 450 m in a downburst in southern Ontario, Canada, illustrating the potential for widespread consequences in suburban neighbourhoods.

Fig. 1.2: Photograph of roof sheathing, caused by a downburst in Bornham, Ontario. The source of the plywood sheathing is the house shown in the background, almost 0.5 km away.

While damage surveys following severe storms occur routinely, there is limited knowledge of the distribution of flight distances from known debris sources. In addition, debris speeds have never been directly measured for hurricanes, although they have been observed (to a limited extent) for large elements from video evidence in tornadoes. Thus, there is a real lack of data from which to develop risk/loss models, impact speed test criteria, and building code requirements. This is why having experimental results and proper numerical models to predict the flight trajectory of wind borne debris become essential.

Amongst the first research on the flight of wind borne debris was the seminal work by Tachikawa (1983) who illustrated the complexity of the problem by showing that in a

smooth, uniform flow many different flight patterns resulted simply by changing the initial angle of attack at release. In particular, he observed that autorotational, translational and intermediate (with alternating directions of rotation) modes of flight are possible for rectangular plates in two-dimensional motion. Tachikawa (1983) used these different modes of flight as a means of estimating the variability of flight trajectories in real storms. He also modeled the aerodynamic forces as the sum of a static component (which is dependent on angle of attack) and an autorotational (or Magnus) component (which is proportional to the rotational speed), by using the quasi-steady method. He showed that the key non-dimensional group is what is now called the Tachikawa number (Holmes et al. 2006b).

This "basic approach" presented by Tachikawa has been the common method used in much subsequent research. Wills et al. (2002) categorized wind borne debris into three groups by shape and aerodynamic properties: compact (e.g., rocks), plate-like (e.g., plywood sheets or shingles), and rod-like (e.g., 2 by 4 lumber). He also discussed the effects of initial holding forces on both the speed and the total distance an element will fly via the important concept of the "fixture strength integrity". Lin et al. (2006), examined the flight trajectories and speeds of a wide range of plate sizes and densities released into a uniform smooth wind flow. Holmes et al. (2006a) presented a model of the force coefficients to solve the two-dimensional equations of motion by the quasi-steady theory. They found that the autorotational lift force induced by the Magnus effect has a considerable effect on the flight trajectory, but ignored the rotational drag and rotational moments which Tachikawa had originally included. Baker (2007) also studied the flight trajectory of plates computationally, but with a greater focus on the non-

dimensionalization of the equations, the asymptotic solutions, and the sensitivity to initial conditions. He also considered the effect of the autorotational moment coefficient caused by the Magnus effect, using information from Iversen's analysis of autorotation data which showed that there is an asymptotic limit to the rotational speed.

Such works have been used to develop criteria for debris impact speeds and in the development of risk or loss models for hurricanes such as HAZUS (ARA, 2002; Vickery et al., 2006 a, b). However, the "basic approach" presented by Tachikawa (1983) cannot fully help us understand the real situation because it ignores two important facts: (i) windborne debris initiating from a real roof must be affected by the building aerodynamics and the local velocities on the roof, and (ii) the debris flies in the turbulent wind defined by the terrain and gust structure causing failure.

To begin to address this, Visscher and Kopp (2007), using the 'failure' model concept of Surry et al. (2005), examined the flight trajectories of aeroelastically-scaled sheathing panels, mounted on the roof of a low-rise building model in a scaled atmospheric boundary layer. They studied the flight of a 1.2m by 2.4m (equivalent full-scale) plywood panel from a single location on the roof, near the ridge of the leeward roof surface, for one wind direction. Electromagnets were used to provide the hold down force of the nails. Their results showed that all of the possible modes of flight observed by Tachikawa can occur from the same nominal initial conditions when the plate is mounted on a building surface and fails under turbulent wind loads. This was shown to have significance since the mode of flight dramatically altered the typical flight distances and speeds. In particular, when autorotation occurred, the flight distance was enhanced by the

additional lift caused by the plate rotation when compared to plates which simply translated and fell in the wake of the house.

In Chapter 2 of this work, the quasi-steady model will be evaluated for windborne flat plates, taking into account the more recent fundamental research into the aerodynamics of autorotation and falling paper, as well as Lin et al.'s (2006) extensive data set. This is because, aside from Tachikawa's analysis of his own experimental data, there has been limited justification for the use of the quasi-steady model to numerically predict the flight of the debris. In fact, papers on autorotation (Lugt 1980) and two-dimensional falling plates (Andersen et al. 2005) offer significant criticisms of the quasi-steady theory, which may be relevant to windborne flight of plates. This will allow the limits of the theory to be determined, which may ultimately be important for the accuracy of such models for computations of debris flight originating from realistic initial conditions on building surfaces in the turbulent atmospheric boundary layer.

Following that the flight of three common forms of debris, namely roof tiles, asphalt shingles, and sheathing panels, which are all critical in residential neighbourhoods during hurricanes, will be examined. It is important to realize the initial conditions are set by the building aerodynamics, while the flight immediately following failure is dependent on the aerodynamics of the debris element and the local velocity field. For a global roof failure, these are one and the same (at least for the initial stages of flight), but for sheathing panels, tiles, and shingles there is a clear distinction between the flow above the roof, the surface pressure fields causing failure, and the local aerodynamics governing flight.

Thus, there are many open questions pertaining to the flight of wind borne debris. The experimental setup will be described in Chapter 3. The experimental results on the flight of roof tiles and shingles will be presented in Chapter 4 and in Chapter 5 the sheathing panel experiments conducted by Traczuk(2007) will be re-examined.

What is also missing is knowledge of the flow field in which the debris flies. In other words, we do not know the actual aerodynamic forces controlling the flight since we do not have the velocity field that the debris flies in. Therefore, the relation between the uniform flow modelling and actual situations is not clear. In addition, the role of turbulence has not been explored to any significant extent by researchers yet, both in terms of overall flight distances and speeds, where, for the latter, it has been explicitly assumed that debris flies with the gust since flight durations are expected to be short compared to the typical duration of gusts (Lin et al., 2007). This assumption has not been investigated, although it could have a significant effect on actual flight speeds and distances. Holmes (2004) examined potential effects on flight trajectories using a simulated (numerical) turbulent field for the flight of spheres and found that, while turbulence increased the scatter in flight distance, he argued that it did not have significant effect on the mean trajectories for these objects. However, this assumption neglects potential effects of gust variation and turbulence on the initial flight conditions. Gusts, and the resulting induced peak pressures, are clearly associated with failures, but they have significant variation. One can imagine that for a strong and long duration gust, the debris, if it is sufficiently responsive (e.g., light), has a chance to move within the gust. In contrast, for shorter duration gusts or less responsive (e.g., heavy) debris, the gust

may pass and the flight occurs in the lower speed flow following the gust. Such turbulence effects will be examined in the Chapter 6.

The work described in this thesis has been published in Kordi and Kopp (2009a,b) where the numerical model were developed and in Kordi and Kopp (2009c,d) where the experimental results and their comparison with numerical models have been performed.

References

Andersen, A., Pesavento, U., and Wang, Z. J. (2005). "Unsteady Aerodynamics of fluttering and tumbling plates." *J. Fluid Mech.* 541, 65-90.

Applied Research Associates, Inc.. HAZUS Wind Loss Estimation Methodology – Volume I. North Carolina, October 2002.

Baker, C.J. (2007). "The debris flight equations." *J. Wind Eng. Ind. Aerodyn.* 95, 329-353.

Holmes, J.D. (2004). "Trajectories of spheres in strong winds with application to wind-borne debris." *J. Wind Eng. Ind. Aerodyn.*, 92, 9-22.

Holmes, J.D., Letchford, C.W., and Lin, N. (2006a). "Investigations of plate-type windborne debris- Part II : Computed trajectories." *J. Wind Eng. Ind. Aerodyn.* 94, 21-39.

Holmes, J.D., Baker, C.J., and Tamura, Y. (2006b). "Tachikawa number: a proposal." *J. Wind Eng. Ind. Aerodyn.* 94, 41-47.

Kopp, G.A., Oh, J.-H., and Inculet, D.R. (2008). "Wind-induced internal pressures in houses." *ASCE J. Struct. Eng.* 134, 1129-1138.

Kordi, B., and Kopp, G.A. (2009a). "Discussion "The debris flight equations" by C.J. Baker." *J. Wind Eng. Ind. Aerodyn.*, 97, 151-154.

Kordi, B., and Kopp, G.A. (2009b). "Evaluation of the quasi-steady theory applied to windborne flat plates in uniform flow." *ASCE J. Eng. Mech.*, 135, No. 7, 657-668.

Kordi, B., and Kopp, G.A. (2009c). "Effects of Initial Conditions on the Flight of Windborne Plate Debris." *J. Wind Eng. Ind. Aerodyn.* (submitted).

Kordi, B., Traczuk, G., Kopp, G. A. (2009d). "Effects of wind direction on the flight trajectories of roof sheathing panels under high winds." *Wind and structures*, special issue on wind –borne debris. (accepted for publication)

Leitch, C.J., Ginger, J.D., Henderson, D.J., Boughton, G.N. (2007). "Tropical Cyclone Larry: Estimation of Wind Field and Assessment of Building Damage." *Aust. J. Struct. Eng.* 7, 209-224.

Lin, N., Letchford, C., and Holmes, J.D. (2006). "Investigation of plate-type windborne debris. Part I. Experiments in wind tunnel and full scale." *J. Wind Eng. Ind. Aerodyn.* 94, 51-76.

Lin, N., Holmes, J.D. and Letchford, C. (2007). "Trajectories of Wind-Borne Debris in Horizontal Winds and Applications to Impact Testing." *ASCE J. Struct. Eng.* 133, 274-282.

Lugt, H. J. (1980). "Autorotation of an elliptic cylinder about an axis perpendicular to the flow." *J. Fluid Mech.* 99, 817-840.

Minor, J.E. (1994). "Windborne debris and the building envelope." *J. Wind Eng. Ind. Aerodyn.* 53, 207-227.

Sparks, P.R., Schiff, S.D., and Reinhold, T.A. (1994). "Wind damage to envelopes of houses and consequent insurance losses." *J. Wind Eng. Ind. Aerodyn.* 53, 145-155.

Surry, D., Kopp, G.A., Bartlett, F.M. (2005). "Wind load testing of low buildings to failure at model and full scale." *ASCE Natural Hazards Review*, 6, 121-128.

Tachikawa, M. (1983). "Trajectories of flat plates in uniform flow with application to wind-generated missiles." *J. Wind Eng. Ind. Aerodyn.* 14, 443–453.

Traczuk, G. (2007). "Trajectories of roof sheathing panels under high winds." Undergraduate thesis, The University of Western Ontario, Canada.

Vickery, P. J., Lin, J. X., Skerlj, P. F., Twisdale, L. A., and Huang, K. (2006a). "HAZUS-MH hurricane model methodology. I: Hurricane hazard, terrain and wind load modeling." *Nat. Hazards Rev.*, 7(2),82–93.

Vickery, P. J., Skerlj, P. F., Lin, J. X., Twisdale, L. A., Young, M. A., and Lavelle, F. M. (2006b). "HAZUS-MH hurricane preview model methodology. II: Damage and loss estimation." *Nat. Hazards Rev.*, 7(2),94–103.

Visscher, B.T., and Kopp, G.A. (2007). "Trajectories of roof sheathing panels under high winds." *J. Wind Eng. Ind. Aerodyn.*, 95, 697-713.

Wills, J.A.B., Lee, B.E., and Wyatt, T.A. (2002). "A model of wind-borne debris damage." *J. Wind Eng. Ind. Aerodyn.* 90, 555-565.

2 EVALUATION OF THE QUASI-STEADY MODEL APPLIED ON THE DEBRIS FLIGHT EQUATIONS

2.1 Equations of Motion

Applying Newton's second law and the quasi-steady theory to the two-dimensional motion of a plate, together with the definitions given in Fig. 2.1, the dimensional equations of motion are

$$\frac{d^2x}{dt^2} = \left(\frac{A \cdot \rho_f}{2\,m}\right)\left[(C_{DS} + C_{DR})(U_w - u) - (C_{LS} + C_{LR})(V_w - \mathrm{v})\right] \cdot U_{rel} \tag{2.1a}$$

$$\frac{d^2y}{dt^2} = \left(\frac{A \cdot \rho_f}{2\,m}\right)\left[(C_{DS} + C_{DR})(V_w - \mathrm{v}) + (C_{LS} + C_{LR})(U_w - u)\right] \cdot U_{rel} - \frac{(\rho_p - \rho_f)}{\rho_p} g \tag{2.1b}$$

$$\frac{d^2\theta}{dt^2} = \left(\frac{A \cdot l \cdot \rho_f}{2\,I}\right).(C_{MS} + C_{MR}) \cdot U_{rel}^2 \tag{2.1c}$$

where, throughout the study, x = horizontal plate displacement; y = vertical plate displacement; θ = angular rotation; t = flight time; l = length of plate parallel to flow (chord); B = width of plate perpendicular to flow (span); h = plate thickness; U_w = horizontal wind velocity; V_w = vertical wind velocity; u = horizontal plate velocity; v = vertical plate velocity; ω = angular plate velocity; D = drag force on the plate; L = lift force, M = pitching moment; C_{DS} = static drag coefficient; C_{DR} = rotational drag coefficient; C_{LS} = static lift coefficient; C_{LR} = rotational lift coefficient; C_{MS} = static moment coefficient; C_{MR} = rotational moment coefficient; A = plate area, $l \cdot B$; ρ_p = plate density; m = plate mass; ρ_f = fluid density; I = plate moment of inertia, $m \cdot (l^2 + h^2)/12$; U_{rel} = relative wind velocity, $((U_w - u)^2 + (V_w - \mathrm{v})^2)^{0.5}$; α = angle of attack of the relative wind

velocity to the plate; β = angle of attack of the relative wind with respect to the horizontal axis; and, g = gravitational acceleration.

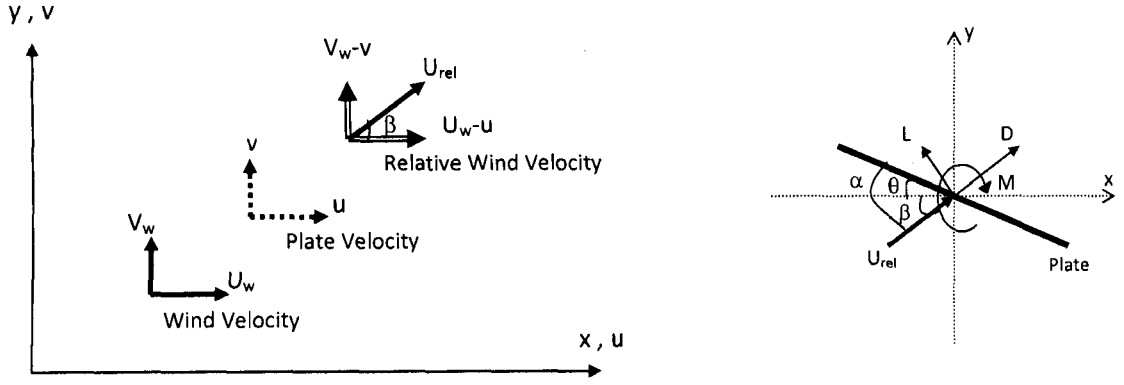

Fig. 2.1: Definition sketch showing the (a) wind velocity components and the (b) directions of forces and moments on the plate.

Following Baker (2007), the non-dimensional equations of motion are

$$\frac{d^2\bar{x}}{d\bar{t}^2} = \left((C_{DS} + C_{DR})(1-\bar{u}) - (C_{LS} + C_{LR})(\bar{V}_w - \bar{v})\right)\cdot \bar{U}_{rel} \tag{2.2a}$$

$$\frac{d^2\bar{y}}{d\bar{t}^2} = \left((C_{DS} + C_{DR})(\bar{V}_w - \bar{v}) + (C_{LS} + C_{LR})(1-\bar{u})\right)\cdot \bar{U}_{rel} - (1-\frac{\rho_f}{\rho_p})\,\Omega \tag{2.2b}$$

$$\frac{d^2\bar{\theta}}{d\bar{t}^2} = \Delta.(C_{MS} + C_{MR})\cdot \bar{U}_{rel}^2 \tag{2.2c}$$

where the non-dimensional parameters are: $\Omega = m{\cdot}g/(0.5\rho_f{\cdot}A{\cdot}U_w^2)$, where $Ta = 1/\Omega$ is the Tachikawa number; buoyancy parameter, $\phi = 0.5\rho_f \cdot A{\cdot}l/m$; plate inertia, $\Delta = m{\cdot}l^2/I$; horizontal displacement, $\bar{x} = x{\cdot}\phi/l$; vertical displacement, $\bar{y} = y{\cdot}\phi/l$; angular rotation, $\bar{\theta} = \theta{\cdot}\phi$; time, $\bar{t} = t{\cdot}U_w{\cdot}\phi/l$; horizontal plate velocity, $\bar{u} = u/U_w$; vertical plate velocity, $\bar{v} = v/U_w$; angular plate velocity, $\bar{\omega} = \omega{\cdot}l/U_w$; relative wind velocity, $\bar{U}_{rel} = U_{rel}/U_w$. If the

fluid is air, the ratio, ρ_f/ρ_p, can be neglected in Eq. (2.2) for typical plates of relevance for windborne debris.

There has not been consensus on the role of the rotational coefficients and some authors have only included the lift coefficient, C_{LR}, (e.g., Holmes et al. 2006) while others have included all three coefficients (e.g., Tachikawa 1983). In the following sections, the role of these coefficients from the existing literature will be examined, including both two-dimensional and three-dimensional plates for the cases of windborne debris, falling paper and single-degree-of-freedom autorotating plates, and based on this, develop a model suited to the problem of 3D windborne plates in uniform flow.

2.1.1 Two-dimensional plates

2.1.1.1 Autorotation

Autorotation has been studied for some time as a basis for understanding unsteady problems in aerodynamics, such as dynamic stall. Typically, autorotation has been idealized experimentally as a single degree of freedom (rotational) system to study onset of autorotation, tip speed ratios and force coefficients. The research has focused on several aspects but two are of particular relevance here, viz., the asymptotic limit of the rotational speed as a function of plate geometry, and the aerodynamic forces. Smith (1971) and Iversen (1979) examined three-dimensional (3D) plates, while Lugt (1980, 1983) and Skews (1990) examined two-dimensional (2D) plates.

Lugt (1980) solved the Navier-Stokes equations for the flow around a two-dimensional thin elliptical cylinder fixed perpendicular to a parallel flow for different tip speed ratios (spin parameter), $S = \omega \cdot l/(2U_{rel})$. He found the spin parameter at the point of

stable autorotation, S_0, of 0.45, a value in good agreement with Skews' (1990) experimental data. Lugt's work showed that when the spin parameter, S, is smaller than the spin parameter at the point of stable autorotation, S_0, vortex shedding leads to an aerodynamic moment in favour of rotation but once the spin parameter exceeds S_0, vortex shedding leads to an aerodynamic moment which damps the rotation. Stable autorotation occurs when the average moment coefficient, $\overline{C}_M$, over every half revolution, is equal to zero (Lugt 1980). Rotational overspeeding, so that $S > S_o$, in single degree of freedom experiments has not been reported.

Skews (1990) conducted experiments on autorotating 2D plates with thickness ratios, $\tau = h/l$, in the range of 0.1 – 1. He found that, at the point of stable autorotation, the spin parameter, S_0, and the mean drag coefficient, C_{DR0}, of 2D plates are independent of thickness ratio. However, the mean lift force coefficient at the point of stable autorotation, C_{LR0}, is dependent on the plate thickness.

2.1.1.2 Falling Plates

Tachikawa (1983) found that the flight of rectangular plates in cross flow is sensitive to the initial angle of attack with different modes of rotation being observed. These included an autorotational mode, a translational mode and, what he termed an intermediate mode, where the direction of rotation reversed during flight. When one examines these different modes of flight, the problem of falling paper is also brought to mind. This latter problem, first studied by Maxwell (1854), has been studied with renewed interest in recent years (Belmonte et al. 1998; Mahadevan et al. 1999; Pesavento and Wang 2004; Andersen et al. 2005; Pesavento 2006). In particular, the work of

Andersen et al. (2005) and Pesavento (2006) provide additional (2D) data which may prove useful in justifying the quasi-steady force and moment coefficients used in the flight of rectangular plate debris in a cross flow.

Andersen et al. (2005) studied four freely falling, 2D, thin, rigid plates in water, with aspect ratios, $AR = B/l$, between 17 and 31, and determined the instantaneous forces and velocities. They observed different behaviors, viz., fluttering, tumbling, and chaotic motion, the latter of which appears to be similar in many ways to Tachikawa's "intermediate" case.

The rotational speed is a critical parameter in the quasi-steady model since the autorotational portion of the forces depends on it directly. The instantaneous spin parameter, S, for cases of fluttering and tumbling plates has been assembled from Andersen et al.'s horizontal, vertical, and rotational velocities into the ratio of S, to the asymptotic value, S_0 (= 0.47) determined from Skews (1990). This is shown in Fig. 2.2. As can be seen, for the case of flutter, the spin parameter is greater than S_0 for a small proportion of each cycle. In contrast, for the case of tumbling, S exceeds S_0 much of the time with S/S_o having values of up to 5 during each cycle. Thus, significant rotational overspeeding, compared to single degree of freedom experiments, is a critical aspect of freely falling plates. This may also be important for wind-driven plates, a point which will be examined in greater detail below.

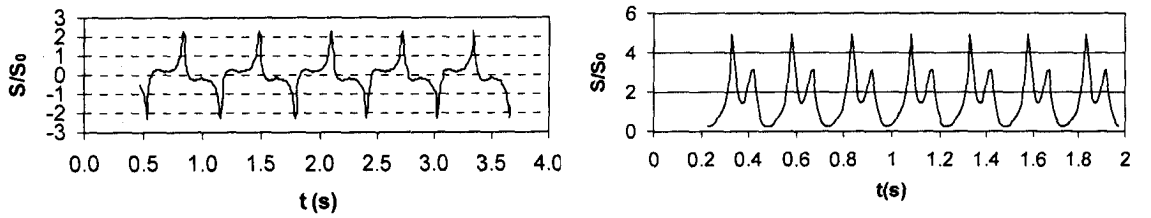

Fig. 2.2: Ratio of spin parameter, S, to the spin parameter at the point of stable autorotation, S_o, from Andersen et al.'s (2005) experiments for two-dimensional (a) fluttering and (b) tumbling plates.

2.1.2 Three-dimensional, rectangular plates

Tachikawa (1983) studied the flight trajectories of square and rectangular plates in a uniform flow both experimentally and numerically. He measured the aerodynamic forces applied on square and rectangular plates from rest to the point of stable autorotation using a single degree freedom (autorotational) experiment. He presented the two-dimensional equations of motion and employed the quasi-steady theory to predict the flight trajectory. A limitation of the single-degree-of-freedom experiment is that it does not allow for the instantaneous over-speeding of rotational motion, which is observed for two-dimensional falling plates, as discussed above.

Holmes et al. (2006) solved the two-dimensional equations of motion based on the quasi-steady theory by incorporating the static forces and moments as well as a rotational lift force. He obtained reasonable agreement between computed trajectories and the experimental work done by Lin et al. (2006), although a close examination of their model seems to indicate a systematic under-estimation of the horizontal plate speeds. Baker (2007) also studied the flight trajectory by adding the effects of both the rotational lift and

moment coefficient caused by the Magnus effect but imposed a constant maximum limit on the angular velocity of a square plate.

Iversen (1979) analyzed the wide range of experimental data available on the autorotation of plates in either free flight or in single-degree-of-freedom motion. He concluded that if the non-dimensional moment of inertia of a plate is large enough, roughly larger than 1, the spin parameter of a plate at the point of stable autorotation only depends on aspect ratio and thickness ratio. Using these observations, we present modified coefficients.

The static drag, lift, and pitching moment coefficients for a square plate, used herein are the same as those assumed by Holmes et al. (2006) based on their experiments and the earlier experiments by Flachsbart (1932), as reported by Hoerner (1965).

Building on the work of Tachikawa (1983), C_{DR} and C_{LR} are defined in terms of S/S_0 so that for a square plate,

$$C_{DR} = \begin{cases} 0.66\left|\dfrac{S}{S_o}\right| & \left|\dfrac{S}{S_o}\right| \le 0.4 \\ 0.12 + 0.36\left|\dfrac{S}{S_o}\right| & 0.4 < \left|\dfrac{S}{S_o}\right| < 1 \\ 0.48 & \left|\dfrac{S}{S_o}\right| \ge 1 \end{cases} \tag{2.3}$$

$$C_{LR} = \begin{cases} 0.1575 + 0.2625\dfrac{S}{S_o} & \dfrac{S}{S_o} \ge 0.2 \\ 1.05\dfrac{S}{S_o} & -0.2 < \dfrac{S}{S_o} < 0.2 \\ -0.1575 + 0.2625\dfrac{S}{S_o} & \dfrac{S}{S_o} \le -0.2 \end{cases} \tag{2.4}$$

where $S = \omega \cdot l/(2U_{rel})$ is the spin parameter (or tip speed ratio) of the plate, $S_0 = \omega_0 \cdot l/(2U_{rel})$ is the spin parameter of the plate at the point of stable autorotation, while ω_0

is the angular velocity of the plate at the point of stable autorotation. It should be mentioned that this model of the autorotational lift force coefficient is different from the previous model presented by Kordi and Kopp (2009). Here, it is not flattened after it has reached the point of stable autorotation, $S=S_0$, but rather is allowed to grow in the way Tachikawa presented it. This is consistent with the observations from two-dimensional falling plates, but with a change in slope at $S/S_0=0.2$. It is not clear why this change in slope occurs, but it appears to be a real factor in Tachikawa's data.

Then, building on the work of Tachikawa (1983), but incorporating Lugt's (1980) result, C_{MR} is defined in terms of S/S_0 for a square plate as

$$C_{MR}=\begin{cases} 0.12\left(1-\dfrac{S}{S_o}\right) & \dfrac{S}{S_o}>1 \\ 0.12\left(1-\left|\dfrac{S}{S_o}\right|\right)\dfrac{S}{S_o} & -1\le\dfrac{S}{S_o}\le 1 \\ -0.12\left(1+\dfrac{S}{S_o}\right) & \dfrac{S}{S_o}<-1 \end{cases} \tag{2.5}$$

Based on Iversen (1979), if the non-dimensional mass moment of inertia of a plate, $I^*=32\,I/(\pi.\rho_f.l^4.B)$, is larger than 1, S_0 of a three-dimensional (3D) plate is defined as

$$S_0=\left(0.329\ln\tau^{-1}-0.0246\left(\ln\tau^{-1}\right)^2\right)\left(\left[\frac{AR}{2+(4+AR^2)^{\frac{1}{2}}}\right]\left[2-\left(\frac{AR}{AR+0.595}\right)^{0.76}\right]\right)^{\frac{2}{3}} \tag{2.6}$$

Thus, the solution of plate trajectories via Eq. (2.2) depends on four independent non-dimensional parameters, Ω, ϕ, θ_0 (representing the initial conditions), and τ. The buoyancy parameter, ϕ, is embedded in the equations through the non-dimensionalization and does not appear explicitly. The thickness ratio, τ, has a direct effect on S_0 and Δ.

There can be other forms for the non-dimensional parameters such as Fr, ρ_f/ρ_P, θ_0, and τ, where

$$Fr = \frac{U_w}{\sqrt{g.l}} = \sqrt{\frac{1}{\Omega . \phi}} \tag{2.7}$$

Thus, to determine the trajectory of any plate or to compare the numerical results with the experimental results, all four parameters must be considered.

For an upstream horizontal wind velocity, where the fluid is air, it is possible to derive the asymptotic solutions to Eqs. (2.2, a-c)

$$\bar{u}_{asymptotic} = 1 \pm \left(\frac{\Omega}{C_{LR0}} \right)^{0.5} \left(1 + \frac{(\bar{C}_{DS} + C_{DR0})^2}{C_{LR0}^2} \right)^{-0.75} \tag{2.8a}$$

$$\bar{v}_{asymptotic} = -\left(\frac{\Omega}{C_{LR0}} \right)^{0.5} \left(\frac{\bar{C}_{DS} + C_{DR0}}{C_{LR0}} \right) \left(1 + \frac{(\bar{C}_{DS} + C_{DR0})^2}{C_{LR0}^2} \right)^{-0.75} \tag{2.8b}$$

$$\bar{\omega}_{asymptotic} = \mp 2\, S_0 . \bar{U}_{rel} = \mp 2\, S_0 \left(\frac{\Omega}{C_{LR0}} \right)^{0.5} \left(1 + \frac{(\bar{C}_{DS} + C_{DR0})^2}{C_{LR0}^2} \right)^{-0.25} \tag{2.8c}$$

where $\bar{C}_{DS}$ is the average static drag applied to a plate over a half cycle. Note that $\bar{\omega}$ is a function of $\bar{u}$ and $\bar{v}$ through $\bar{U}_{rel}$. For the case of a thin square plate, $\bar{C}_{DS}$ = 0.82, C_{DR0} = 0.48, and C_{LR0} = 0.42. This results in a simpler set of equations for square plates:

$$\bar{u}_{asymptotic} = 1 \pm 0.263\sqrt{\Omega} \tag{2.9a}$$

$$\bar{v}_{asymptotic} = -0.814\sqrt{\Omega} \tag{2.9b}$$

$$\bar{\omega}_{asymptotic} = \mp 1.748\ S_0 \sqrt{\Omega} \tag{2.9c}$$

It should also be noted that the asymptotic solutions presented in Eq. (2.8) are only applicable to wind-driven plates, not to falling plates, because of the way the velocities

are non-dimensionalized with the horizontal wind speed in the denominator. The asymptotic solution for windborne plate debris is equivalent to the point of stable autorotation since $\bar{u}$ and $\bar{v}$ are constant over a cycle when this point is reached.

2.2 Results for Square Plates in Uniform Flow

There are currently only two existing experimental databases for the flight of wind-driven plates in uniform flow with which to compare the current numerical model, namely, Tachikawa (1983) and Lin et al. (2006). The Lin et al. data is more comprehensive in that many different plates with many repeat runs were performed. However, these data are limited since no rotational speeds were recorded so that the performance of the autorotational portion of the empirical model can only be determined indirectly. Tachikawa (1983), on the other hand, provided a limited database, but the source data through stroboscopic images is available so that rotational frequencies can be inferred. So, to evaluate the current quasi-steady model, we will compare the numerical results with the trajectory data available in both papers. We will also examine the summary data presented by Lin et al. (2006), since there is undoubted variability in individual runs due to the strong sensitivity to initial conditions (Baker 2007).

Using the static and autorotational force coefficients defined above, Eq. (2.2) is solved using a 4^{th}-order Runge-Kutta scheme. Numerical results are compared with data from Tachikawa (1983) in Fig. 2.3 and Fig. 2.4. There is good agreement between our solutions and Tachikawa's, and in general, the best matches appear to be those cases with the lowest rotational speeds. The two cases with the highest observed rotational speeds

are shown in the figures. It should be emphasized that these are the worst matches between the current model and the data presented in his paper.

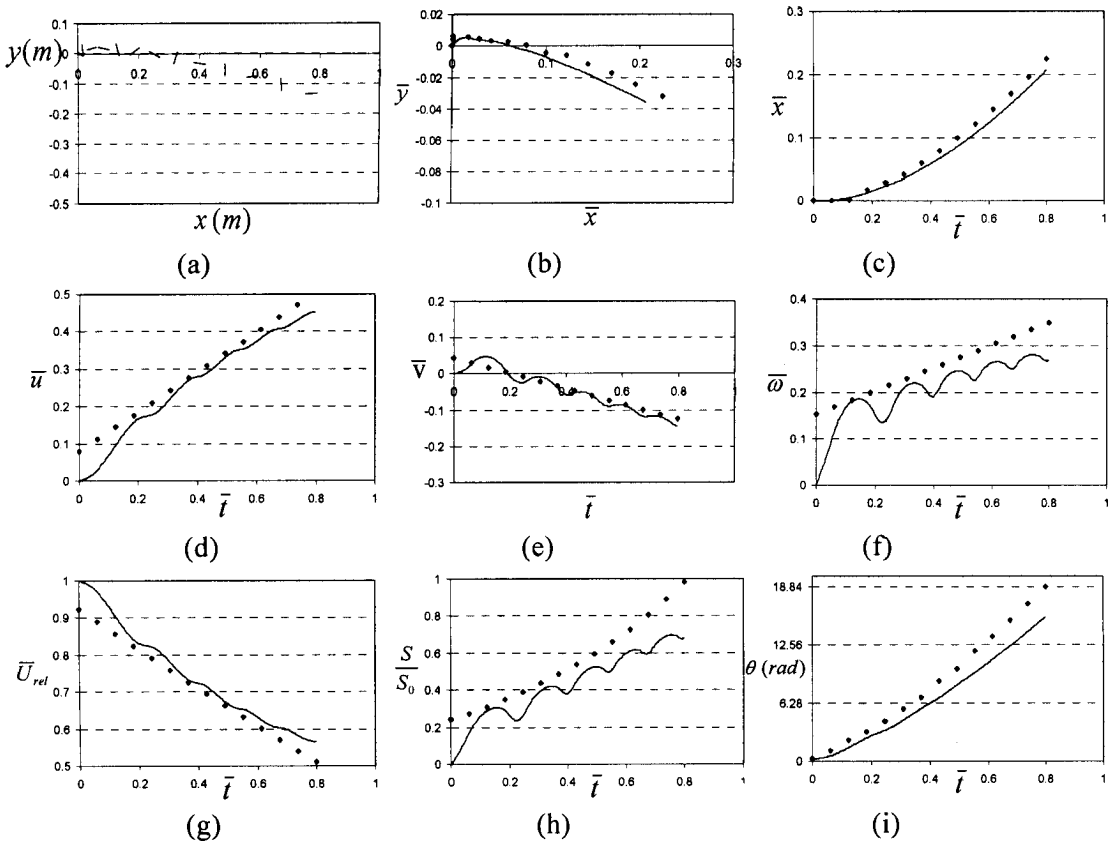

Fig. 2.3: Comparison between Tachikawa recordings and the computed trajectory for a square plate with l=B=4cm, h=2mm, ρ_p=1120 Kg/m^3, U_w=9.18 m/s, and θ_0=15°, (a) computed dimensional trajectory, (b) non-dimensional trajectory, (c) non-dimensional horizontal distance vs. non-dimensional time, (d) non-dimensional horizontal velocity vs. non-dimensional time, (e) non-dimensional vertical velocity vs. non-dimensional time, (f) non-dimensional rotational velocity vs. non-dimensional time, (g) non-dimensional relative velocity vs. non-dimensional time, (h) ratio of spin parameter to the spin parameter at the point of stable autorotation, S_0, vs. non-dimensional time, (i) angular displacement vs. non-dimensional time. Symbol, ♦, shows the data obtained from the Tachikawa recordings, and , _____, shows the numerical solutions.

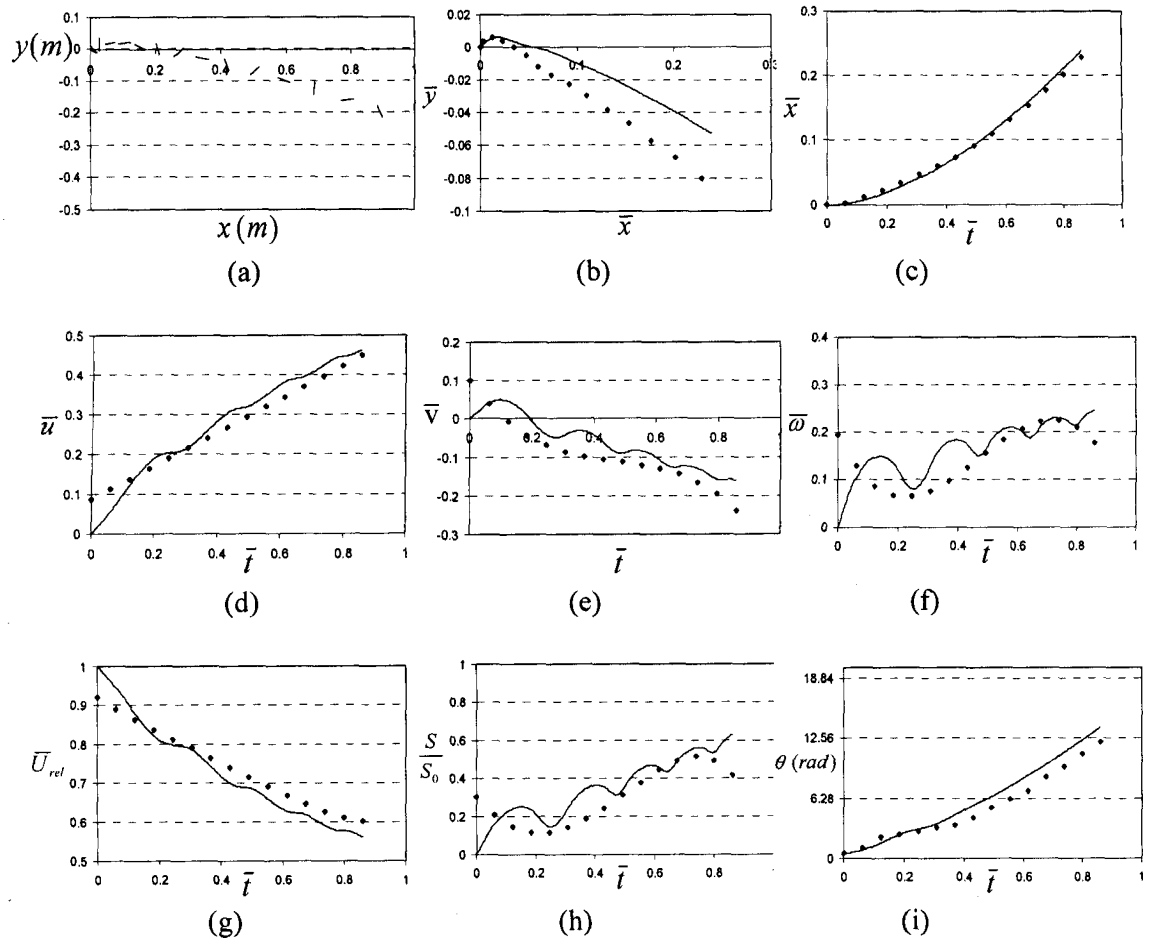

Fig. 2.4: Comparison between Tachikawa recordings and the computed trajectory for a square plate with l=B=4cm, h=2mm, ρ_p=1120 Kg/m^3, U_w=9.18 m/s, and θ_0=30°, (a) computed dimensional trajectory, (b) non dimensional trajectory, (c) non-dimensional horizontal distance vs. non-dimensional time, (d) non-dimensional horizontal velocity vs. non-dimensional time, (e) non-dimensional vertical velocity vs. non-dimensional time, (f) non-dimensional rotational velocity vs. non-dimensional time, (g) non-dimensional relative velocity vs. non-dimensional time, (h) ratio of spin parameter to the spin parameter at the point of stable autorotation, S_0, vs. non-dimensional time, (i) angular displacement vs. non-dimensional time. Symbol, ♦, shows the data obtained from the Tachikawa recordings, and , _____, shows the numerical solutions.

Fig. 2.3(b) shows that the numerical results fall below the experimental trajectory (x-y plane) for $\theta_o = 15^\circ$, while for $\theta_o = 30^\circ$, Fig. 2.4(b) shows that the numerical is above the experimental. This is due to slightly low horizontal speeds for the former and slightly high horizontal and vertical plate speeds for the latter. The rotational speeds in both of these cases are similar and it is interesting to observe that for $\theta_o = 15^\circ$, the net rotation (Fig. 2.3i) is slightly high in the numerical calculation, while for $\theta_o = 30^\circ$, the net rotation is slightly low (Fig. 2.4i). Given that this seems to be contrary to the overall trajectories for $S < S_o$, one can conclude that the rotational speed is not the main driver for the plate trajectories; rather, the horizontal and vertical velocities seem to be of greater importance for obtaining accurate trajectories. This makes sense, considering Eq. (2.2), where the x and y motion depends explicitly on both the drag and lift, and only implicitly on the rotation (through the effects of the instantaneous angle of attack on the static lift and drag and the rotational speed on the rotational lift and drag). In any case, the agreement between the computed and observed data is excellent, except perhaps for $\theta_o = 30^\circ$, where the trajectory is substantially in error (although the plate speeds are reasonable).

Holmes et al. (2006) also compared their model with Tachikawa's data for the case of $\theta_0 = 45^\circ$ and found excellent agreement, but their model did not consider the effect of $\overline{U}_{rel}$ correctly in their definition of ω_0. If we modify their model of rotational lift force coefficient by adding the effect of $\overline{U}_{rel}$ on the definition of ω_0, the model no longer shows such close agreement. Since aerodynamic forces are dependent on relative wind speeds, this is quite important.

Comparisons between computed trajectories and selected experimental results from Lin et al. (2006) are shown in Fig. 2.5. The effects of rotational lift, rotational pitching moment, and rotational drag are added to the model incrementally in Fig. 2.5 in order to observe the effects of these terms. When comparing with Holmes et al. (2006), the current model yields generally better accuracy than the previous models since the rotational moment and drag coefficients have considerable effects on the plate trajectory and translational plate speeds. However, these effects change with initial conditions making definitive statements difficult. For example, examining the trajectories in Fig. 2.5(a, d, g), one observes differing effects for the three rotational coefficients. In some cases, C_{DR} causes a higher trajectory (Fig. 2.5a) while in others a lower trajectory (Fig. 2.5d and Fig. 2.5g). This is somewhat clarified by the remaining figures which show that rotational drag plays an important role in the speed of the plates, allowing a much better estimation of both the plate speed and horizontal trajectory (x) with time, when compared to the experimental data. The increased horizontal speed directly caused by the rotational drag seems to flatten the trajectories so that falling plates fall less rapidly (Fig. 2.5a) and rising plates rise less rapidly (Fig. 2.5d and Fig. 2.5g), offsetting the effects of the rotational moment, C_{MR}. Thus, inclusion of the autorotational drag is important to the fidelity of the simulations.

As mentioned above, Lin et al. (2006) performed a considerable number of experiments on a range of plates. They derived an empirical expression, fit through the center of their data set, to estimate the typical non-dimensional plate speeds as a function of non-dimensional distance traveled. Eq. (2.4) of Lin. et al. (2006) can be written in the current notation as

$$\bar{u} \approx 1 - \exp(-\sqrt{1.8\,\bar{x}}\,) \tag{2.10}$$

The majority of Lin et al.'s (2006) experiments were conducted on square plates with 0^o initial angle of attack, with Ω between 0.03 and 0.45. The thickness ratio, τ, and the buoyancy parameter, ϕ, for most of the plates were between 0.032-0.06 and 0.006-0.03, respectively. Substituting the range of values of the parameters τ and ϕ used in their experiments and solving Eq. (2.2) shows that there is a measureable, but relatively minor effect, of these parameters on the resultant horizontal distances and velocities for the case of $\theta_o = 0^o$. The numerical results for a range of values of Ω between 0.03 and 0.45 are shown in Fig. 2.6(a), with $\tau = 0.045$ and $\phi = 0.018$. In this figure, it can be seen that the horizontal speeds are similar in the initial portion of the flight, while heavier plates (all else being equal) travel relatively slower for large $\bar{x}$. The solutions are also compared with Eq. (2.10). Clearly, the current results are offset from the fit to the experimental data given by Eq. (2.10), although they are still within the experimental range. There is, however, an explanation for this offset.

Because of the nature of the experiments, the initial angle of attack cannot always be perfectly set to 0^o in a large boundary layer wind tunnel, which has some nominal level of free stream turbulence and mean nonuniformity in the flow. While the initial angle of attack is nominally 0^o, there could be small variations in the initial conditions for each particular case. Examining Fig. 21(a) of Lin et al. (2006), it is clear that the upstream horizontal velocity for some of the square plates exceeds the upstream horizontal wind velocity, U_w. In general, the only way this can happen is when the plate is rotating anti-clockwise (in the current coordinate system), rather than clockwise. Since rotational speeds were not reported in their work, we have to speculate on this. In any

case, to account for slight fluctuations in the initial angle of attack, we re-computed the results using $\theta_0 = -2^\circ$ (178°), 0°, $+2^\circ$. Fig. 2.6(b) shows the results. As can be seen, results for $\theta_0 = 2^\circ$ are not much different from the case of $\theta_0 = 0^\circ$, but the solutions for the cases with $\theta_0 = -2^\circ$ (178°) lie above the line defined by Eq. (2.10), perhaps explaining much of the "scatter" observed in the Lin et al. (2006) data.

2.3 Discussion of Results

2.3.1 Asymptotic Limits for Small $\bar{x}$

The non-dimensionalization for $\bar{x}$ and $\bar{y}$ uses the buoyancy parameter, φ. At the initiation of flight, $U_{rel} \approx U_w$ and $u \approx 0$, so that φ governs the initial response. Significantly, the initial angle of attack does not matter much. Fig. 2.6(c) enlarges the area of Fig. 2.6(b) for small $\bar{x}$, and indicates that the results for the different initial angles of attack and different values of Ω collapse well for $\bar{x} < 0.25$. By this point, $\bar{u} = 0.5$, i.e., at least half of the asymptotic value. To put this into context, consider typical dimensions of two common forms of windborne debris, namely plywood sheets and asphalt shingles. For $\bar{x} = 0.25$, $x \sim 3$m for plywood (with $h = 12$ mm and $l = 1.2$ m) and $x \sim 2$ m for asphalt shingles (with $h = 3.5$ mm and $l = 0.35$ m. Thus, debris originating from a building will attain a high speed while it is still in the immediate vicinity of the building from which it originated.

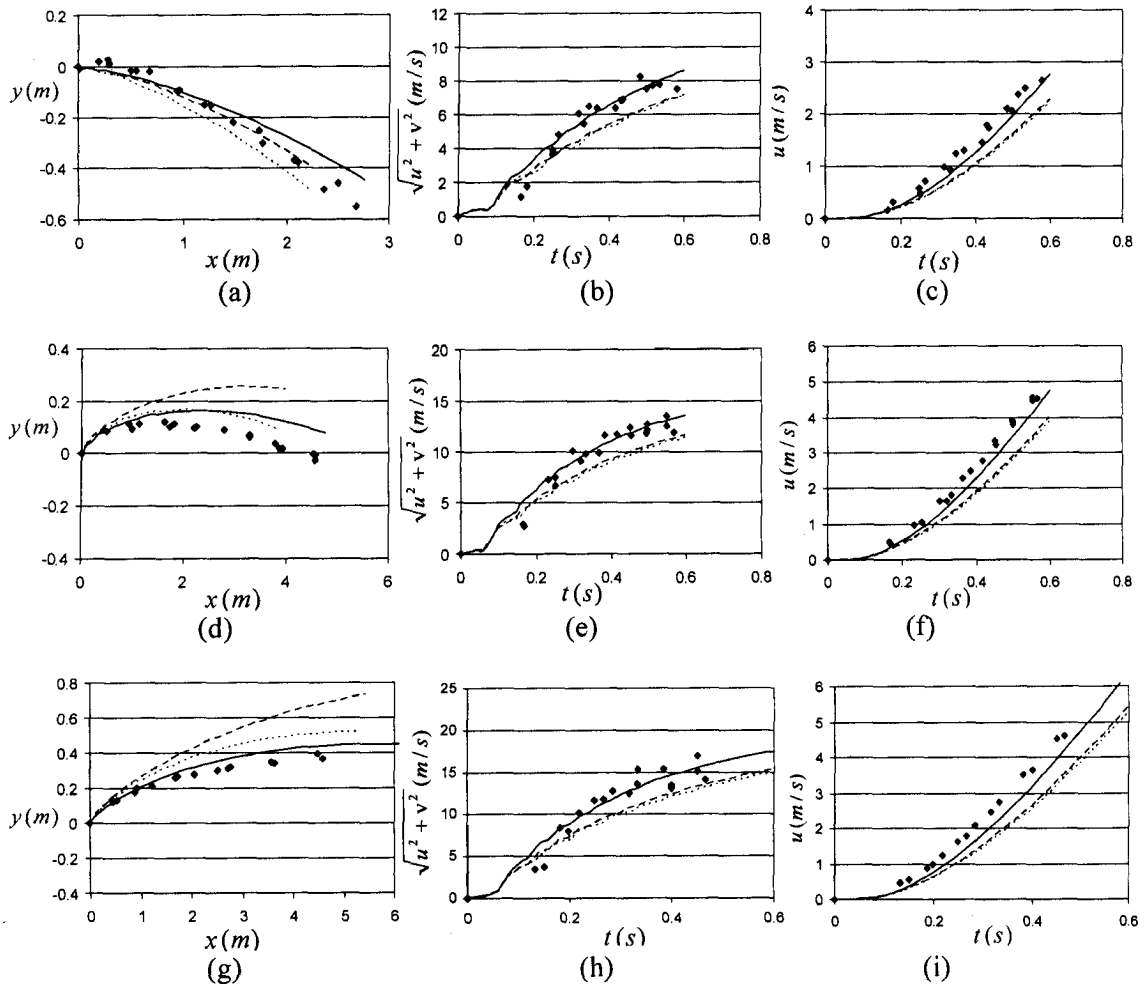

Fig. 2.5: Comparison of the current computed trajectories with the TTU data for a square basswood plate, with an initial angle of attack, θ_0=0°, and uniform wind speed of (a-c) U_w=15.6 m/s, (d-f) U_w=21.4 m/s, and (g-i) U_w=25.6 m/s. (a, d, g) vertical distance vs. horizontal distance, (b, e, h) plate's velocity vs. time, and (c, f, i) plate's horizontal velocity vs. time. TTU data, ◆ ; numerical solution including C_{LR}, ...; numerical solution including C_{LR} and C_{MR}, ------; numerical solution including C_{LR} , C_{MR} ,and C_{DR}, ———

(a)

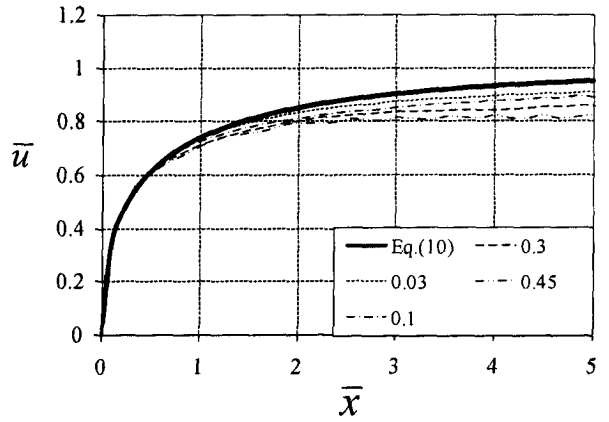

(b)

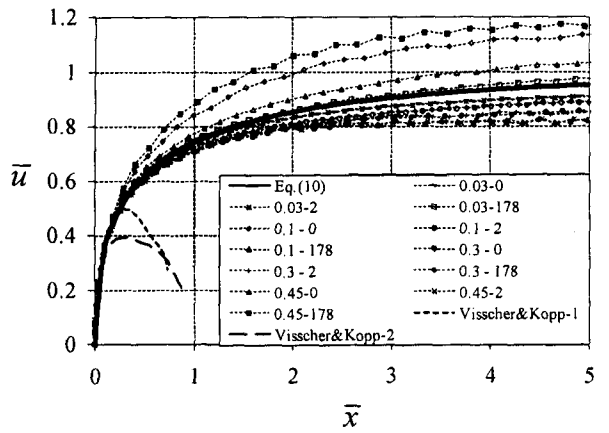

(c)

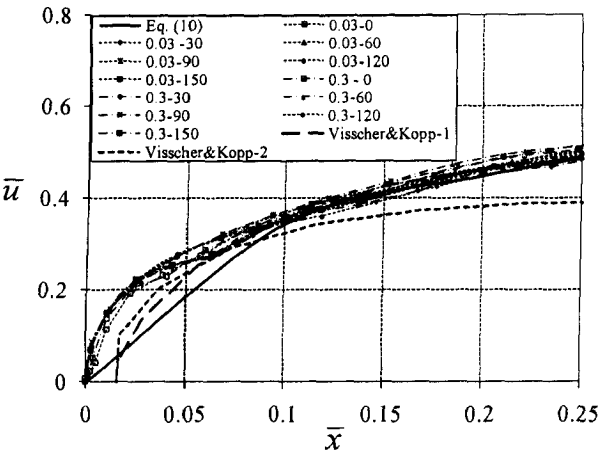

Fig. 2.6: Comparison between computed horizontal speeds using Eq. (2.10), Visscher & Kopp's (2007) translational and autorotational panel represented by 1 & 2, respectively, and the solutions of Eqs. (2.2, a-b) for sheet debris with: ϕ=0.018, τ=0.45, 0.03≤Ω≤0.45: (a) θ_0=0°, (b) θ_0=0°, 2°, 178°, and (c) Ω=0.03,0.3 and θ_0=0°, 30°, 60°, 90°, 120°, 150°.

Visscher and Kopp (2007) presented results for the translating and autorotating sheathing panels originating from the leeward side of the gable roof of a two-story building in a turbulent atmospheric boundary layer with an initial holding force. Given this initial dependence on φ one wonders whether these trajectories also follow this basic behavior. Thus, their two reported trajectories were added to Fig. 2.6b and Fig. 2.6c. Although the initial condition and the wind flow are significantly different when compared to the uniform, smooth flow assumed in the calculations, and used in Lin et al.'s (2006) data, the early part of the flight shows surprising agreement with the calculations. However, as can be seen in Fig. 2.6(b), the speeds drop off dramatically later in the flight for these relatively heavy panels. The effects of such 'real' flow conditions will be examined further in this work.

2.3.2 Asymptotic Limits for Large $\bar{x}$

The asymptotic horizontal speed for the plates in Fig. 2.6(b) with $\tau = 0.045$, $\phi =$ 0.018, and $\Omega = 0.03$, 0.1, 0.3, and 0.45 are 0.95, 0.92, 0.86, and 0.82, respectively, for clockwise rotation and 1.05, 1.08, 1.14, and 1.18 for counter-clockwise rotation. It is important to observe that by $\bar{x} \sim 3$, the plates have basically reached the asymptotic limit, or about one order of magnitude further downstream from the point where the initial similarity of the flight (bound by $\bar{x} < \sim 0.25$) starts to be altered by plate details. Considering the example of plywood sheet and asphalt shingles from above, this implies that the asymptotic limit is practically reached within 20 – 30m of the point of origin. This suggests that wind borne debris can reach the asymptotic solution in real situations

and understanding the asymptotic behavior of the plate is imperative for practical purposes, a point made by Baker (2007).

In order to consider the asymptotic limit, one needs to recall that the four non-dimensional parameters (Ω, φ, θ_o, τ) govern the behavior. The effect of φ is particularly subtle as it does not appear either explicitly or implicitly in Eq. (2.9) for square plates. In fact, the role of φ is to determine, partially, the sign (i.e., the direction of rotation) in Eqs. (2.8) or (2.9), but this can only be done by solving the trajectory in time. In fact, this is a subtle point because it is all four parameters that determine the ultimate direction of rotation, and the resulting signs in Eq. (2.9). So, asymptotic speeds are plotted in Fig. 2.7, while the direction of rotation is plotted in Fig. 2.8 as a function of φ for several values of θ_o and τ.

Fig. 2.7 shows the effect of variation of Ω on the asymptotic solutions of thin square plate debris from a full solution of Eqs. (2.2, a-c) with different initial angles of attack, 30°, 90°, 150°, and constant values of $\phi = 0.03$ and $\tau = 0.05$. It also compares the asymptotic numerical solutions of Eq. (2.2) with the asymptotic solutions, Eq. (2.9). There is a good agreement between numerical solutions and the asymptotic solutions, Eq. (2.9). It can be seen that as Ω increases the plates with $\theta_0 = 30°$ and $\theta_0 = 150°$ do not change their rotational direction while the plate with θ_0=90° does change its direction of rotation. One observation, not readily apparent from this plot, is that, as the effect of rotational drag is added to the model, the difference between the asymptotic horizontal speed for the two cases of clockwise and anti-clockwise rotation decreases.

Fig. 2.8 shows plots of the direction of rotation for a thin square plate with τ=0.025 for two different initial angles of attack, 60° and 90°, in the Ω-ϕ plane for flow from left-

to-right. The plates considered in this plot are bound by $\varphi = 0.01$ and 0.1. As can be seen, the lighter plates with $\theta_0 = 60^\circ$ are more likely to rotate in the clockwise direction and the heavier ones anti-clockwise, but there is no such role for the $\theta_0 = 90^\circ$ case where the behavior is more complex. The dimensionless times to reach the asymptotic solution for the plates with Ω=0.01 and Ω=1 are about $\bar{t}$ =20-40 and $\bar{t}$ =2-4, respectively.

Baker (2007) showed the asymptotic sign of the rotation in the Ω-ϕ plane and indicated three regions, clockwise, anti-clockwise, and negligible rotation, without mentioning the values of φ that were considered. However, for wind-driven plates in uniform flow, the asymptotic solution is always auto-rotational, with either direction possible, as indicated by Eq. (2.8), for Reynolds numbers of relevance to windborne debris.

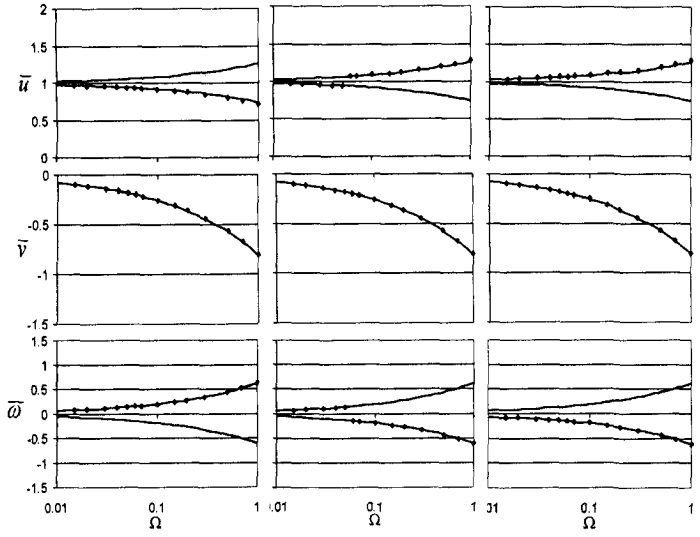

Fig. 2.7: Effect of variation of Ω on the asymptotic values of $\bar{u}$, $\bar{v}$, and $\bar{\omega}$ for square plates with ϕ=0.03 and τ=0.05 for an initial angle of attack, θ_0, of (a) 30°, (b) 90°, and (c) 150°. The symbol, ♦, is from computed solution, while, _____, is obtained via Eqs. 15(a)-(c).

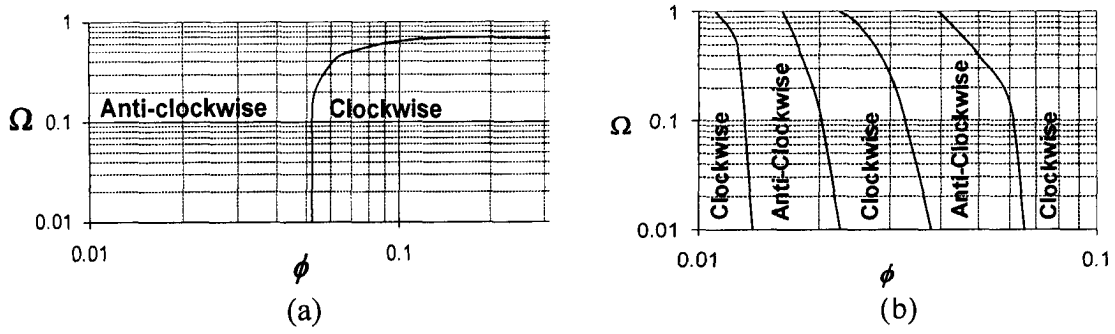

Fig. 2.8: Regions of clockwise and anti-clockwise asymptotic rotation for a square plate debris with τ=0.025, for an initial of angle of attack, θ_0, of (a) 60° and (b) 90°.

2.3.3 Asymptotic Limit at U_w = 0 (Falling Plates)

It has been shown above that the asymptotic limit of Eq. (2.2) for wind-driven plates in uniform flow at large times has a closed form solution which is always autorotational. However, in the limit of $U_w = 0$, this is clearly not the case, as observed by Andersen et al. (2005) and many others. Thus, presumably for small U_w, there would be similar behavior, but there are no data to establish the bounds on when only autorotational (or tumbling) flight trajectories are observed asymptotically. In any case, this is perhaps not pertinent for wind-driven plates for debris applications; however, it would be of some use to know whether the current quasi-steady model functions well for falling plates.

Based on the earlier literature, our quasi-steady model for 2D plates is as follows. Using the data reported by Hoerner (1965), the static normal force coefficient, C_N, on the plate is assumed to be

$$C_N = \begin{cases} 0.7\dfrac{\alpha}{7^\circ} & \alpha \le 7^\circ \\ 0.7 + 0.15\dfrac{\alpha - 7^\circ}{13^\circ} & 7^\circ < \alpha \le 20^\circ \\ 0.253 + 1.747\sin(\alpha) & 20^\circ < \alpha < 160^\circ \\ 0.7 + 0.15\dfrac{173^\circ - \alpha}{13^\circ} & 160^\circ \le \alpha < 173^\circ \\ 0.7\dfrac{180^\circ - \alpha}{7^\circ} & 173^\circ \le \alpha \le 180^\circ \end{cases} \tag{2.11}$$

The normal force is resolved to yield the lift and drag components. An additional drag coefficient of 0.15 is assumed as the effect of the skin friction component for the thickness ratios less than 0.2 (Andersen et al. 2005). Thus,

$$C_{DS} = 0.15 + C_N \sin(\alpha) \tag{2.12a}$$

$$C_{LS} = C_N \cos(\alpha) \tag{2.12b}$$

Based on Richards et al.'s (2008) results for the plates with AR=4, the center of pressure, c, is assumed to be at

$$\frac{c}{l} = 0.25 - \frac{\alpha}{2\pi} \tag{2.13}$$

so that the static moment coefficient can be calculated as

$$C_{MS} = \frac{c}{l} . C_N \tag{2.14}$$

Andersen et al. (2005) defined the rotational part of the lift coefficient as a linear function of the spin parameter, S. Applying this so that it reaches Skews' value at the point of stable autorotation yields

$$C_{LR} = 1.3\frac{S}{S_o} \tag{2.15}$$

As well, if we assume that the rotational drag coefficient also has a linear relation with the spin parameter, reaching Skews' value at the point of stable autorotation, but

flattening off beyond this, as observed by Tachikawa (1983), the rotational drag force coefficient is

$$C_{DR} = \begin{cases} 0.35 & \left|\frac{S}{S_o}\right| \geq 1 \\ 0.35\left|\frac{S}{S_o}\right| & 0 \leq \left|\frac{S}{S_o}\right| < 1 \end{cases} \tag{2.16}$$

Using Lugt's (1980) autorotational work, the rotational moment coefficient is assumed to be

$$C_{MR} = \begin{cases} k'_{MR}(1-\frac{S}{S_o}) & \frac{S}{S_o} > 1 \\ k_{MR}(1-\left|\frac{S}{S_o}\right|)\frac{S}{S_o} & -1 \leq \frac{S}{S_o} \leq 1 \\ -k'_{MR}(1+\frac{S}{S_o}) & \frac{S}{S_o} < -1 \end{cases} \tag{2.17}$$

where k_{MR} and k'_{MR} are the rotational and anti-rotational pitching moment constants. Based on Lugt (1980), it can be assumed $k_{MR} = k'_{MR} = 0.08$ for a 2D elliptical cross section. Andersen et al. (2005) observed that the total torque on a 2D thin ellipse is twice the total torque on a 2D thin rectangular plate. Since there has been no work on a 2D thin rectangular plate, to the knowledge of the writer, it is assumed that $k_{MR} = k'_{MR} = 0.16$.

Using these static and autorotational force coefficients, the same tumbling and fluttering plates given in Fig. 2.2 are solved. Fig. 2.9 shows the computed results for the trajectories. These computed trajectories are in good qualitative agreement with Andersen at al.'s experiments and the model is even able to capture a (slightly) positive vertical velocity at the turning points (c.f., Andersen et al. 2005, Fig. 2). However, there are some significant errors in the model. In particular, the absolute values of computed horizontal and vertical velocity are lower than what were reported by Andersen et al. (2005) while

the rotational velocity is higher than what they reported and has substantially different frequency content.

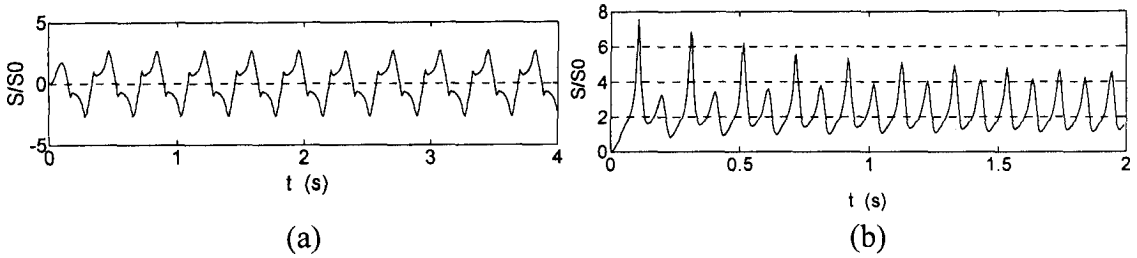

(a) (b)

Fig. 2.9: Ratio of spin parameter, S, to the spin parameter at the point of stable autorotation, S_o, for the present computations of two-dimensional (a) fluttering and (b) tumbling plates, for the same plate details as in Fig. 2.2.

One of our observations is that the results are sensitive to the chosen coefficients, particularly since the rotational speeds are so high for these calculations in still water. For example, if k'_{MR} was assumed to be 0.32 instead of 0.16, the range of horizontal, vertical, and rotational velocity of the tumbling plate would be much closer to Andersen et al. (2005). There is no basis to make such a change, however, based on the literature. It is interesting to point out that the weakest comparisons between the 3D empirical model and Tachikawa's experimental data were for cases with higher rotational speeds. This points to significant limitations in the quasi-steady model when there are high rotational speeds present and the model should be used with caution under these circumstances.

2.4 Conclusions

A quasi-steady model to predict the trajectories and speeds of wind-driven 3D plates was suggested. The model incorporates the effects of rotational lift, drag, and pitching moment using single degree of freedom autorotation data for thin plates. There

are four independent non-dimensional parameters which are required to determine the trajectory of windborne plate debris. It was observed that plate rotational speeds are not well predicted by the quasi-steady model when these speeds are large, such as occurs during falling in a still fluid. However, the trajectories when the plates are dominated by a uniform free stream show excellent agreement when compared with existing experimental data. An important aspect is that the rotational drag plays a significant role and should be included in the model. In fact, the developed model captured the physics sufficiently to explain some of the scatter observed in the experimental data of Lin et al. (2006). Additionally, it was shown that the initial horizontal plate speeds are largely dependent on the buoyancy parameter, φ, so that non-dimensionalization of spatial coordinates with this parameter collapses the data well in the early stages of flight. The asymptotic limit at large times showed that wind-driven plates will always rotate, the direction of which is determined in a complex way by the four governing parameters.

References

Andersen, A., Pesavento, U., and Wang, Z. J. (2005). "Unsteady Aerodynamics of fluttering and tumbling plates." *J. Fluid Mech.* 541, 65-90.

Baker, C.J. (2007). "The debris flight equations." *J. Wind Eng. Ind. Aerodyn.* 95, 329-353.

Belmonte, A., Eisenberg, H., and Moses, E. (1998). "From Flutter to tumble: inertial drag and Froude similarity in falling paper." *Phys. Rev. Lett.* 81(2), 345-348.

Flachsbart, O. (1932). "Messungen an ebenen und gewolbten Platten." *Ergebnisse der AVA. IV.*

Hoerner, S. F. (1965). "Fluid-dynamic drag." Hoerner Fluid dynamics.

Holmes, J.D., Letchford, C.W., and Lin, N. (2006). "Investigations of plate-type windborne debris- Part II : Computed trajectories." *J. Wind Eng. Ind. Aerodyn.* 94, 21-39.

Iversen, J. D. (1979). "Autorotating flat plate wings: the effect of the moment of inertia, geometry and Reynolds number." *J. Fluid Mech.* 92, 327-348.

Kordi, B., and Kopp, G.A. (2009). "Discussion "The debris flight equations" by C.J. Baker." *J. Wind Eng. Ind. Aerodyn.*, 97, 151-154.

Lin, N., Letchford, C., and Holmes, J.D. (2006). "Investigation of plate-type windborne debris. Part I. Experiments in wind tunnel and full scale." *J. Wind Eng. Ind. Aerodyn.* 94, 51-76.

Lugt, H. J. (1980). "Autorotation of an elliptic cylinder about an axis perpendicular to the flow." *J. Fluid Mech.* 99, 817-840.

Lugt, H. J. (1983). "Autorotation." *Ann. Rev. Fluid Mech.* 15, 123-147.

Mahadevan, L., Ryu, W.S., and Samuel, A.D.T. (1999). "Tumbling cards." *Phys. Fluids Lett.* 11(1), 1-3.

Maxwell, J.C. (1854). "On a particular case of the descent of a heavy body in a resisting medium." *Cambridge and Dublin math. J.* 9, 145-148.

Pesavento, U., and Wang, Z. J. (2004). "Falling paper: Navier-Stokes solutions, model of fluid forces, and center of mass elevation." *Phys. Rev. Lett.* 93, 144501.

Pesavento, U. (2006). "Unsteady aerodynamics of falling plates." Ph.D. Thesis, Physics Department, Cornell University, Ithaca, NY.

Richards, P.J., Williams, N., Laing, B., McCarty, M., and Pond M. (2008). "Numerical calculation of the three-dimensional motion of wind-borne debris." *J. Wind Eng. Ind. Aerodyn.* 96, 2188-2202.

Skews, B.W. (1990). "Autorotation of rectangular plates." *J. Fluid Mech.* 217, 33-40.

Smith, E.H. (1971). "Autorotating wings: an experimental investigation." *J. Fluid Mech.* 50, 513-534.

Tachikawa, M. (1983). "Trajectories of flat plates in uniform flow with application to wind-generated missiles." *J. Wind Eng. Ind. Aerodyn.* 14, 443–453.

Visscher, B.T., and Kopp, G.A. (2007). "Trajectories of roof sheathing panels under high winds." *J. Wind Eng. Ind. Aerodyn.*, 95, 697-713.

3 EXPERIMENTAL SETUP

The "failure model" approach is used to examine the trajectory of the roof tiles, asphalt shingles, and sheathing panels originating from a gable roof of a house in a scaled boundary layer flow. Details of the experiments are given below. (It should be mentioned again that the experimental setup described here for the sheathing panel tests is based on experiments conducted by Traczuk (2007)).

3.1 Basic Considerations

The failure model approach, recently described by Surry et al. (2005), and utilized by Farquhar et al. (2005) and Visscher and Kopp (2007), is used in the present study. In this approach, the failure mechanism cannot be generally modeled without prior knowledge of it. In the present work, failure is assumed to occur via wind pressure overcoming the holding force, an assumption which is not strictly correct for shingles and, to a lesser extent, tiles. However, the goal is that the flow field at failure be reasonably realistic so that the movement of the debris element within the gust structure causing failure is correct; consistent with the objective of the work to determine debris trajectories and speeds in as realistic a flow simulation as possible. The goal of the work is not to determine failure mechanisms, and this fact should be kept in mind.

One of the primary challenges with the failure model approach is that mass and force scaling require relatively light elements with small forces. In order to actually perform such experiments, larger models than normal are required in order that the model

be manufactureable. For example, Visscher and Kopp (2007) used a model length scale of 1:20. Of course, this contrasts with the requirements of the wind tunnel simulation where smaller-scale flow simulations are used, the norms for boundary layer wind tunnels typically being 1:300 to 1:500 for high-rise buildings, where the entire depth of the atmospheric boundary layer is modelled, and 1:100 to 1:200 for low-rise buildings, where only the lower portion of the boundary layer is modelled. These challenges were discussed in an earlier work, pertaining to pressure models (Kopp et al., 2005), but the constraints are more severe for failure models generally. Given that there is a significant need for the type of data presented herein, data which is not possible to obtain in full-scale at this time, large model scales are used in the present work. The main limitation of this is that the integral scales of the flow are too small compared to those observed in full scale. The effects of this will be examined in the chapter six of the thesis. In any case, few of our future conclusions depend on this mismatch. Nevertheless, there may be implications of these results when applying them in full scale, which the reader should keep in mind.

3.2 House Model

An acrylic, two-storey, gable roof house at a scale of 1:20 was used for the experiments. This is the same model as used by Visscher and Kopp (2007). The plan dimensions of the model are 45.7 cm by 51.9 cm, with an eave height of 30.0 cm. The gable roof has a pitch of 4:12 and rises 9 cm from the top of the wall. A 2.54 cm roof overhang exists around the perimeter of the building. At a scale of 1:20, the equivalent full-scale dimensions are 9.14 m (30 ft) by 10.38 m (34 ft), with the eave height of 6 m (19.8 ft). Fig. 3.1 shows a photograph of the model house in the wind tunnel. This is a

model of the house currently being tested at the 'Three Little Pigs' project (Kopp et al., 2008).

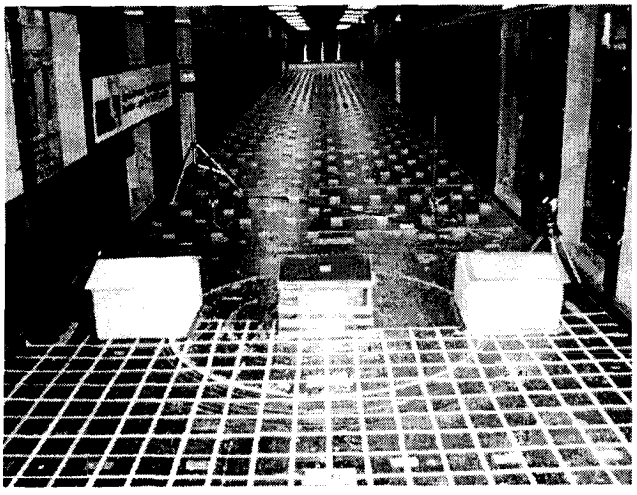

Fig. 3.1: Photograph of the 1:20 scale, gable roof model house in the wind tunnel, looking upstream. The house in the center is the main house.

3.3 Plate Debris Models

3.3.1 Roof Tiles

The tile dimensions were chosen to match typical dimensions found in practice. Full scale tile dimensions of 41.9 cm by 34.3 cm with the thickness of 3.17cm and mass of 4.86 kg were considered for the experiment. The mass scale is

$$\lambda_m = \lambda_\rho . \lambda_L^3 = \frac{\text{Mass in model scale}}{\text{Mass in full scale}} \tag{3.1}$$

where λ_ρ is the density scale and λ_L is the length scale. The density scale is 1:1 since air is the common fluid between full scale and the wind tunnel. With the length scale of 1:20, the mass scale is, therefore, 1:8000. The model tiles had target plan dimensions of 21 mm by 17.1 mm with a thickness of 1.6 mm and mass of 0.61 gr. To meet the criteria for the thickness and weight of the rigid model, as well as to have a metal surface in order to use

magnets for the hold down force, the model tiles were made as a sandwich of a central layer of Styrofoam, with a thickness of 1.39 mm, and a layer of steel "shim stock" on each side, one with a thickness of 0.07 mm and the other with a thickness of 0.14 mm. The tiles were presumed to be rigid. Fig. 3.2a shows a photograph of the model roof tile. Individual tiles were placed on the roof with the short edge parallel to the ridge of the roof. Table 3.1 shows the characteristics of the tiles used during the testing. Because the tiles would sometimes break (from repeated impacts with the ground), several model tiles were used. The model tiles were painted white in order to be visible to the cameras, described below, although half of one side was left unpainted in order to better control the hold down force.

Table 3.1: Characteristics of the model tiles used for each configuration.

Position_Pattern_Wind-Angle	m (gr)	*B* (mm)	*l* (mm)	*h* (mm)	Hold Down Force (N)	Equivalent hold-down moment (N.m)
A, C, D, F, E_I_0, B_II_45 (tests 1-15)	0.63	21	17	1.6 - 1.9	0	0
E_II_0, B_II_45 (tests16-30), B_III_45 (tests 1-21)					7.35 E-3	77.47 E-6
B_I_45, B_III_45 (tests 22-30)					19.61 E-3	205.93E-6

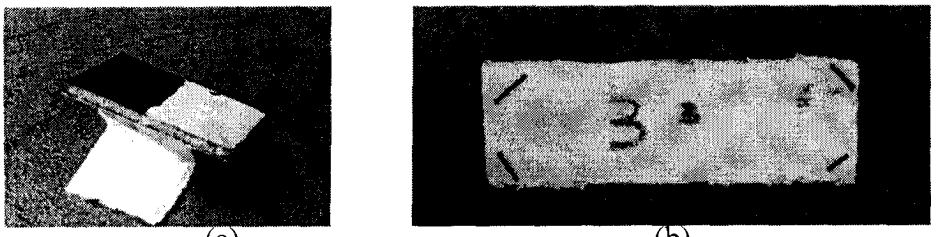

(a) (b)

Fig. 3.2: Photograph of the 1:20 scale model of (a) roof tile and (b) roof shingle.

3.3.2 Roof Asphalt Shingles

The shingle dimensions were chosen to match typical dimensions found in practice so that full scale dimensions of 100 cm by 34 cm with a thickness of 3.5 mm and mass of 1.58 kg were considered for the experiment. With the length scale of 1:20 and mass scale of 1:8000, the model shingles were designed to have plan dimensions of 5 cm by 1.7 cm with the thickness of 0.175 mm and mass of 0.23 gr. Individual shingles were placed with the long edge parallel to the ridge of the roof, as they are in practice.

A roof shingle is a flexible object, so scaling of the elastic (bending) stiffness was required for the model. The equivalent elastic stiffness was obtained indirectly by considering the shingles as simple cantilever beams, rigidly fixing one end, and then measuring the end deflection, δ_{max}. Because of the required geometric similarity, the ratio δ_{max}/B should be the same in both model scale and full scale for the same aspect ratio. Thus, the full scale deflections were measured and used as the basis for choosing the model material.

It was observed that full scale asphalt shingles have different flexibility depending on which side is up. For a aspect ratio of 2.95, the flexibility of the shingle with the asphalt side up was such that $\delta_{max}/B = 0.60$ and, with the asphalt side down, the ratio was 0.34. The mean value of 0.47 was used for the design of the model.

A light fabric was chosen for the model shingles. In order to gain the desired flexibility, a thin layer of glue was used on one side of it. The glue also sealed the fabric so there was no air leakage through the material. Fig. 3.2b shows a photograph of the model shingle. Table 3.2 shows the characteristics of the shingles used during the testing. However, it should be noted that the thickness, h, of the fabric is greater than the target thickness. Based on Iversen's (1979) autorotation experiments, it is expected that for thickness ratios, h/l, less than 0.05, this ratio does not have a significant effect on the aerodynamics.

Table 3.2: Characteristics of the model shingles used for each configuration.

Position (Pattern)	m (gr)	B (mm)	l (mm)	h (mm)	δ_{max}/B	Hold Down Force (N)
Pos. :A, B, C, D, E Pos. F (_I_0, _II_0)	0.23	50	17	0.65	0.5 - 0.55	5.69 E-3
Pos. F (_I_45, _II_45)					0.34	11.37 E-3

3.3.3 Roof Sheathing Panels

The roof sheathing panel dimensions were chosen to match typical dimensions found in practice so that full scale dimensions of 1.2 m by 2.4 m with a thickness of 12.7 mm and mass of 66.9 Kg were considered for the experiment. Using the length and mass scales described above the model roof sheathing panels were designed to have a length, l, of 6cm, and the width, B, of 12 cm, a thickness of 0.635 mm, and a mass of 8.360 gr. The panel was placed with the long edge parallel to the ridge of the roof.

The model sheathing panels were made of Rohacell 71 modelling foam. A thin layer of paint was used on both sides of the panel to help prevent air leakage. To simulate

the hold down force of the nails, two circular steel cut-outs were glued on the back of the model panel that would come in contact with the electromagnets located inside the roof cavity. In addition, two longitudinal strips of brass were used on the back of the model to match the mass-moment-of-inertia about all three axes. Please refer to Fig. 3 of Visscher and Kopp (2007) for a photograph of a typical panel.

3.4 Hold-Down Forces

The scaling relationship for model to full scale forces is

$$\lambda_F = \lambda_\rho . \lambda_V^2 . \lambda_L^2 = \frac{\text{Force in model scale}}{\text{Force in full scale}} \tag{3.2}$$

Froude scaling is required to obtain the correct effects of gravity on the flight trajectories, so that

$$\lambda_V = \sqrt{\lambda_L} \tag{3.3}$$

and

$$\lambda_F = \lambda_L^3 \tag{3.4}$$

Thus, the force scale is 1:8000 in the current experiments.

3.4.1 Roof Tiles and Shingles

The full scale failure pressure for the tiles and shingles was initially assumed to be 1.2 kPa (25 psf). Considering the sizes of the tiles and shingles, this results in initial hold-down forces of 172 N and 408 N, respectively. In the model scale, these holding forces are 0.0215 N and 0.051 N, respectively.

The calibration setup involved an apparatus consisting of a system of weights and pulleys. The magnet was secured to a table and the model tile or shingle was attached to the magnet with the desired contact length. A fishing line was connected to the models through the center at one edge. The fishing line was connected to pulleys, and attached to a cradle at the other end, where the loads where applied. Table 3.1 shows the actual hold down force applied for each tile configuration. Note that the weight of the tile should be added to these hold down forces since the resistance to flight is through the combination of these. As an additional comment, it was later observed that many of the tile failures appeared to be by overturning, rather than uplift. Thus, Table 3.1 also gives the equivalent overturning moment about the leeward edge (i.e., the rotation point) for the magnet force (i.e., the moment neglecting the mass of the tile) as obtained through calibration.

For both of the tiles and shingles, the hold down force was provided by metal contacts glued to the models, while a magnetic strip (like a 'fridge' magnet) was placed on the model house roof at the desired location. For the tiles, the steel sides were used to provide the magnetic force. This force could be adjusted by altering the length of the model in contact with the magnet. In order that the magnetic strips be flush with the roof surface, small slots were machined in the surface of the model roof with a nominal size of 5 cm by 2.5 cm and a depth of 0.5 mm. Then, the magnetic strips were attached to the roof at each of these positions in turn. Six different roof locations were used, shown in Fig. 3.3a.

In order to provide the holding force for the model shingle without altering the flexibility of the model, thin steel "shim stock", like that used for the tile models, was cut

into small pieces and glued onto one side of the fabric. The desired hold down force could be altered by changing the thickness of the magnet or the quantity of metal glued to the fabric.

The hold down force was a difficult parameter to implement, the reasons for which will be more clearly understood after the results are presented. As an example, the very first shingle flight, at a hold down force of 0.051 N (equivalent to 25 psf in full-scale) resulted in a flight that terminated with the shingle stuck to the downstream fan screen well above the centerline of the wind tunnel (in the uniform flow in core of the wind tunnel). Since the goal of the experiments, as described above, was to get good data on flight distances for particular configurations, the hold down force had to be modified. Thus, the finite field of view of the camera and the desire to have failure occur at a realistic wind speed for hurricanes led to adjustments of the hold down force. The most constraining of these was the field of view of the camera. Thus, the basic method for choosing the holding force was the requirement of "measurable flight trajectories" with a realistic equivalent full scale wind speed. In general (though not always), the larger the hold down force, the further the flight. The results could be quite sensitive at times, so that choices were not always straightforward. Table 3.2 lists the holding force used for each configuration.

3.4.2 Roof Sheathing Panels

A total nail pull out resistance of 8.54kN, equivalent to 1.07 N in model scale, was considered for the entire panel. This was comparable to a nailing pattern of 6d nails at 6/12 spacing, obtained from the HAZUS Wind Loss Estimation (Applied Research

Associates Inc., 2002). Two electromagnets, located underneath of the model panels inside the roof cavity, were calibrated to provide the appropriate scaled hold-down force. The failure is assumed to occur via wind pressure overcoming the holding force.

3.5 Boundary Layer Simulation

All experiments were conducted in Boundary Layer Wind Tunnel II at the University of Western Ontario. The boundary layer simulation was designed to mimic an open country terrain, having an aerodynamic roughness length, z_o, of 0.015 m, as defined by Engineering Sciences Data Unit (ESDU, 1974, 1982, 1983). The boundary layer was generated using adjustable roughness elements on the wind tunnel floor for the 39 m (128 ft) upstream fetch, 3 large, 1.5 m (59 in) spires, and one 38.5 cm (15 in) high barrier. These obstructions were necessary to generate the large scale turbulent gusts. The resulting flow simulation was identical to that used previously by Visscher and Kopp (2007) and the reader is referred to that work for further details. However, it is emphasized that at a scale of 1:20, the integral scales of the flow are too low compared to actual flow and this may affect the results. In fact, it would be practically impossible to do these experiments with smaller models, which is the reason why, in the earlier work we relaxed the scales. This is not expected to substantially alter the aerodynamic loads on the building since the streamwise integral scale, L_x, of 0.91 m is twice the streamwise length of the building (Surry, 1982). However, it could have an effect on the interpretation of the trajectory results in equivalent full-scale dimensions, so care needs to be used in such interpretations (although we do present the dimensional results in full-scale dimensions, following the practice in the wind engineering discipline).

3.6 Surrounding Neighbourhood

3.6.1 Roof Tiles and Shingles

For the proximity model of the surroundings, two neighbourhoods, with typical housing densities of 6.5 and 3.0 houses/acre were examined. Fig. 3.3b shows drawings of the house layouts where "d" equals 1.0 and 1.8 times the length of the house, L_{House}= 51.9cm in model scale, for 6.5 and 3 houses houses/acre, respectively. The distance between the houses in every row was considered to be twice the length of the house. Three different neighbourhood patterns are defined as: "I" for 1 row of housing with 6.5 houses/acre, "II" for 2 rows of housing with 6.5 houses/acre, and "III" for 2 row of housing with 3 houses/acre. The three neighbourhood patterns with two wind angles of 0 and 45 degrees and six roof locations for the tiles and shingles were used in such a way that 12 configurations for tiles and 14 configurations for shingles were examined. For each configuration, about 30 individual tests were conducted to obtain a representative sample of the variation of the trajectories. The configurations examined are listed in Table 4.1.

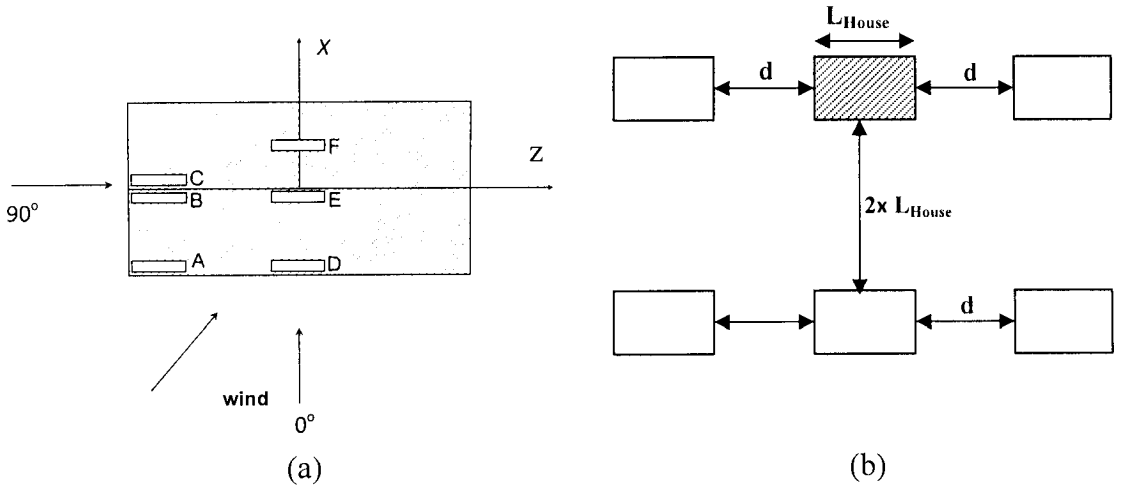

Fig. 3.3: Layout and definition sketch for (a) element locations on the roof, and (b) the subdivision setup for 2 rows of houses.

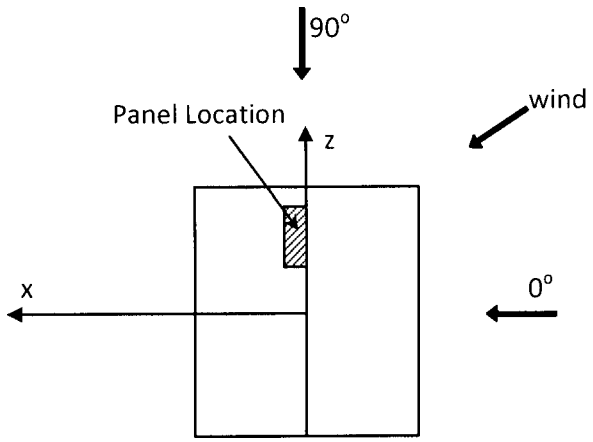

Fig. 3.4: Plan view showing the coordinate system, the definition of wind angle, and the plan dimensions of the model house.

3.6.2 Roof Sheathing Panels

Six wind directions, viz., 15°, 30°, 45°, 60°, 75°, and 90° were examined for one panel location without any neighbourhood houses. About 80 to 100 tests were conducted for each wind direction. Fig. 3.4 shows the location of the panel on the roof of the house with respect to the defined wind directions.

3.7 Test Procedure

Prior to testing a longitudinal and lateral grid on 6" centers was laid down on the wind tunnel floor with masking tape. This grid can be seen in Fig. 3.1. A plastic "bird net" was also laid down on the floor to ease catching the model tile or shingle on the floor and to minimize its impact with the floor. For each configuration, the model and neighbouring houses were set in the tunnel. Since the debris elements were relatively light, they tended to fly straight down the wind tunnel once they had cleared the roof of the house. Thus, one high speed video camera was set in the best position to capture the trajectory of the model tile or shingle. However, to capture the trajectory of the panels, two high speed cameras were used. One was mounted to the ceiling of the wind tunnel to capture the horizontal and lateral movement of the panel and the other camera was located beside the model house at almost the same height of the house to capture the horizontal and vertical movement of the panel.

Each test was conducted in the same manner as Visscher and Kopp (2007) and Farquhar et al. (2005). So, each test was started at a wind velocity that had a low probability to cause a failure, as found through initial trials. Test durations equivalent to 10 min. in full scale were considered to be sufficiently long, as this is consistent with

wind events which are typically statistically stationary for this duration, while not causing the tests to take an excessive amount of time. This interval is equivalent to 130 sec with the current scaling. So, during testing, the fan drive voltage would be increased by 0.1 volts, equivalent to 0.19 m/s increase in wind speed at the mean roof height in model scale, every 130 sec, unless failure had occurred during the interval. Average tests took 20-30 minutes to complete, so obtaining 30 samples typically took in the range of 10-15 hours of continuous testing.

The failure wind velocity, $\hat{U}_H$, was measured for each test based on the wind tunnel drive voltage. This value, which originates from a mean value in the wind tunnel, is interpreted as the equivalent full-scale, 3-sec wind gust speed at the mean roof height using

$$\hat{U}_H = U_{ref} \times \lambda_V \times \frac{U_H}{U_{ref}} \times \frac{\hat{U}_{3\,\mathrm{sec}}}{\hat{U}_{600\,\mathrm{sec}}} = U_{ref} \times \sqrt{20} \times 0.78 \times \frac{1.52}{1.07} \tag{3.5}$$

where U_{ref} and U_H are the mean velocities at the reference height and mean roof height; the ratio is obtained from the velocity profile measurements in the wind tunnel, while $\hat{U}_{3sec}$ and $\hat{U}_{600sec}$ are the ratio of 3- and 600-sec gust speeds to the hourly mean wind speed, as obtained by Durst (see ASCE 7-05). U_H is assumed to be a 10 min mean value. Gust speeds were not measured at failure, so it should be clear that these are estimates based on the mean wind tunnel speed and the terrain match being similar to that of Durst.

3.8 Calibration and Image Processing

3.8.1 Roof Tiles and Shingles

A MATLAB program was generated to separate the tiles or shingles (in flight) from the background image and extract the longitudinal and vertical pixel location of these in

each video image. Fig. 3.5a illustrates an example of a model shingle separated from the background image. Following this, the center of the debris element in each image was located. Using a conversion matrix, each pixel location was converted to dimensional values of the longitudinal, x, and vertical, y, location in the plane of the calibration image. Since only one high speed camera was available for these experiments, several calibration planes were required for each camera position in order to account for the lateral variation of the flight plane. Fortunately, because the debris elements were relatively light, they almost travel in the same lateral plane. Thus, a calibration board was placed at a particular lateral (z) location, so that the (x, z) variation in that plane could be obtained. Several calibration planes were obtained for each camera position. The calibration image closest to the impact location was chosen for the analysis of the trajectory so that the dimensional longitudinal and vertical positions as a function of time could be obtained. A typical calibration image is also shown in Fig. 3.5b.

Once the dimensional locations of the debris elements were obtained for each video image, the set of the longitudinal and vertical locations was mathematically fit to a polynomial function of time using least squares regression. The impact location of each test was compared with the image processing results and tests with errors lower than 10% was considered herein for the panel speed analysis. Following this, the longitudinal, u, and vertical, v, velocities were obtained by differentiation of the curve fit, and the magnitude of the translational velocity, $u_{mag} = \sqrt{u^2 + \mathrm{v}^2}$, was also calculated (lateral velocity is assumed to be zero in this case).

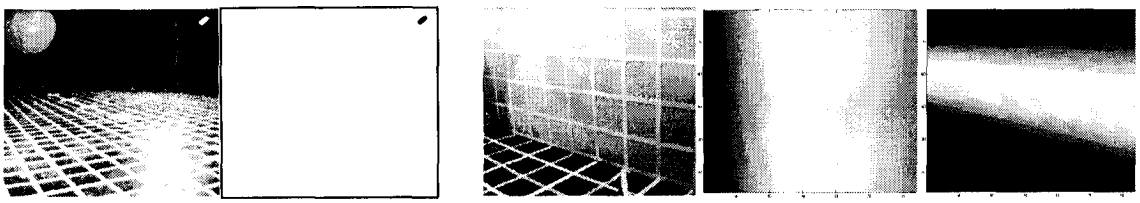

(a) (b)

Fig. 3.5: (a) Sample illustration of MATLAB image processing including (left) the original image, (right) the image with the background removed, (b) the calibration image.

3.8.2 Roof Sheathing Panels

The longitudinal, vertical, and lateral location of the sheathing panels were captured simultaneously by the two high-speed cameras. Like tiles and shingles, a Matlab program was generated to separate panels from the background image and extract the simultaneous longitudinal, vertical, and lateral pixel location of the panel in the images from the two cameras. Since the top camera was placed in the middle of the tunnel, high above the floor, and was pointed parallel to the wind flow, the longitudinal and lateral, x and z, pixel locations of the panels were captured from this camera. The grid lines on the floor were used to create a conversion matrix for the (x,z) pixel locations to dimensional values. The height of the panels, y, was captured by the side camera, but, because of the close proximity and angle of this camera, the estimated vertical location depends on the (x,z) location. Thus, multiple conversion matrices were created for the side camera by placing the calibration board at several locations in the lateral direction. The calibration matrix closest to the lateral position of the panel was chosen to convert the pixel height to dimensional values. Therefore, the dimensional longitudinal, vertical, and lateral positions as a function of time were obtained for each test.

Like tile and shingle analysis, a polynomial function of time was fitted to each set of horizontal, vertical, and lateral locations of the panel trajectory. From the polynomial

fit, the longitudinal (horizontal), u, vertical, v, and lateral, w, velocities of the sheathing panels were obtained by differentiation and the magnitude of the translational velocity, $u_{mag} = \sqrt{u^2 + v^2 + w^2}$, was also calculated.

References

Applied Research Associates, Inc.. HAZUS Wind Loss Estimation Methodology – Volume I. North Carolina, October 2002.

ASCE 7-05, Minimum Design Loads for Buildings and Other Structures, American Society of Civil Engineers, Reston, Virginia, 2005.

Engineering Sciences Data Unit (1974). Characteristics of atmospheric turbulence near the ground, Data Item 74031.

Engineering Sciences Data Unit (1982). Strong winds in the atmosphere boundary layer. Part 1: Mean-hourly wind speeds, Data Item 82026.

Engineering Sciences Data Unit (1983). Strong winds in the atmosphere boundary layer. Part 2: Discrete gust speeds, Data Item 83045.

Farquhar, S. W.A., Kopp, G.A., and Surry, D. (2005). Wind tunnel and uniform pressure tests of a standing seam metal roof model. *ASCE J. Struct. Eng.* 131, 650-659.

Iversen, J. D. (1979). "Autorotating flat plate wings: the effect of the moment of inertia, geometry and Reynolds number." *J. Fluid Mech.* 92, 327-348.

Kopp, G.A., Surry, D., and Mans, C. (2005). "Wind effects of parapets on low buildings: Part 1. Basic aerodynamics and local loads." *J. Wind Eng. Ind. Aerodyn.* 93, 817-841.

Kopp, G.A., Morrison, M.J., Iizumi, E., Henderson, D., and Hong, H.P., (2008), The 'Three Little Pigs' Project: Hurricane Risk Mitigation by Integrated Wind Tunnel and Full-Scale Laboratory Tests, submitted to *ASCE Natural Hazards Review*.

Surry, D., Kopp, G.A., Bartlett, F.M. (2005). "Wind load testing of low buildings to failure at model and full scale." *ASCE Natural Hazards Review*, 6, 121-128.

Surry, D. (1982). "Consequences of distortions in the flow including mismatching scales and intensities of turbulence", *Wind Tunnel modelling for civil engineering applications*, (ED: T.A. Reinhold), Cambridge University Press, Cambridge, 1982, 137-185.

Traczuk, G. (2007). "Trajectories of roof sheathing panels under high winds." Undergarduate thesis, The University of Western Ontario, Canada.

Visscher, B.T., and Kopp, G.A. (2007). "Trajectories of roof sheathing panels under high winds." *J. Wind Eng. Ind. Aerodyn.*, 95, 697-713.

4 FLIGHT RESULTS – ROOF TILES AND SHINGLES

In this chapter the flight of model roof tiles and shingles from a gable roof model house in a scaled turbulent boundary layer wind flow will be studied. In total, twenty six different configurations were examined by varying debris element, wind angle, element location on the roof, holding down force, and surroundings. The impact locations and the translational velocities of the debris will be fully studied.

4.1 Failure Wind Speeds

Table 4.1 presents the average,$(U_H)_{avg}$, of the full scale 10-min mean velocity at the mean roof height, as well as the average, $(\hat{U}_H)_{avg}$, and standard deviation, $(\hat{U}_H)_{\sigma}$, of the full scale gust (3 sec) failure wind velocity, $\hat{U}_H$, for each configuration. $\hat{U}_H$ is described by Eq. (3.5) so that this is not a measured peak speed in the experiment; rather, it is a statistical peak value computed using a constant peak factor. Typically, lower wind speeds were required for shingles because of their light weight and the subsequent tendency to travel relatively long distances, as discussed in Chapter 3. Since the hold-down forces were not intended to model absolute failure loads, the failure velocities should not be compared between the shingle and tile experiments.

In what follows, any roof position with the associated surroundings and wind direction will be labelled as position_pattern_wind-angle, such as E_I_0, which means position E (as shown in Fig. 3.3a), with surroundings pattern I, and a wind direction of 0^{o}.

The initial conditions for failure and debris flight are set by the building aerodynamics in the atmospheric boundary layer. The mean failure wind velocity for different positions on the roof vary, even though the hold down force was held constant (for most of the configurations), since the pressures depend on location on the roof. For example, many of the highest failure wind velocities were observed for position F (on the leeward side of the ridge). Tiles and shingles located at this position either stayed on the roof for the range of velocities tested or failed at amongst the highest wind velocities when compared to the other positions with the same hold down force. Thus, the aerodynamic load coefficient at failure, for position F, is amongst the lowest of the six positions for the two wind angles examined. In contrast, shingles at position B require the lowest failure wind speed (for the same hold down force). For the tiles at position B, a higher hold down force was used, which led to similar failure velocities as the other positions. Thus, the aerodynamic force coefficient at position B is amongst the largest for the positions examined herein.

The failure wind speeds for each particular configuration were nominally similar, with the ratio of $(\hat{U}_H)_\sigma / (\hat{U}_H)_{avg}$ typically less than ~10% for most, although not all, of the configurations. This variation is primarily due to the turbulent gusts - since turbulence is a stochastic process, particularly strong gusts may or may not happen during the 10 minute (equivalent full-scale) time increment prior to the next mean wind tunnel speed change. The failure wind velocities were observed to fit the Gumbel distribution, in agreement with Visscher and Kopp (2007).

Table 4.1: Summary of the results (in equivalent full-scale dimensions).

	Configuration	$(U_H)_{avg}$ (km/hr)	$(\hat{U}_H)_{avg}$ (km/hr)	$(\hat{U}_H)_\sigma$ (km/hr)	Impact Location for those that flew (m)				Flight Pattern (%)				
					X_{avg}	Z_{avg}	X_σ	Z_σ	Autorotational	3D spinning	Translational	Falling	No flight
Tiles	A_I_45	130	185	30	36.7	2.4	21.9	5.7	0	88	8	0	4
	B_I_45	150	210	15	37.6	-8.3	21.2	4.9	0	83	7	3	7
	B_II_45	160	225	-	37.5	-7.8	21.9	3.4	0	80	0	7	13
	B_III_45	145	210	-	29.7	-7.7	18.3	3.3	3	77	10	10	0
	C_I_45	115	165	15	17.4	-8.2	13.4	5.4	0	18	7	21	54
	D_III_45	125	175	10	18	10.6	6.9	3.0	0	75	13	12	0
	E_I_0	125	180	5	23.3	2.3	13.1	2.6	4	61	0	14	21
	E_II_0	170	240	30	33.1	3.4	13.2	4.9	0	95	5	0	0
	F_I_0	-	-	-	-	-	-	-	0	0	0	0	100
	F_II_0	-	-	-	-	-	-	-	0	0	0	0	100
	F_I_45	135	195	10	19.8	0.8	2.2	1.1	0	3	0	3	94
	F_II_45	160	230	25	30	-3.4	10.4	1.8	0	55	0	4	41
Shingles	A_I_45	115	165	15	103	-2.3	31.7	7.8	10	83	7	0	0
	B_I_45	70	100	5	44	-9.9	13.1	5.6	3	94	3	0	0
	B_II_45	70	100	10	30.9	-6.9	13.4	4.2	0	80	3	14	3
	B_III_45	60	90	5	26.6	-5.7	7.6	3.2	7	86	0	7	0
	C_I_45	85	120	5	43.5	-5.8	12.2	4.1	0	77	10	13	0
	D_I_0	90	125	5	51.4	-0.6	23.6	4.7	0	37	17	0	46
	D_II_0	90	125	5	29.6	-1.3	13.8	5.9	0	68	19	13	0
	D_III_45	100	145	5	38.1	1.5	17.7	8.4	0	53	25	9	13
	E_I_0	90	125	15	78.4	1.6	22.6	8.3	19	81	0	0	0
	E_II_0	80	115	5	46.7	1.4	15.1	4.3	3	90	7	0	0
	F_I_0	120	170	5	43.1	1.7	34.2	6.5	0	33	0	20	47
	F_II_0	120	170	10	25	0	34.4	3.8	0	33	10	54	3
	F_I_45	-	-	-	-	-	-	-	0	0	0	0	100
	F_II_45	-	-	-	-	-	-	-	0	0	0	0	100

4.2 Fight Patterns

The observed flight trajectories usually followed complex patterns. We have categorized these into the following six categories: auto-rotational, 3D spinning, translational, falling, and "no flight", based on observations of the high speed video recordings. Our definitions of these patterns are:

- The auto-rotational mode involves "pure" rotation about the axis of the debris parallel to the z-direction (or parallel to the ridge for wind from 0^{o}). This is a category that is useful for the two-dimensional flight described in the literature (e.g., Tachikawa 1983; Holmes et al. 2006), since it is associated with additional lift due to the Magnus effect.
- The 3D spinning mode is a mixture of rotation in any direction or "pure" rotation around any axis other than the "auto-rotational" axis.
- The translational mode involves translation of the model in the flow without having significant rotation, or it has reversing directions of rotation, (which we have arbitrarily included as translational), similar to Visscher and Kopp's (2007) classification.
- The falling mode is the case that the debris element falls almost directly (vertically) to the ground in the wake of the house without having significant horizontal velocity at impact.
- "No flight" is the case where the model stays or lands on the roof immediately following the failure.

Table 4.1 presents the type of flight patterns observed for each configuration. We observed that the most common case for shingles and tiles is the complex three-

dimensional motion, "3D spinning". This is not surprising since the models are three-dimensional and have six degrees of freedom (three translational and three rotational). Their relatively light weight compared to, say, sheathing, also plays a role, where sheathing tests indicated greater numbers of two-dimensional motion, at least for the normal (0^o) wind direction studied by Visscher and Kopp (2007).

The second most common flight pattern was "no flight". This occurred primarily at positions F, in the middle of the leeward roof, and D, at the windward edge of the roof on the building centerline. The reasons for this will be examined later in the paper. Autorotational, translational, and falling patterns each were observed in less than 25% of the shingle and tile tests, except for shingles in position F_II_0 where more than half of the time the shingles fell down. In particular, less than 7% of the shingles and tiles demonstrated the autorotational pattern. The exception to this was shingles in positions E_I_0 and A_I_45, where they experienced autorotational motion over a significant portion of their trajectory, about 45% of the time. Further details regarding the flight patterns can be found in Kordi and Kopp (2008).

4.3 Flight Trajectory Distances

The impact location for each test was extracted from the high speed video using the grid lines taped on the floor of the wind tunnel. The average, $(.)_{avg}$, and standard deviation, $(.)_{\sigma}$, of the longitudinal, X, and lateral, Z, impact locations for each configuration is tabulated in Table 4.1. Fig. 4.1 and Fig. 4.2 show the impact locations of the shingles initiating from the various configurations listed in Table 4.1 for wind angles of 0^o and 45^o. Fig. 4.3 shows the impact locations of tiles initiating from the various

initiating from the various configurations, for a wind angle of 45°. As can be seen from these figures, there is significant variability on the flight distances from a single given initial condition, as well as significant differences in overall trajectories for the various configurations.

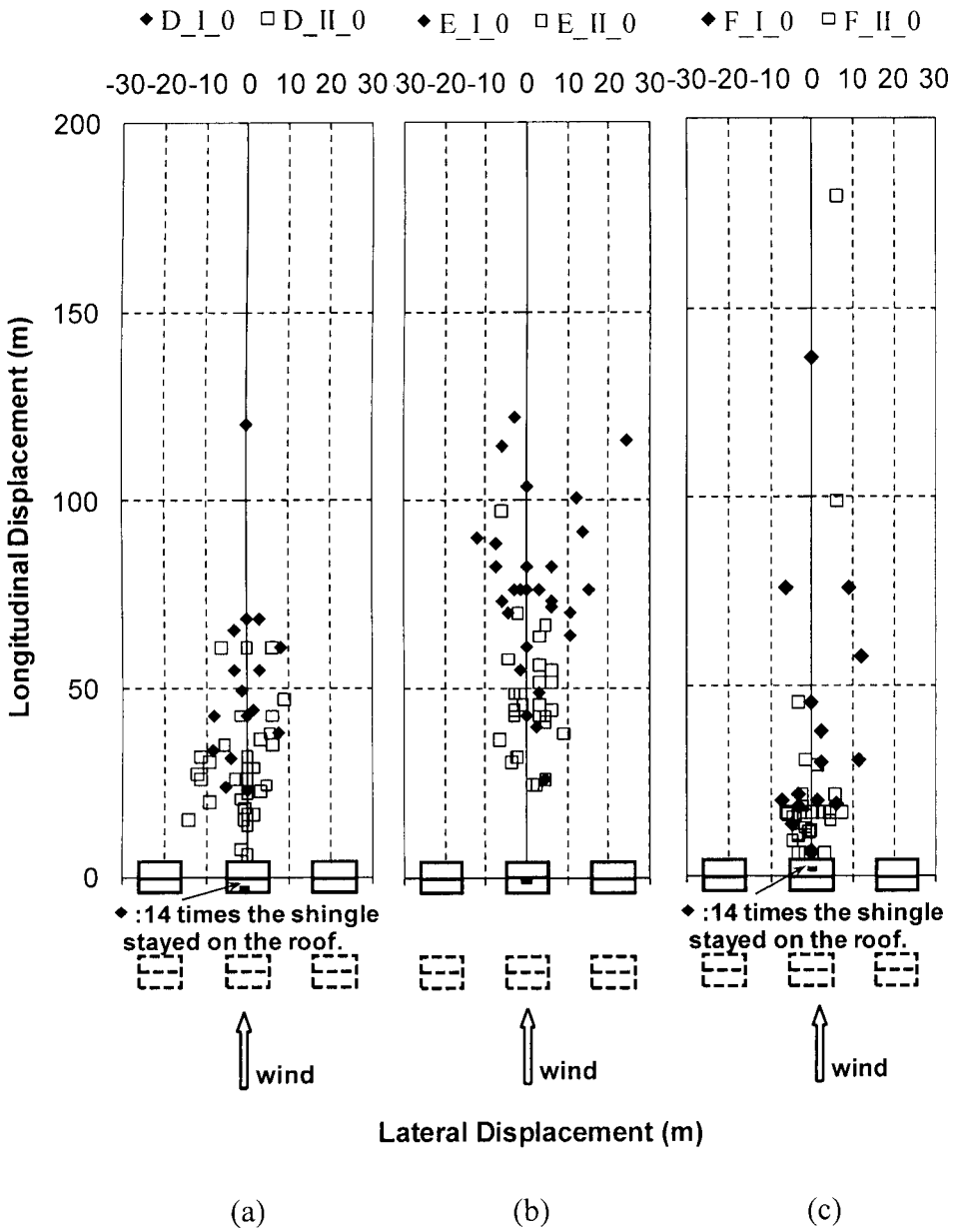

Fig. 4.1: Measured flight distances for shingles for several configurations: (a) D_I_0 and D_II_0, (b) E_I_0 and E_II_0, and (c) F_I_0 and F_II_0.

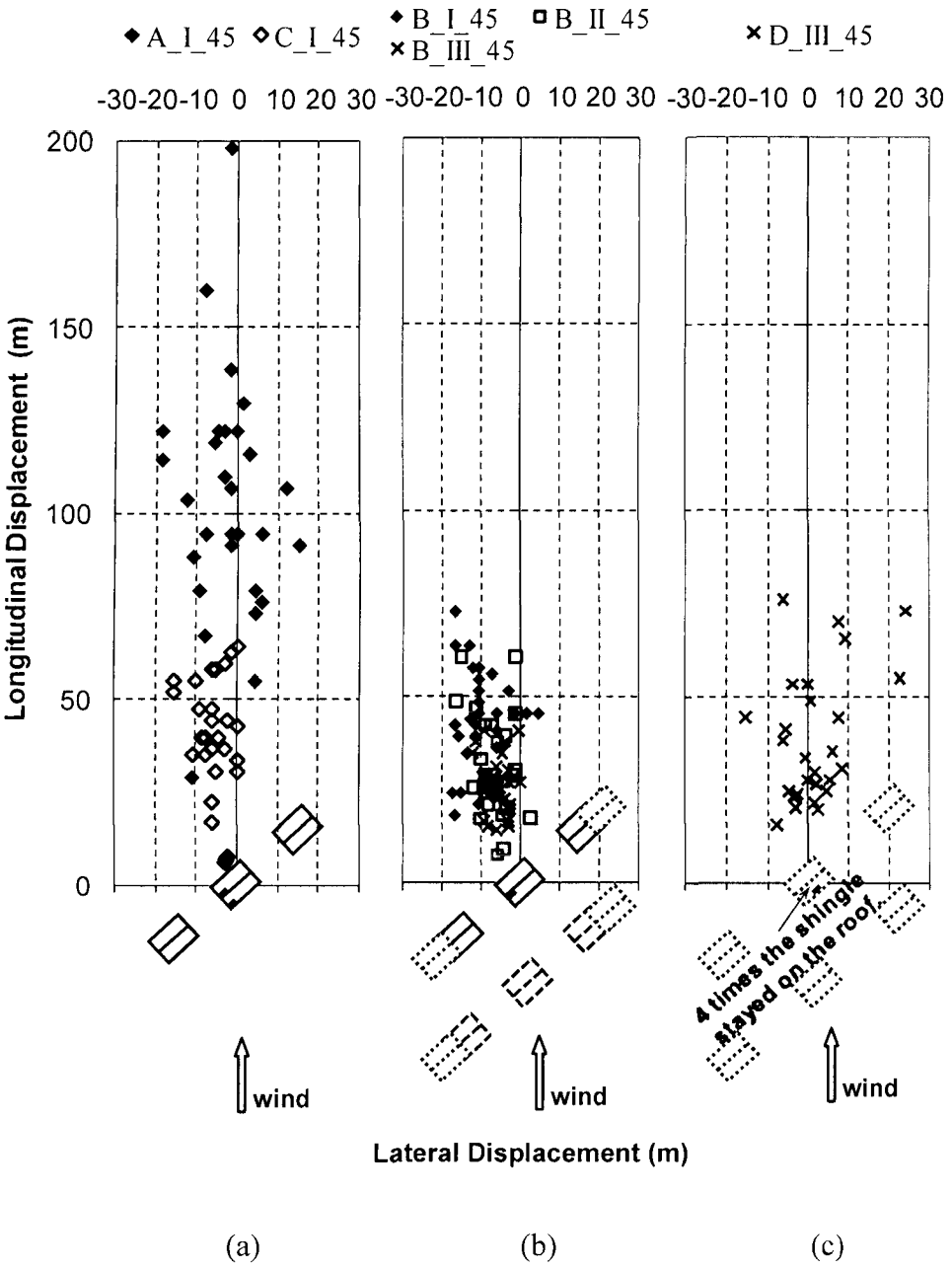

Fig. 4.2: Measured flight distances for shingles for several configurations: (a) A_I_45 and C_I_45, (b) B_I_45, B_II_45, and B_III_45, and (c) D_III_45.

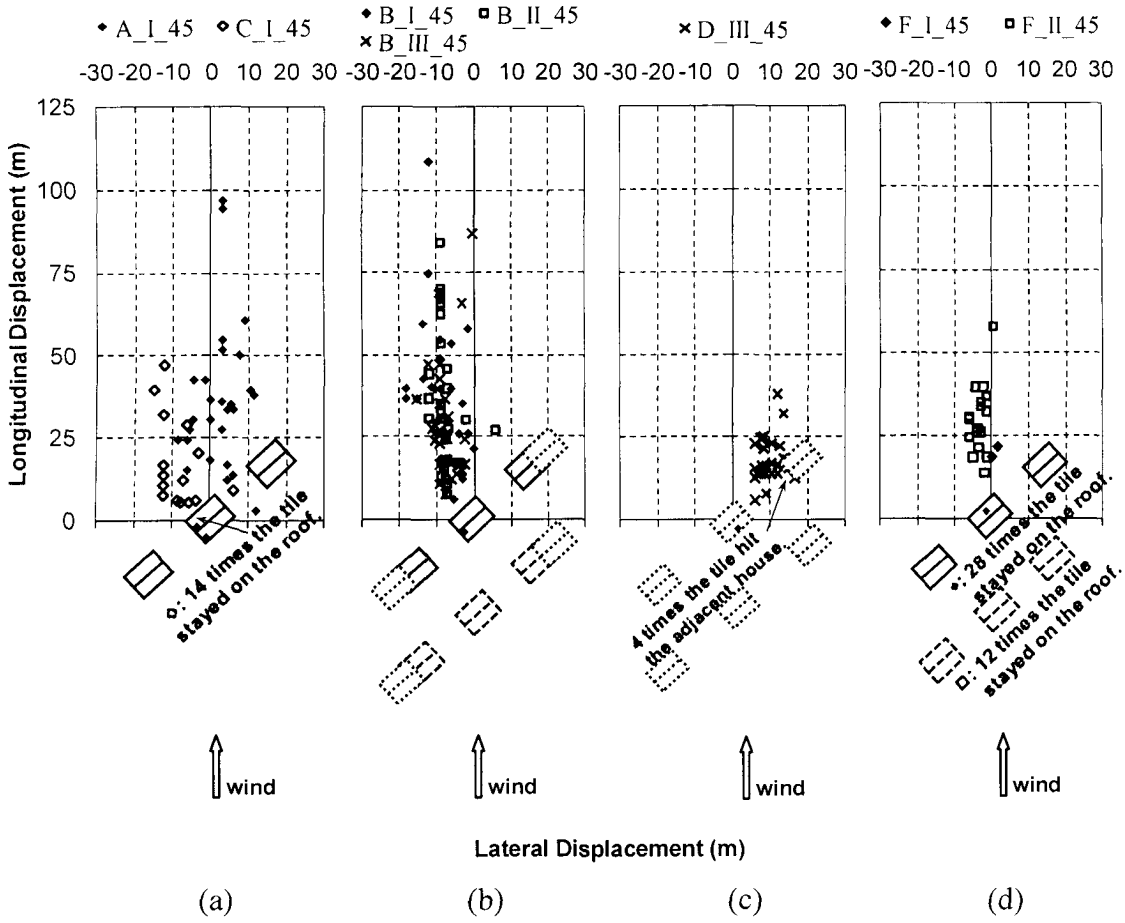

Fig. 4.3: Measured flight distances for tiles for several configurations: (a) A_I_45 and C_I_45, (b) B_I_45, B_II_45, and B_III_45, (c) D_III_45, and (d) F_I_45 and F_II_45.

Consider the clusters of data points in Fig. 4.1, for example. In this figure, data from three roof locations, for two sets of surroundings and one wind direction are presented. Clearly, both the location of the envelope of data points for each configuration, as well as the size of the envelope of data points are dependent on the detailed initial conditions. There are interesting aspects, such as configuration F_II_0 where the range of flight distances is from 0 to 170m (equivalent full-scale) in contrast to D_II_0, where the range is 0 to 60m. However, most of the F_II_0 data are between 0 and 20m, while for

D_II_0 the majority are between 20 and 60m. Thus, the details are very sensitive to the conditions at 'failure' and during the subsequent flight, which, in this example, lead to distributions that are skewed in opposite directions. So, for a given debris element, the combination of the initial location on the roof, the variability of turbulent gusts, the details of the local velocity field around the house and roof, the fixture strength integrity and the proximity of neighbouring houses were all found to have an effect on the flight trajectories and impact locations. These factors will be examined in detail below.

4.3.1 Relationship between Failure Velocity and Impact Location

All published work to date on the aerodynamics of windborne debris links flight distance with a gust speed so that the greater the wind speed, the further downstream the impact location. For example, having the uniform flow results in mind, like those of Tachikawa (1983) and Lin et al. (2006), one would expect the highest failure speed to result in the greatest flight distance. As the results show, this is not always the case for debris originating from different locations on the roof or with different surroundings. First, Fig. 4.1 shows the results for shingles at positions D, E, and F with a wind direction of 0 degrees. The shingles are along the centerline of the house and have the same hold down force. The mean failure wind velocity of position E is the same as position D and both are much lower than position F, but shingles originating from position F fly on average the shortest distance, while those from position E fly the longest. Second, for a wind direction of 45 degrees, tiles at positions A and C are along the windward edge of the house and have the same hold down force. The failure wind velocity for both of the configurations are similar, but those at position A fly much farther than those originating

at position C. Third, the failure wind velocity of shingles for C_I_45 is higher than those on B_I_45 but the shingles at position C travel less distance on average. Fourth, the hold down force and failure velocity of tiles for A_I_45 is lower than those for B_I_45, but they both fly the same distance on average. Finally, tiles for F_I_45 have a failure velocity in the range of the other configurations but most of them do not fly at all and land on the roof immediately after failure. These results are all contrary to the expectations for uniform flow.

4.3.2 Turbulent Gusts

The impact location of debris originating from the same nominal initial condition (hold down force, position on the roof, and neighbourhood) varies test by test. It may appear that the variation in the impact locations is mostly due to failure velocity, $\hat{U}_H$, variations in different tests, but this is not necessarily the case. Fig. 4.4 shows the distribution of the shingle and tile tests for the configurations A_I_45 and C_I_45 in a X-$\hat{U}_H$ plane, where X is a longitudinal impact location. As can be seen, there is generally no correlation between the impact location and failure velocity. Thus, debris in the same configuration, but failing at a higher velocity, does not necessarily fly further. This could be because the failure gust velocity is presumed to have the same relationship to mean speeds every time. However, the gust duration may be different relative to the response time of the debris, or details of the gust structure may different, resulting substantial variations, following the failure-inducing gust. This will be discussed further, later in the paper.

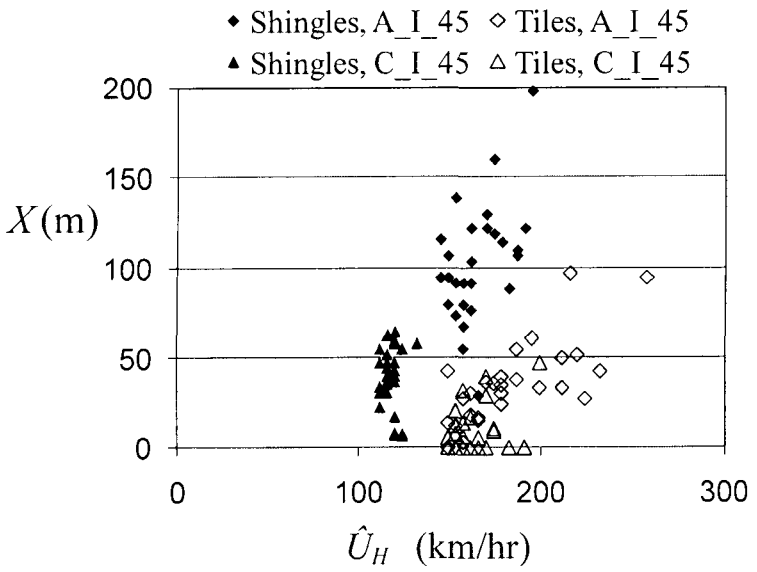

Fig. 4.4: Failure velocity vs. the longitudinal impact location in equivalent full scale for tile and shingle testings for A_I_45 and C_I_45.

4.3.3 Local Wind Field

The local flow field has an important effect on the impact locations. Fig. 4.1 shows that unlike shingles originating from position E, half of the shingles from positions D and F (with no upstream houses) land on the roof immediately after failure. The typical initial failure patterns for shingles located at positions D, E, and F, with no upstream houses and a wind direction of 0 degrees, are shown in Fig. 4.5. As can be seen, two different initial failure patterns are observed for shingles from positions D and F; they either land on the roof immediately after failure, or travel downstream with the main flow. However, just one pattern was observed for shingles from position E. In addition, shingles from positions D and F initially rotate upstream after failure. Fig. 4.6 illustrates the flow field above the roof schematically for this wind direction. As the figure shows, the shingles from positions D and F are within the separation bubbles at the leading edge and ridge,

respectively, so that the local surface flow is actually upstream (e.g., towards the ridge for F). Thus, when failure occurs due to high suctions, they drift slightly upstream. However, if they elevate sufficiently, they can be caught up in the high speed flow of the separated shear layer and travel downstream; otherwise, they land on the roof after failure. In contrast, shingles from position E are in high speed reattached flow; they initially rotate downstream and continue their flight in the high speed separated shear layer. As a result shingles starting from position E fly much farther than shingles originating from positions D and F even though the mean failure wind velocity of position E is the same as that of position D and much lower than that of position F. This demonstrates that variability in the results begins from the initial failure pattern, which is governed by the local flow field.

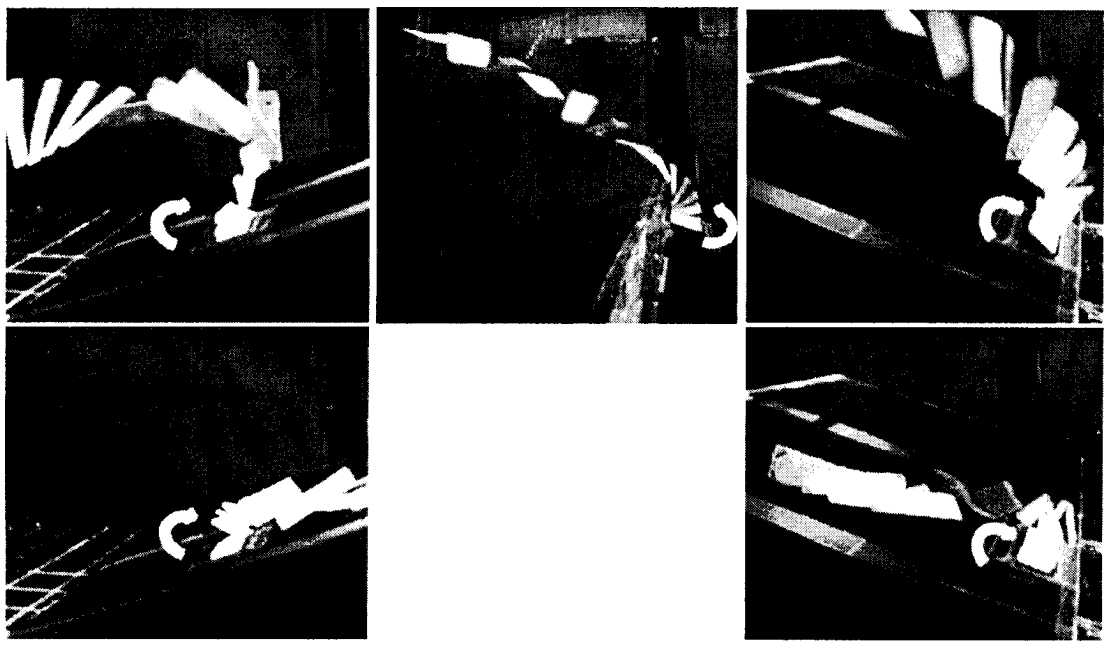

(a) (b) (c)

Fig. 4.5: Strobe images constructed from high speed video of the initial flight patterns of the roof shingles located at (a) position F, (b) position E, and (c) position D. Wind direction is 0°, from right to left in the images.

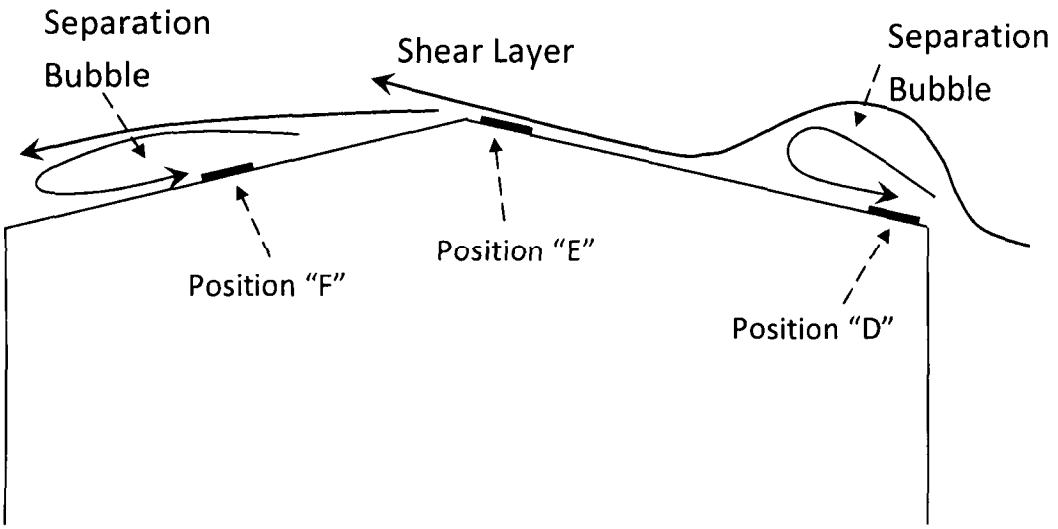

Fig. 4.6 Schematic sketch for the local flow field over the center of the house. Wind direction is 0°, from right to left.

4.3.4 Fixture Strength Integrity

The hold down force plays a significant role, as first pointed out by Wills et al. (2002). Fig. 4.7 shows typical initial failure patterns for tiles located at positions D, E, and F with no upstream houses and a wind direction of 0 degrees. A hold down force of zero (i.e., only the weight) was used for the tiles in these configurations. Like shingles at position D, two different flight patterns were observed for the tiles at position D; they either land on the roof immediately after failure or are carried away with the main flow. It is interesting that the tiles at position D do not rotate upstream like their shingle counterparts; rather, they sometimes slide down until they reach the ridge and sometimes rotate sidewise. Tiles at position E, unlike shingles, are not always carried downstream with the flow, sometimes they fall on the roof or close to the house. The impact location of tiles on E_I_0 is shown in Fig. 4.8. Unlike shingles, no tiles from position F were able

to escape the separation bubble; they just rotate upstream, land on the roof, and stay there.

Wills et al. (2002) defined the concept of fixture strength integrity, I', which is the wind force required to break objects loose divided by the object's own weight. They point out that for debris which is loosely held down, say under its own mass, (I'=1), that, as it begins to fly it accelerates lowering the relative velocity and the aerodynamic force so that it can fall back to the ground. In contrast, for an object that is held down with significant resistance, (I'>1), once it breaks free it accelerates in a high speed flow and stays airborne for a much longer distance. The fixture strength integrity for the tiles and shingles at positions D, E, and F (with no upstream houses) are 1 and 3.5, respectively. Perhaps that is why almost half of the tiles from position E tend to fall back down, while all of the shingles travel away. This might also explain why none of the tiles from position F has the power to leave the roof. The impact locations of tiles with fixture strength integrity of 2.2 located on E_II_0 are also shown in Fig. 4.8. As this figure shows, all of the tiles clear the roof. Therefore, the fixture strength integrity has direct effect on the distance the debris travels from a certain location, although this relationship is clearly complicated by the local flow field effects.

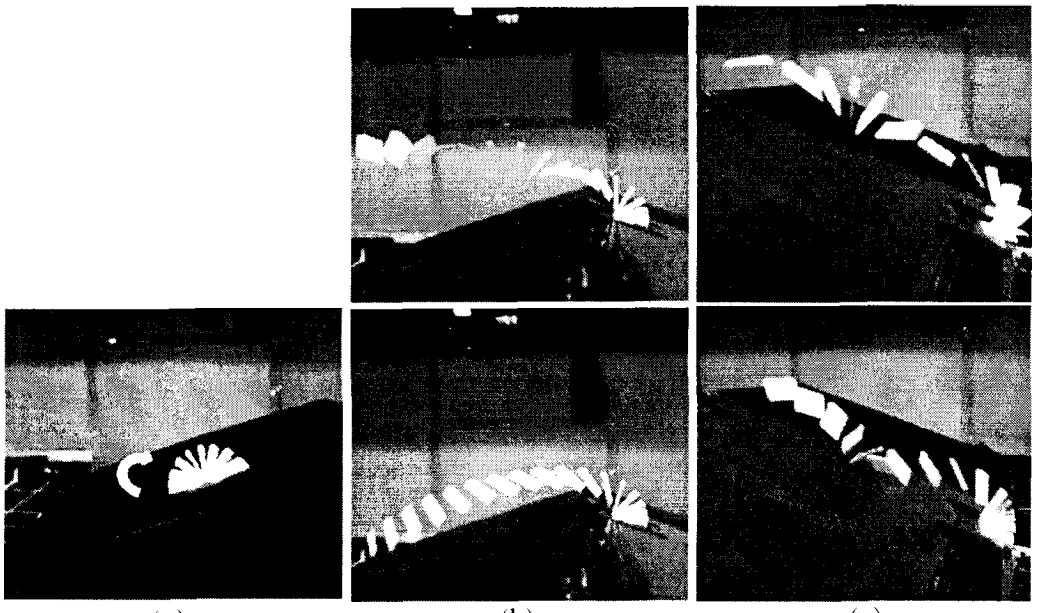

(a) (b) (c)

Fig. 4.7: Strobe images constructed from the high speed video of the initial flight patterns of the roof tiles located at (a) position F, (b) position E, and (c) position D. Wind direction is 0^{0},from right to left in images.

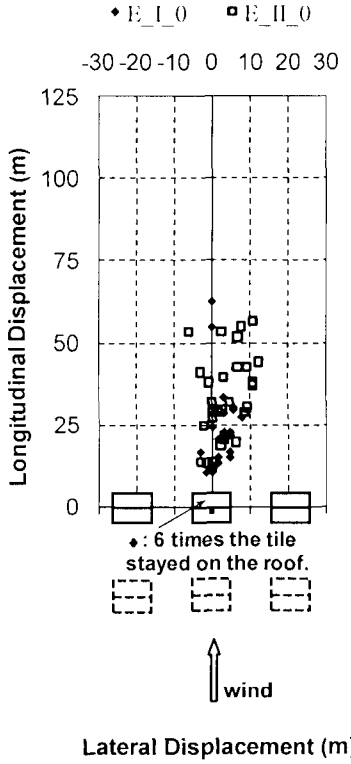

Fig. 4.8: Measured flight distances for tiles located at E_I_0 and E_II_0.

4.3.5 Neighbouring Houses

The addition of upstream houses plays a role in the debris trajectories, as well. Again, several observations from the data can be made. First, an upstream row of houses must change the local wind speeds and directions. As can be seen in Fig. 4.1, no shingles from positions D and F, with an upstream row of houses, landed on the roof after failure, while half of the shingles landed on the roof when the upstream houses were removed. The same trend occurs for tiles located at positions F, with a wind direction of 45 degrees (Fig. 4.3). Almost all of the tiles from locations F, with no upstream houses, landed on the roof immediately after failure; however, the addition of upstream houses decreased the number to less than half (Fig. 4.3(d)). Second, the upstream row also increases the size of the wake behind the debris-source house, which lowers flight distances. For example, the shingles from certain locations, with the same hold down force, whose failure velocity has only slightly changed with the addition of upstream row of houses, like those on positions B, D, and F (which were able to escape the separation bubble on the roof), have shortened trajectories(Fig. 4.2(b) and Fig. 4.1(a,c)). Third, the failure wind velocity for tiles and shingles at certain locations, with the same hold down force, can either decrease or increase with the addition of upstream houses. Thus, the aerodynamic force coefficients change with the addition of upstream row of houses. Clearly, the flow field above and around the house is significantly altered by the presence of upstream and neighbouring houses and this has a significant effect on the subsequent debris flight. This is relatively complex and detailed flow measurements would be helpful and are being considered for future work.

4.3.6 Wind Direction

Wind direction changes the local flow field above the roof in a complex way because of changes in the flow and vortex structure. Several observations regarding the debris flight can be made. First, tiles at position F, with the wind direction of 0 degrees do not fly, but they tend to fly if the wind direction is 45 degrees. In contrast, shingles at position F, with the wind direction of 0 degrees tend to fly, but they do not fly with the wind direction of 45 degrees. Second, while the addition of upstream row of houses distorts the local wind speed in a way that none of the shingles from D_II_0 land on the roof after failure, the change in the wind direction reverses the situation as four of the shingles from D_III_45 land on the roof after failure. Third, the effect of wind direction is different for tiles and shingles. The tiles on D_III_45 mostly follow the same direction, toward the adjacent house, while shingles on D_III_45 spread much more. We have no explanation for these effects, at this time, but they perhaps indicate the complex interdependence of the variables governing this problem. Again, detailed velocity field measurements may help, but they are not available at this time.

4.4 Debris Flight Speeds

The horizontal and vertical location of the tiles and shingles were extracted from the high speed video frames as a function of time. Each set of the longitudinal and vertical locations was mathematically fit to a polynomial function of time using least squares regression. The horizontal (longitudinal), u, and vertical, v, velocities of shingles and tiles were obtained by differentiation of the curve fit, and the magnitude of the

translational velocity, $u_{mag}=(u^2+v^2)^{0.5}$, was also calculated. Further details can be found in Kordi and Kopp (2008). All the values are non-dimensionalized according to Baker's (2007) formulation: horizontal displacement ($\bar{x}=x\cdot\phi/l$), vertical displacement ($\bar{y}=y\cdot\phi/l$), time ($\bar{t}=t\cdot\hat{U}_H.\phi/l$), horizontal velocity ($\bar{u}=u/\hat{U}_H$), vertical velocity ($\bar{v}=v/\hat{U}_H$), magnitude of translational velocity ($\bar{u}_{mag}=u_{mag}/\hat{U}_H$), where ϕ is the buoyancy parameter ($\phi = 0.5\rho_{air}\cdot A\cdot l/m$), A, m, l, are the area, mass, and length of the shingle or tile, respectively, and ρ_{air} is the density of air.

Fig. 4.9 shows the results of $\bar{y}$, $\bar{u}$, and $\bar{v}$ versus $\bar{x}$ for all of the tile and shingle tests while Fig. 4.10, Fig. 4.11, and Fig. 4.12 show the results for shingles in the selected configurations A_I_45, B_I_45, C_I_45, D_I_0, E_I_0, B_III_45, D_II_0, and E_II_0. Note that there were cases where the shingles or tiles flew out of the camera range and we were not able to extract the entire trajectory from the video images; thus, for those cases the results for only a portion of the trajectory are presented. The exception is for the figure showing the results of A_I_45 where the grey points show the calculated trajectory and velocities based on the fitted curve to the trajectory and the impact location. The non-dimensional elevation of the eave and ridge heights are shown by the two broken lines at $\bar{y}_{eave}$=0.665 and $\bar{y}_{ridge}$=0.865 for the shingles and at $\bar{y}_{eave}$ =0.102 and $\bar{y}_{ridge}$ =0.133 for the tiles. Note that the non dimensional horizontal and vertical distances of 14 and 2.2 for shingles and 2 and 0.35 for tiles are almost equivalent to the horizontal and vertical distances of 125 m and 20 m, respectively.

Table 4.2: Summary of impact velocity results.

	Configuration	$(\bar{u}_{mag\text{-}eave})_{avg}$	$(\bar{u}_{mag\text{-}eave})_{\sigma}$	$(\bar{u}_{mag\text{-}ground})_{avg}$	$(\bar{u}_{mag\text{-}ground})_{\sigma}$
Tiles	A_I_45	0.51	0.10	0.55	0.1
	B_I_45	0.46	0.12	0.48	0.14
	B_II_45	0.38	-	0.40	-
	B_III_45	0.42	-	0.50	-
	C_I_45	-	-	-	-
	D_III_45	0.37	0.08	0.39	0.06
	E_I_0	0.28	0.06	0.32	0.08
	E_II_0	0.38	0.08	0.39	0.08
	F_I_0	-	-	-	-
	F_II_0	-	-	-	-
	F_I_45	-	-	-	-
	F_II_45	0.38	0.10	0.49	0.14
Shingles	A_I_45	0.83	0.22	0.88	0.29
	B_I_45	0.88	0.26	0.99	0.51
	B_II_45	0.64	0.18	0.61	0.18
	B_III_45	0.70	0.16	0.74	0.25
	C_I_45	0.73	0.15	0.73	0.24
	D_I_0	0.63	0.09	0.63	0.14
	D_II_0	0.52	0.12	0.52	0.17
	D_III_45	0.58	0.15	0.55	0.20
	E_I_0	0.77	0.23	0.74	0.31
	E_II_0	0.66	0.13	0.60	0.22
	F_I_0	0.43	0.11	0.43	0.09
	F_II_0	0.36	0.09	0.38	0.09
	F_I_45	-	-	-	-
	F_II_45	-	-	-	-

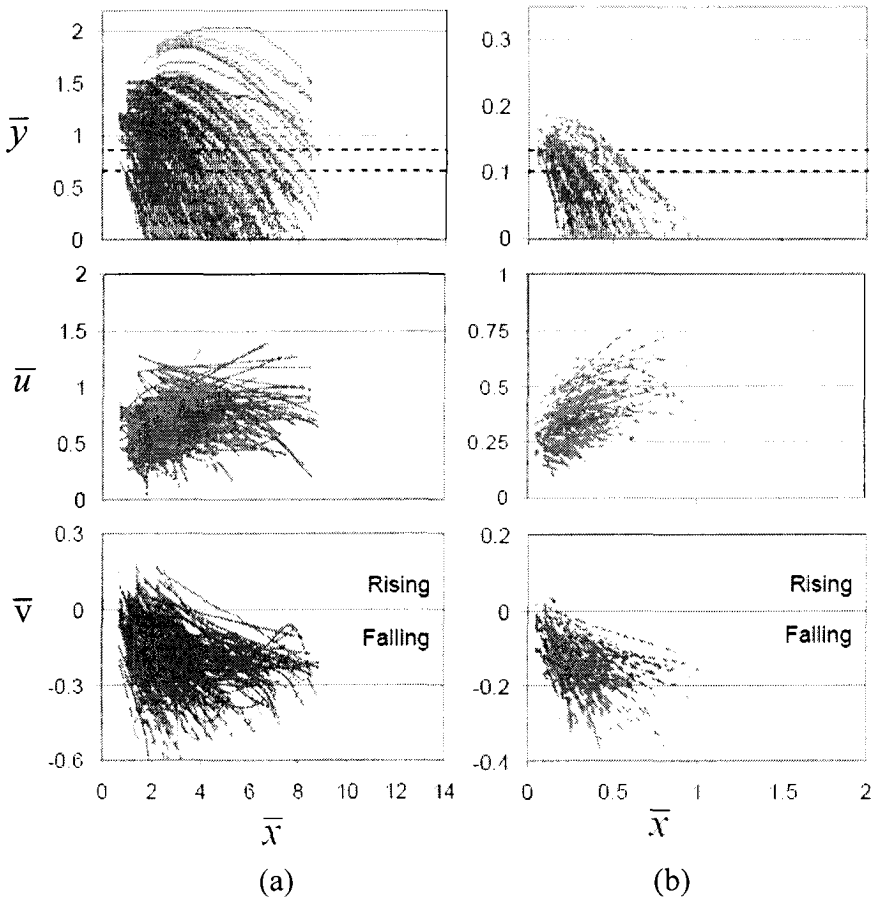

Fig. 4.9: Non-dimensional trajectories and horizontal and vertical velocity components for all measured (a) shingle and (b) tile flights.

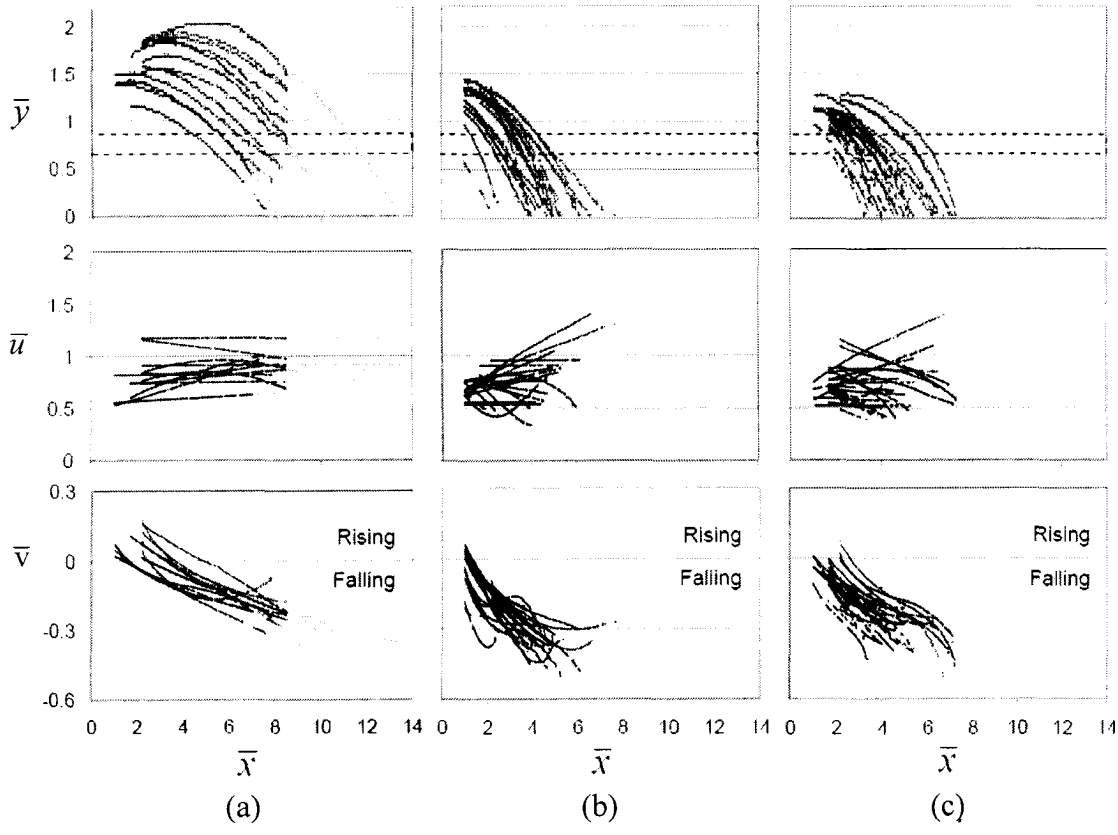

Fig. 4.10: Non-dimensional trajectories and horizontal and vertical velocity components of shingles in configurations (a) A_I_45, (b) B_I_45, and (c) C_I_45.

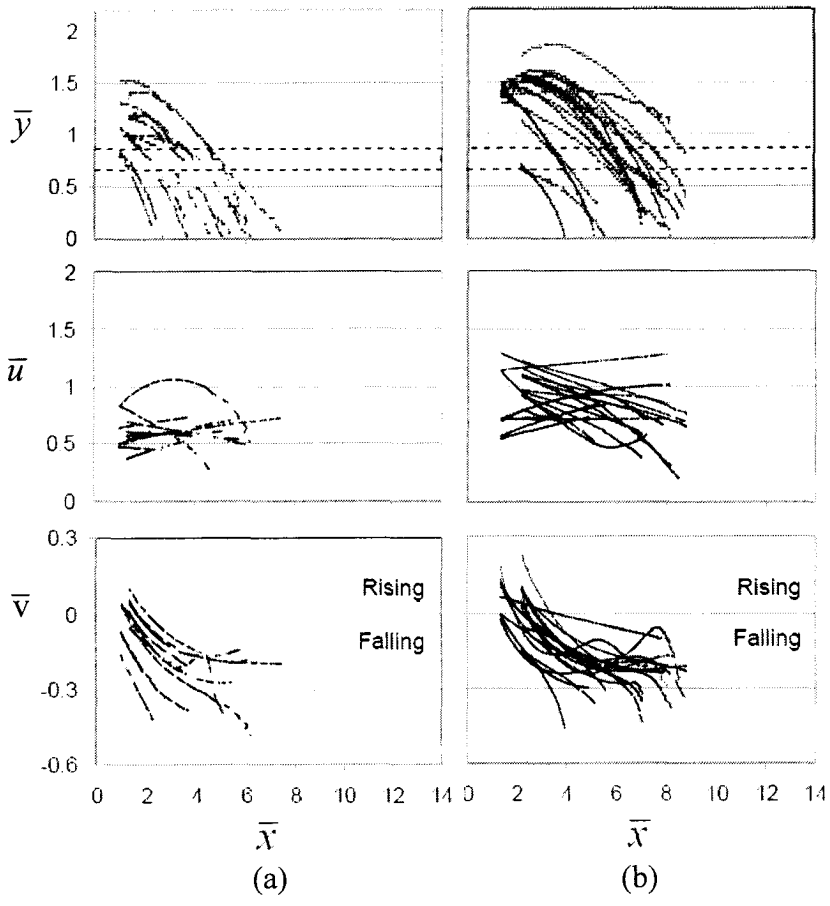

Fig. 4.11: Non-dimensional trajectories and horizontal and vertical velocity components of shingles in configurations (a) D_I_0 and (b) E_I_0.

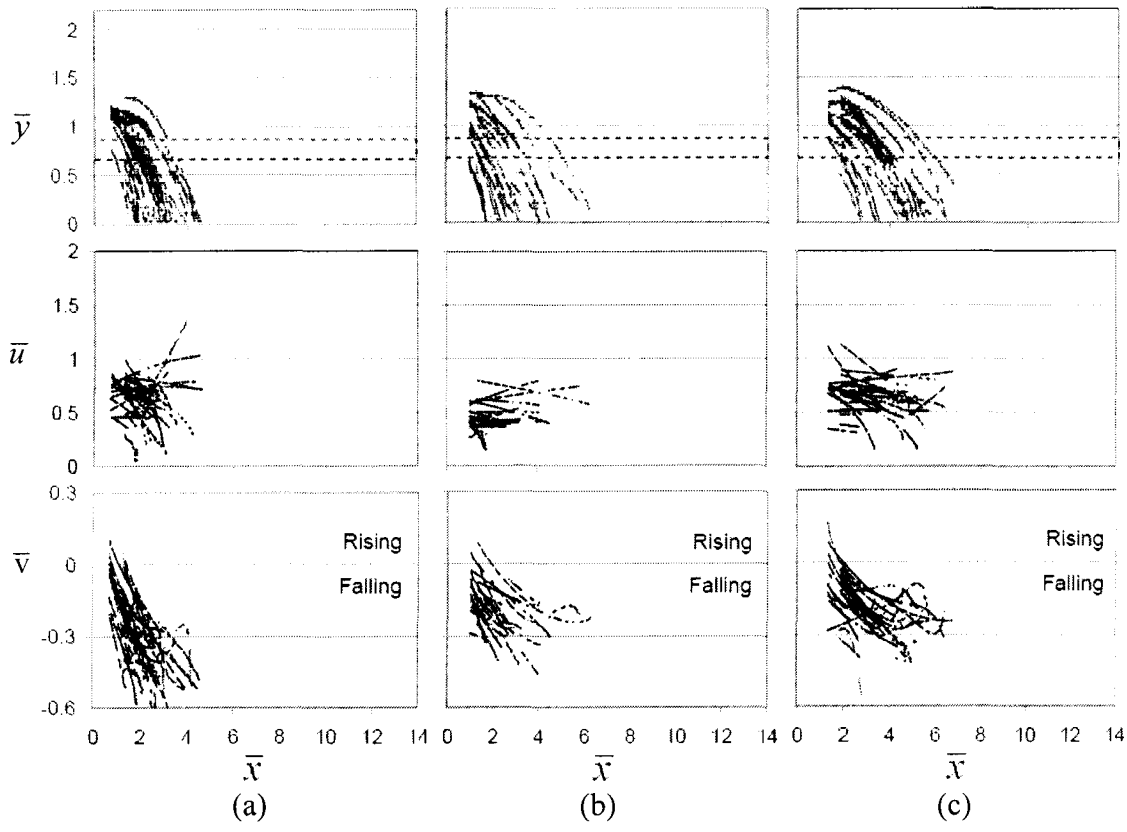

Fig. 4.12: Non-dimensional trajectories and horizontal and vertical velocity components of shingles in configurations (a) B_III_45, (b) D_II_0, and (c) E_II_0.

4.4.1 Range of Impact Velocities

The translational velocity of debris indicates the energy it possesses. The translational velocity at two important points, the eave height (on the way down) and the ground level, were investigated in detail. Table 4.2 gives a summary of the non-dimensional impact velocity results for tiles and shingles at the eave height, $\bar{u}_{mag\text{-}eave}$, and at the ground level, $\bar{u}_{mag\text{-}ground}$ for each configuration. Included in the summary are the mean and standard deviation of the speeds for each configuration. One of the important results is that the magnitude of shingle and tile velocities at the eave height spans a range

from 40% to 90% and 30% to 50% of the upstream 3 second gust speed, respectively. In addition, as Fig. 4.9 shows, the magnitude of shingle velocity during the flight reaches at least half of the undisturbed 3 second gust speed, and up to 120% of the full value. Tile velocities, in contrast, cover the range of 30% to 60% of the upstream 3 second gust speed, at some point during their trajectories.

4.4.2 Height and Duration of Flight

Some select results for the shingle configurations were chosen for comparison in Fig. 4.10 and Fig. 4.11. It can be observed that the combination of the initial location on the roof, initial vertical velocity, height of the flight, and the duration of flight have an effect on the translational velocity of the debris.

One important observation is that there are many instances where shingles fly faster than the estimated failure gust speed. This primarily depends on the initial location on the roof. For instance, (i) A_I_45, B_I_45, and C_I_45 are along the windward edge of the house and have the same hold down force. The shingles from positions B and C have almost the same trajectory and failure speed, but the flights initiated from position A require a higher failure speed and fly much higher and faster as a result. (ii) The mean failure velocity of the shingles on E_I_0 is the same as those on D_I_0 but the translational velocity of those at position E is much higher than those at D. Thus, the local velocity field, which is set by the location on the roof, has an important effect on the translational velocity of the debris element.

The second important observation is that the higher and longer the flight, the farther and faster the flight. The two configurations A_I_45 and E_I_0 are the two extreme cases

for the translational velocity of shingles, where the shingle flies about, or even faster, than the estimated failure gust speed. They are also the two extreme cases for the impact locations. Comparing the results of the shingles on A_I_45 and E_I_0 with the rest of the configurations demonstrates that the ones from positions A and E attain higher initial vertical velocity which helps them to fly higher and remain airborne longer. This eventually results in the higher relative translational velocity.

4.4.3 Neighbouring Houses

The presence of upstream houses also plays a role on debris flight speeds. Comparing the shingles originating from the same position but different neighbourhood patterns (such as position B with pattern I and III, and positions D and E both with patterns I and II), all tested with the same hold down force and failure wind speed, shows that the upstream row of houses (i) decreases the initial positive vertical velocity, (ii) increases the descent velocity, and (iii) decreases the horizontal velocity. All of these result in a shorter and lower trajectory. This is because of the blockage induced by the upstream houses, which makes a larger wake behind the debris-source house. Thus, the shingles initiating flight from a single row of houses tend to have higher, longer, and faster trajectories.

4.5 Conclusions

Earlier researches have primarily focussed on the three degree-of-freedom flight of debris elements in uniform, smooth flow. The objective of the present work is to determine how realistic initial conditions, surroundings, and turbulence affect the flight of

two common types of 'plate' debris. In particular, shingle and tile flight, originating from a typical house in typical neighbourhoods, is examined. Details on the modes of flight, distance travelled and flight speeds were examined for a range of initial locations, hold down forces and wind angles. As might be anticipated, given the large number of parameters governing the problem, there are complex relationships between initial location on the roof, hold down force, failure wind speed and flight distance. The main conclusions of the work are:

1- Three-dimensional spinning flight was by far the most common mode of flight. Relatively few cases were observed where the primary rotation was aligned to cause additional lift through the Magnus effect.

2- The second most common mode of flight, following failure, is for the element not to fly from the roof. This is due to the flow field at the point of failure being governed by the building aerodynamics and the flow separations and reattachments above the roof. The flow below the separation streamline is a vortex with the flow near the roof surface being in a direction against the main stream. In this local flow field, flight of elements is often not possible. Thus, for failures due to large suctions, it is possible to have many elements remain on the roof.

3- In other situations, the element is able to move upstream and gets caught up in the high speed flow associated with the separated shear layer near the point of flow separation. In this case, high speed, high elevation, trajectories are observed.

4- Because of the effects of the flow field above the roof, the debris failing in the highest wind speeds did not always travel the furthest.

5- Debris that travels higher, also travels faster and further. In general, debris initiating from a building with no structures upstream results in a higher, longer, and faster trajectory.

6- Debris with a higher fixture strength integrity, from a particular location, travels farther.

7- For shingles, typical flight speeds range between 50 – 120% of the estimated, mean roof height, (undisturbed) gust speed at failure. For tiles, the range is 30 – 60%.

References

Baker, C.J. (2007). "The debris flight equations." *J. Wind Eng. Ind. Aerodyn.* 95, 329-353.

Holmes, J.D., Letchford, C.W., and Lin, N. (2006). "Investigations of plate-type windborne debris- Part II : Computed trajectories." *J. Wind Eng. Ind. Aerodyn.* 94, 21-39.

Kordi, B., Kopp, G.A. (2008). A Wind Tunnel Study of Roof Shingle and Tile Flight. Boundary Layer Wind Tunnel Laboratory Report No. BLWT-SS10-2008, University of Western Ontario, ON, Canada.

Lin, N., Letchford, C., and Holmes, J.D. (2006). "Investigation of plate-type windborne debris. Part I. Experiments in wind tunnel and full scale." *J. Wind Eng. Ind. Aerodyn.* 94, 51-76.

Tachikawa, M. (1983). "Trajectories of flat plates in uniform flow with application to wind-generated missiles." *J. Wind Eng. Ind. Aerodyn.* 14, 443–453.

Visscher, B.T., and Kopp, G.A. (2007). "Trajectories of roof sheathing panels under high winds." *J. Wind Eng. Ind. Aerodyn.*, 95, 697-713.

Wills, J.A.B., Lee, B.E., and Wyatt, T.A. (2002). "A model of wind-borne debris damage." *J. Wind Eng. Ind. Aerodyn.* 90, 555-565.

5 FLIGHT RESULTS – ROOF SHEATHING PANELS

In this chapter the flight of model sheathing panels from a gable roof model house in a scaled turbulent boundary layer wind flow will be studied. The effect of five different wind directions will be examined. The impact locations and the translational velocities of the debris will be fully studied. (The experimental results of sheathing panel experiments conducted by Traczuk (2007) are re-examined in this chapter.)

5.1 Failure Wind Speeds

U_H and $\hat{U}_H$ are the 10 min (mean) and 3 sec (peak) gust speeds, respectively, at the mean roof height obtained from each test. Then, the means, $(\cdot)_{avg}$, and standard deviations, $(\cdot)_\sigma$, are obtained by averaging the test results for each configuration. These values are presented in Table 5.1. The results for the wind direction of 0 degrees, presented in Table 5.1, are those of Visscher and Kopp (2007).

The failure wind speeds of each test were nominally similar for each wind direction, with the ratio of $(\hat{U}_H)_\sigma$ / $(\hat{U}_H)_{avg}$ being less than ~4% for all of the wind directions. In addition, these speeds were observed to fit the Gumbel distribution (Traczuk, 2007). Since, the failure load is fixed, the variation is primarily due to the variability in the turbulent gusts inducing the wind loads. Since turbulence is a stochastic process, particularly strong gusts may or may not happen during the 10 minute (equivalent full-scale) time increment prior to the next mean wind tunnel speed change.

Nevertheless, given the relatively small value of $(\hat{U}_H)_\sigma$ / $(\hat{U}_H)_{avg}$, 10 min (in equivalent full-scale) appears to be an appropriate duration to capture the most significant peaks.

Since the panel was located on the roof of the house, the building aerodynamics define the initial conditions at the moment of "failure". By changing the wind direction, the aerodynamic loads vary. Thus, the mean failure wind speeds depend on wind directions. This has a substantial effect with a range of $(\hat{U}_H)_{avg}$ from 135 km/hr for 60° to 200 km/hr for 0°. Since the hold down force was kept constant for all tests, the result of the dependence of roof pressure coefficients on wind direction leads to these changing failure wind speeds.

Table 5.1: Summary of the results (in equivalent full-scale dimensions).

Wind Direction	$(U_H)_{avg}$ (km/hr)	$(\hat{U}_H)_{avg}$ (km/hr)	$(\hat{U}_H)_\sigma$ (km/hr)	Impact Location for those that flew (m)				Flight Patterns (%)			
				X_{avg}	Z_{avg}	X_σ	Z_σ	Auto-rotational	3D Spinning	Trans-lational	No Flight
0	140	200	7.9	33	5	19	5	25	0	75	0
15	114	162	5.1	36	2	12	5	28	55	17	0
30	104	147	5.8	43	9	9	3	0	100	0	0
45	102	144	5.3	31	11	15	4	0	100	0	0
60	95	135	N/A	13	10	6	4	0	18	0	82
75	135	192	N/A	-	-	-	-	0	0	0	100
90	121	172	N/A	-	-	-	-	0	0	0	100

5.2 Fight Patterns

Based on the observations from the two high speed cameras located beside and above the house, the observed flight patterns were placed into four categories: auto-rotational, 3D Spinning, translational, and no flight. These categories, which are the same as what was defined in the previous chapter, are re-defined here for clarity:

- Autorotational – The panel rotates about its longer axis, which should remain almost parallel to the z-axis during the flight. This flight pattern is associated with additional lift due to the Magnus effect and is also defined in the literature by Tachikawa (1983), Holmes et al. (2006).
- 3D spinning – The panel rotates about different axes, or about any axis other than the "auto-rotational" axis. The rotation about the longer axis when it is not parallel to the z-direction is also in this category.
- Translational - The panel translates in the flow without significant rotation.
- No Flight - The panel stays or lands on the roof immediately after failure.

Table 5.1 shows the proportion of each observed flight pattern, for each wind direction. For 0^{o}, Visscher and Kopp (2007) observed just two types of flight pattern – autorotational and translational – using Tachikawa's terminology, where the translational mode occurred about three times more than the autorotational mode for this particular hold down force (or fixture strength integrity). By changing the wind direction from 0^{o} to 15^{o}, the proportion of the autorotational mode remains almost the same, while the number of translational mode flights is reduced. The remainder have shifted to the "3D Spinning" mode. This mode is not unexpected since the initial direction of the force on the panel is perpendicular to the surface, by definition, and not aligned with the mean flow direction

for this wind angle. This activates all six degrees of freedom, as shown by Richards et al. (2008).

Contrary to what might be expected, the "translational" mode appears to be more sensitive to the out of plane wind direction than the autorotational mode. Nevertheless, for the cornering wind angles, like 30° and 45°, 100% of the panels flew in the "3D Spinning" mode. Surprisingly, for the wind angles of 60°, 75°, and 90° the panel tends not to fly from the roof. 82% of the panels for the wind direction of 60° and all of the panels with the wind directions of 75° and 90° landed on the roof immediately after failure. The reasons for this will be examined later in the chapter.

5.3 Flight Trajectory Distances

The impact location of each test was obtained by using the two high speed cameras, one mounted on the ceiling and one placed beside the house, as explained in Chapter 3. Fig. 5.1 shows the impact location of the panels originating from the roof of the house for the wind directions of 0°, 15°, 30°, 45°, and 60°. The average, X_{avg} and Z_{avg} , and standard deviation, X_{σ} and Z_{σ}, of the longitudinal and lateral impact locations, respectively, are also presented in Table 5.1. The results for the wind direction of 0 degrees, presented in Fig. 5.1, are those of Visscher and Kopp (2007).

As Fig. 5.1 shows, the ground impact locations are scattered downstream of the house. For example, for a wind direction of 15°, the panels land between 20 – 70 m downstream of the house, while for 60° they land no further than 25 m downstream. There are several possible reasons for the range of values for both the mean and standard deviation of the flight distances including the variations of the (gust or mean) wind speed

at failure, wind turbulence in flight, mode of flight, turbulence and flow structure at the moments surrounding failure, and the angle between the mean wind direction and the normal to the panel.

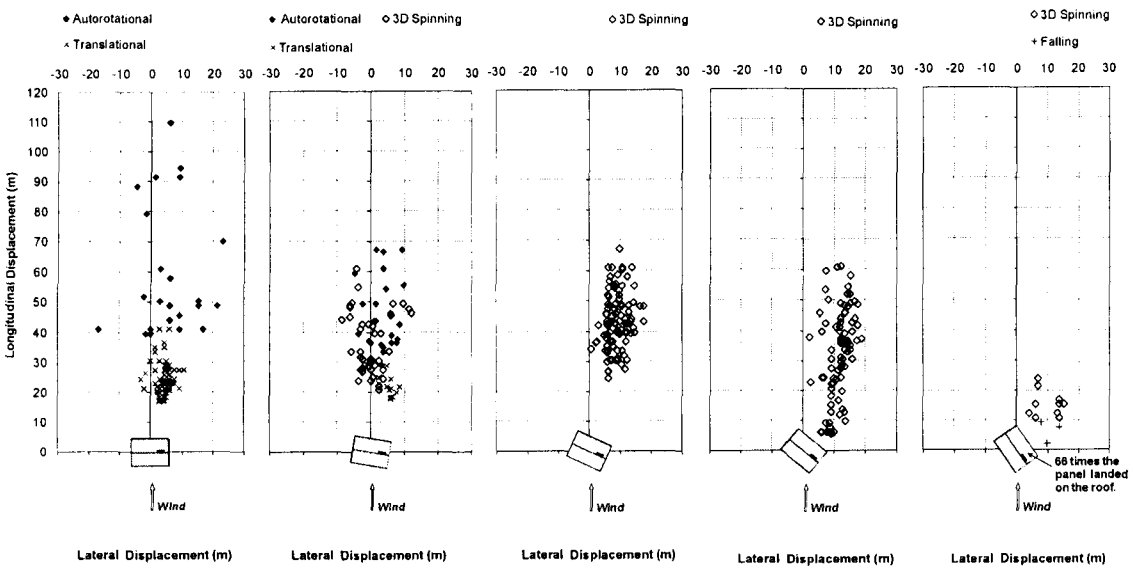

Fig. 5.1: Measured impact locations of the panels for the wind directions of (a) 0°, (b) 15°, (c) 30°, (d) 45°, and (e) 60°. The data for 0° are taken from Visscher and Kopp (2007).

In terms of mean flight distances, there appear to be, broadly speaking, two groupings. One is for 0° to 45°, where X_{avg} ranges from 31 – 43 m. The second group is for 60° to 90° where X_{avg} ranges from 0 – 13 m. There are differences in the scatter for all the wind angles examined, but in terms of the mean, this classification seems reasonable. Interestingly, these groups appears to be mostly unrelated to the failure wind speeds, with a range of $(U_H)_{avg}$ of 102 to 140 km/hr for the first group and 95 to 135 km/hr for the second. Thus, the use of uniform flow results and models (even with turbulence included)

cannot capture this effect, at least not without considering the effects of initial conditions on the roof in some way.

The scatter in the impact locations is also critical, because the furthest flight distances give the bounds of risk both in terms of impact locations and speeds. The X_σ results in Table 5.1 imply that the scatter is greater than what one would expect simply based on the turbulence levels in flight, although it is without a doubt that this contributes some of the scatter. For 0^o, with the same panel location, Visscher and Kopp (2007) attributed much of the scatter to the existence of different flight modes. They found that the translational mode spanned a range of 15 – 40 m, with the autorotational mode spanning 40 – 110 m. However, for 15^o, the differences caused by the change of modes are less obvious with little difference between the three modes, as classified. This suggests two things. First, effects of autorotation may only be relevant when the wind direction aligns with the normal to the panel, as it does for the current set-up for 0^o. Second, for the wind angles examined here (15^o – 90^o), flight mode identification is not really relevant and the panels move with all six degrees of freedom. Thus, for modeling, it may be that the autorotational force coefficients are not generally required (except for close to 0^o), and the use of only the static force coefficients may be reasonable. Additionally, the differences in the scatter for 15^o – 60^o (since for > 60^o the panel stays on the roof), as observed in Fig. 5.1, are due to other factors.

Fig. 5.2 depicts the impact locations as a function of the wind tunnel speed ($\hat{U}_H$). From this figure, it is clear that the variations in the mean wind tunnel speed for the experiments do not have an impact on the distribution of flight distances. Therefore, this can be removed as a factor contributing to the scatter.

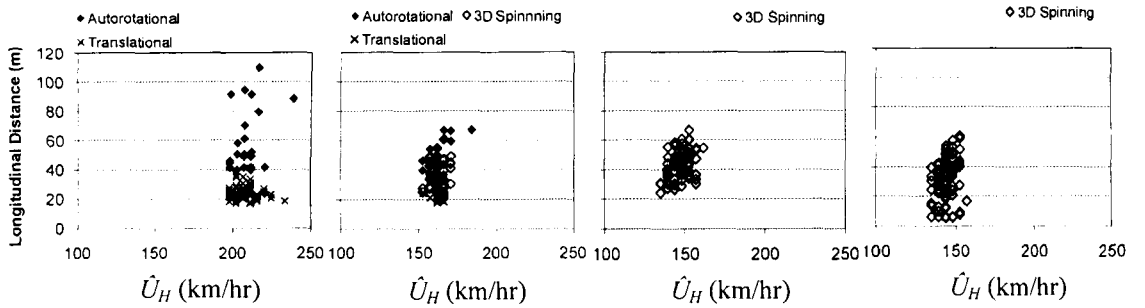

Fig. 5.2: The longitudinal impact as a function of failure velocity for the wind directions of (a) 0°, (b) 15°, (c) 30°, and (d) 40°. Note that the data for 0° is taken from Visscher and Kopp (2007).

Fig. 5.3 shows strobe images made from the digital videos for typical examples of the two types of flight for the wind direction of 60°, i.e., one example of 3D spinning and one where the panel did not leave the roof. In this case, the camera was observing the flight from above. From this figure, the role of the wind angle, as it relates to the panel angle, becomes apparent. Because the pressures acts normal to the surface, the initial impulse at failure is also normal to the surface so that initial panel motion is in the direction of the normal to the panel and not in the direction of the wind. Then, for panels which fly, they slowly re-align into the direction of the wind. For 45°, Fig. 5.1(d) shows that this leads to a scatter which is primarily in the streamwise (X) direction, with the shortest trajectories ending just downstream of the eaves edges in a straight line on the normal from initial panel location. In contrast the longer flights, land almost straight downstream of this as the wind direction controls beyond this point.

For 75° and 90°, none of the panels flew; rather, they all landed back on the roof immediately after failure. The panels with the wind direction of 75° either overturned and

landed on the roof upside down (like the example for 60° in Fig. 5.3b) or lifted from the long edge close the ridge and dropped back down. For 90°, the panels failed in uplift and subsequently fell back to the roof surface. Fig. 5.4 is a schematic sketch of the flow field above the panel for the wind directions in the range of 60° – 90°. Looking at the elevation of the gable end, the panel motion is approximately orthogonal to the wind but it stays in the separation bubble generated by the leading edge. This is illustrated in the section view so that the normal to the panel remains orthogonal to the wind when the panel is in position '2'. For this orientation, there is little aerodynamic force on the panel because of its alignment with the direction of flow and the relatively low speed flow in the bubble. Thus, the panels are unable to get into the high speed flow to move it downstream and to escape from the roof for these wind directions.

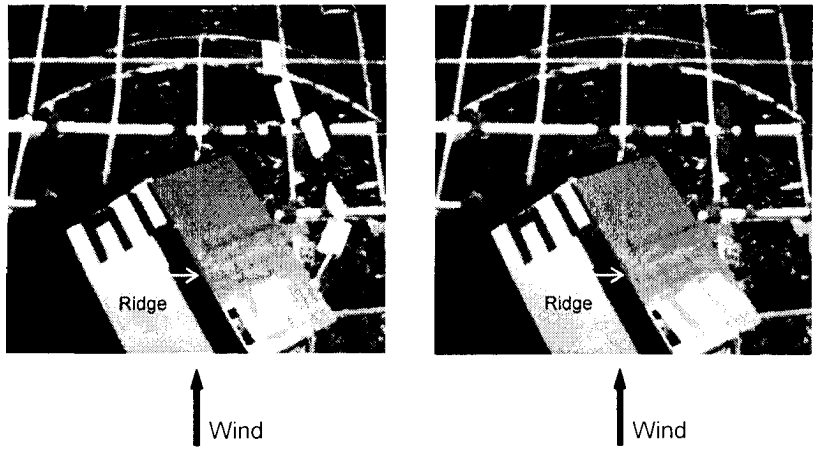

Fig. 5.3: Strobe images from overhead camera, looking down on the roof, typical of the (a) "3D Spinning" and (b) "no flight" patterns for a wind direction of 60°.

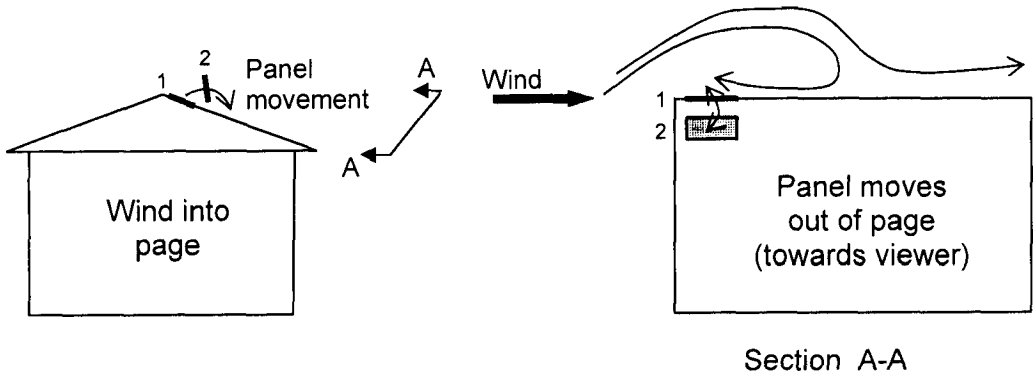

Fig. 5.4: Failure behaviour and initial movement of the panels, illustrating the flow pattern around the panel for wind directions of 60°, 75°, and 90°.

5.4 Flight Speeds

As mentioned in chapter 3, the horizontal (longitudinal), u, vertical, v, and lateral, w, velocities of the sheathing panels were obtained by differentiation of the curve fit to the panel trajectory. From this, the magnitude of the translational velocity, $u_{mag}=(u^2+v^2+w^2)^{0.5}$, was also obtained. All the values are non-dimensionalized according to Baker's (2007) formulation as described in chapter 4. Fig. 5.5 shows the results of $\bar{y}$, $\bar{u}$, $\bar{v}$, and $\bar{w}$ versus $\bar{x}$ for the sheathing panels with the wind directions of 15°, 30°,and 45°. The non-dimensional elevation of the eave and ridge heights are at $\bar{y}_{eave}$=0.16 and $\bar{y}_{ridge}$=0.2. Note that the non-dimensional horizontal and vertical distances of 1.4 and 0.3, respectively, which are limits of the plots, are equivalent to the horizontal and vertical distances of 55m and 12m, respectively. Note that when the panels flew out of the range of one of the cameras, we were not able to extract the entire trajectory; thus, for those tests, only a portion of the trajectory is presented.

From Fig. 5.5, several observations can be made: (i) The panels initially have a positive vertical velocity and elevate to about 25% above the ridge; (ii) The horizontal velocities of the panels are typically in the range of 30% - 90% of $\hat{U}_H$; (iii) The vertical and lateral velocity were much smaller in magnitude than the horizontal velocity and mostly less than 30% and 20% of $\hat{U}_H$, respectively.

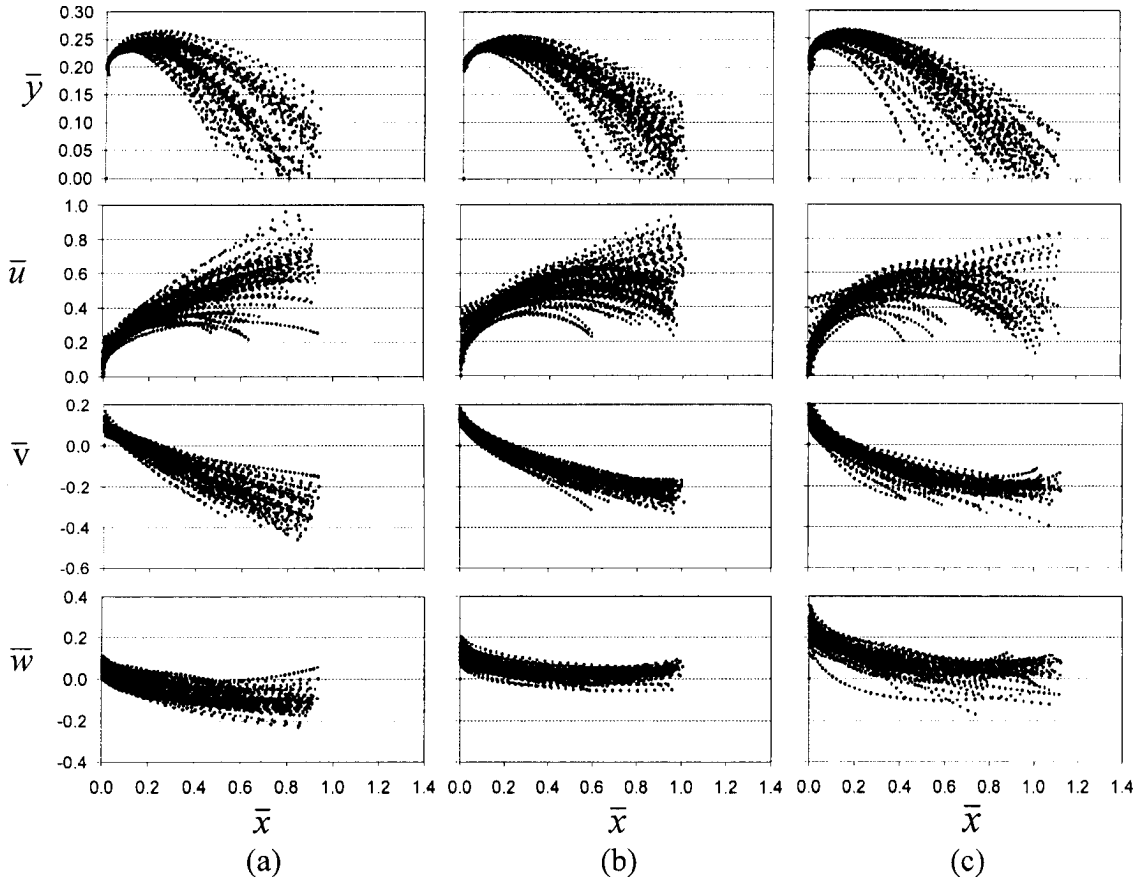

Fig. 5.5: Non-dimensional trajectories and the corresponding horizontal, vertical, and lateral velocity components of the panels for wind directions of (a) 15°, (b) 30°, and (c) 45°.

Wind direction affects the panel flight speeds in complex ways. For 15°, the horizontal speed is observed to (mostly) increase during the flight, with only a few decreasing towards the ground, as can be seen in Fig. 5.5. In contrast, the horizontal

velocity of the panels for 30° and 45° increases only to about $\bar{x}$ = 0.3 to 0.5 for all panels and after that point is either continuing to increase or decreases. Thus, there are two distinct patterns for $\bar{u}$. This appears to be an effect caused by the wake of the house so that the trajectories that are relatively shorter are disproportionately affected by the lower wind speeds in the wake and the panels slow down prior to impact with the ground. In contrast, panels which clear the most significant portion of the wake travel further and have continually increasing speeds – a point which is also observed for panels in a uniform stream.

The available energy for debris impacts is determined by the magnitude of the translational velocity during the flight. The translational velocities of the panels were investigated at two points, viz., eave height (on the way down) and ground level. Table 5.2 gives summary statistics of the non-dimensional velocities for panels at the eave height, $\bar{u}_{mag\text{-}eave}$, and at the ground level, $\bar{u}_{mag\text{-}ground}$, for wind directions of 15°, 30°, and 45°. The mean and standard deviation are included in the summary. As can be seen, the average of the translational speeds at the eave height is about 60% of the upstream 3 second gust speed for the panels with the wind direction of 15°, 30°, and 45°. It was also observed that the non-dimensional impact velocities at the eave height and ground level could be fitted to the lognormal probability distribution (not shown).

Table 5.2: Summary of the impact velocity results.

Wind Direction	$(\bar{u}_{mag\text{-}eave})_{avg}$	$(\bar{u}_{mag\text{-}eave})_{\sigma}$	$(\bar{u}_{mag\text{-}ground})_{avg}$	$(\bar{u}_{mag\text{-}ground})_{\sigma}$
15	0.58	0.14	0.73	0.21
30	0.61	0.11	0.58	0.24
45	0.58	0.08	0.43	0.20

5.5 Conclusions

The focus of the current work is on the flight of sheathing panels from the roof of a house in a realistic boundary layer flow with different wind directions. The failure velocity, flight trajectory, and translational velocity were studied in detail. As might be expected, complex relationships between the failure velocity, flight distance, translational velocity, and wind direction were observed. It is concluded that:

1- Three-dimensional spinning, with six degrees for freedom, is the most common type of flight patterns observed for the wind directions of 15^{o}, 30^{o}, and 45^{o}. This mode is similar to what Tachikawa (1983) and Visscher and Kopp (2007) labelled as "translational" for their nearly two-dimensional flights. The autorotational mode only appears when the normal to the initial plate location is aligned with the wind direction.

2- Almost all of the panels for wind directions of 60^{o} – 90^{o} landed on the roof immediately following "failure". This is because (i) the normal to initial panel location is perpendicular to the wind direction so that initial panel motion is also perpendicular to the wind, and (ii) these panels are located in the low speed region of the separated vortex on the roof and the direction and magnitude of wind speed does not provide significant aerodynamic force to the panels.

3- Panels with shorter trajectories, but which fly from the roof, are caught in the wake of the house so that the horizontal and net panel speed is dropping towards impact with the ground. Otherwise, they continue to increase all the way to impact.

4- Typical flight speed for panels range between 20% - 95% of the of the estimated roof height gust speed at failure.

References

Baker, C.J. (2007). "The debris flight equations." *J. Wind Eng. Ind. Aerodyn.* 95, 329-353.

Holmes, J.D., Letchford, C.W., and Lin, N. (2006). "Investigations of plate-type windborne debris- Part II : Computed trajectories." *J. Wind Eng. Ind. Aerodyn.* 94, 21-39.

Richards, P.J., Williams, N., Laing, B., McCarty, M., and Pond M. (2008). "Numerical calculation of the three-dimensional motion of wind-borne debris." *J. Wind Eng. Ind. Aerodyn.* 96, 2188-2202.

Tachikawa, M. (1983). "Trajectories of flat plates in uniform flow with application to wind-generated missiles." *J. Wind Eng. Ind. Aerodyn.* 14, 443–453.

Traczuk, G. (2007). "Trajectories of roof sheathing panels under high winds." Undergarduate thesis, The University of Western Ontario, Canada.

Visscher, B.T., and Kopp, G.A. (2007). "Trajectories of roof sheathing panels under high winds." *J. Wind Eng. Ind. Aerodyn.*, 95, 697-713.

6 CONSIDERATIONS FOR NUMERICAL MODELLING

Assessing "how far" and "how fast" windborne debris travels is a necessity for risk models of wind storms. Post event damage surveys from hurricanes do not provide any direct information on the speed of debris and provide only limited information regarding how far the debris travels, given the challenges of identifying debris sources, particularly, when wind directions change during a storm. Experiments provide information on both trajectory path and speeds of debris, but it would be impossible to conduct experiments for all possible scenarios. Therefore, the most efficient way to predict variation in debris flight is to have a numerical model that can predict the behaviour with sufficient accuracy, and which has been validated by experimental results.

The numerical model presented in Chapter 2 for the plate-like debris are based on uniform smooth flow, assuming that the plate travels with the gust that caused failure, and without applying the effects roof flow conditions and building wakes. It was also observed in Chapter 2 that the numerical solutions are able to provide excellent agreement with available experimental results in the literature which were also conducted in a uniform wind flow. In these experiments, the plates were released into the wind at particular initial angles of attack, without applying the effects of turbulence and initial flow conditions above the roof. Thus, the uniform, smooth flow conditions provide a unique trajectory result for a plate flying in a certain wind speed from a particular initial angle of attack. To explain the variation of trajectories observed in real situations, Tachikawa (1988) attributed the scatter to the different initial angles of attack and found the spatial variation to be uniformly distributed.

Unlike previous experiments, the experimental study presented in Chapters 4 and 5 were an attempt to capture the effects of turbulence, the wake generated by the 'source' building, and initial flow conditions on the roof for sheathing panels held down by nails. As such, results from uniform flow simulations have not been compared with this type of experimental data. The purpose of the present section is to make such comparisons.

6.1 Numerical Model

6.1.1 Roof Shingles

Based on the force coefficients presented in Chapter 2 for square plates, the non-dimensional asymptotic horizontal velocity of tiles is

$$\bar{u}_{asymptotic} = 1 - 0.263\sqrt{\frac{1}{Ta}} \tag{2.9a}$$

where Tachikawa Number, $Ta=(0.5\rho_{air}\cdot A\cdot \hat{U}_H^2)/m\cdot g$, and $\bar{u}_{asymptotic}$ is non-dimensionalized by the 3-sec gust wind speed at the mean roof height, $\hat{U}_H$. Since all of the tiles in the experiments had rotated clockwise, the associated non-dimensional asymptotic horizontal velocity is considered herein. The Tachikawa number (using $\hat{U}_H$) is in the range of 3.6-7.7 for the tile flights; thus, the non-dimensional, asymptotic, horizontal speed of the tiles is in the range of 0.86-0.9, based on Eq. (2.9a).

Likewise, by using the force coefficients presented in Chapter 2 for 2D plates, the non-dimensional asymptotic horizontal velocity of shingles can be calculated

$$\bar{u}_{asymptotic} = 1 - 0.51\sqrt{\frac{1}{Ta}} \tag{6.1}$$

Since all of the shingles in the experiments had rotated clockwise, the associated non-dimensional asymptotic horizontal velocity is considered herein. The Tachikawa number

(using $\hat{U}_H$) is in the range of 7.1-25.2 for the shingle flights; thus, the non-dimensional, asymptotic, horizontal speed of the shingles is in the range of 0.8-0.9, based on Eq. (6.1).

6.1.2 Roof Sheathing Panles

The two-dimensional numerical procedure presented in Chapter 2 is used herein to compare the numerical results with the current experimental results. In the numerical calculations, the static force coefficients are from the data presented by Richards et al. (2008) for plates with aspect ratio, $AR=l/B$, of 2. Thus, the static normal force coefficient, C_N, on the plate is assumed to be

$$C_N = \begin{cases} \dfrac{\alpha}{20^\circ} & \alpha \le 20^\circ \\ 1-0.1\dfrac{\alpha-20^\circ}{10^\circ} & 20^\circ < \alpha \le 30^\circ \\ 0.9+0.2\dfrac{\alpha-30^\circ}{30^\circ} & 30^\circ < \alpha \le 60^\circ \\ 1.1+0.1\dfrac{\alpha-60^\circ}{30^\circ} & 60^\circ < \alpha \le 90^\circ \\ 1.2-0.1\dfrac{\alpha-90^\circ}{30^\circ} & 90^\circ < \alpha \le 120^\circ \\ 1.1-0.2\dfrac{\alpha-120^\circ}{30^\circ} & 120^\circ < \alpha \le 150^\circ \\ 0.9+0.1\dfrac{\alpha-150^\circ}{10^\circ} & 150^\circ < \alpha \le 160^\circ \\ 1-\dfrac{\alpha-160^\circ}{20^\circ} & 160^\circ < \alpha \le 180^\circ \end{cases}$$

where α is angle of attack of the relative wind velocity to the plate. The normal force is resolved to yield the static lift, C_{LS}, and drag, C_{DS}, components. An additional drag coefficient of 0.1 is assumed as the effect of the skin friction component. Thus,

$$C_{LS} = C_N \cos(\alpha)$$

$$C_{DS} = 0.1 + C_N \sin(\alpha)$$

Based on Richards et al.'s (2008) results for the plates with AR of 4, the center of pressure, c, is assumed to be at

$$\frac{c}{l} = 0.25 - \frac{\alpha}{2\pi}$$

so that the static moment coefficient, C_{MS}, can be calculated as

$$C_{MS} = \frac{c}{l} \cdot C_N$$

Based on Tachikawa (1983), the rotational drag, C_{DR}, lift, C_{LR}, and moment, C_{MR}, are defined in terms of S/S_0 so that

$$C_{DR} = \begin{cases} 1.16\left|\frac{S}{S_0}\right| & \left|\frac{S}{S_0}\right| \le 0.4 \\ 0.465 + 0.108\left(\left|\frac{S}{S_0}\right| - 0.4\right) & 0.4 < \left|\frac{S}{S_0}\right| < 1 \\ 0.53 & \left|\frac{S}{S_0}\right| \ge 1 \end{cases}$$

$$C_{LR} = \begin{cases} 0.0395 + 0.7505\frac{S}{S_0} & 0.6 < \frac{S}{S_0} \\ 0.0727 + 0.6952\frac{S}{S_0} & 0.1 \le \frac{S}{S_0} \le 0.6 \\ 1.422\frac{S}{S_0} & -0.1 \le \frac{S}{S_0} \le 0.1 \\ -0.0727 + 0.6952\frac{S}{S_0} & -0.6 \le \frac{S}{S_0} \le -0.1 \\ -0.0395 + 0.7505\frac{S}{S_0} & \frac{S}{S_0} < -0.6 \end{cases}$$

$$C_{MR} = \begin{cases} 0.32\left(1 - \frac{S}{S_0}\right) & \frac{S}{S_0} > 1 \\ 0.32\left(1 - \left|\frac{S}{S_0}\right|\right)\left(\frac{S}{S_0}\right) & 0 \le \left|\frac{S}{S_0}\right| \le 1 \\ -0.32\left(1 + \frac{S}{S_0}\right) & \frac{S}{S_0} < -1 \end{cases}$$

where S_0 for a three-dimensional (3D) plate is defined based on Eq. (2.6).

Therefore, using the numerical procedure described in Chapter 2 with the force coefficients described above, the non-dimensional asymptotic horizontal velocity for plates with $AR = 2$ is

$$\bar{u}_{asymptotic} = 1 - 0.42\sqrt{\frac{1}{Ta}} \tag{6.2}$$

Since all of the sheathing panels in the experiments rotate clockwise (for flow from left to right), the associated non-dimensional asymptotic horizontal velocity is considered herein. The Tachikawa number (using $\hat{U}_H$) is in the range of 4.2-5.3 for the panel flights, with the wind directions of 15°, 30°, and 45°; thus, the non-dimensional, asymptotic, horizontal speed of the panels is about 0.8, based on Eq. (6.2).

6.2 Numerical Results and Considerations

6.2.1 Roof sheathing Panels

The numerical model predictions presented in Chapter 2 closely matched a range of experimental results in uniform, smooth flow, so the method is helpful for assessing the effects of initial conditions and in-flight velocity fields on the trajectories. Since the majority of the flight patterns observed for panels with the wind directions of 0° and 15° are basically two-dimensional, the results of numerical calculations for these two wind directions are considered herein. Clearly, uniform, smooth flow results are unable to predict the situations where no flight is observed following failure, as occurs for wind directions greater than 60° in the current panel and roof configuration. An initial angle of attack of 20° was applied in the present calculations, close to the value of the roof slope of 18.5°, although the effects of this are examined further below.

The mean values of the 3-sec gust speeds (i.e., failure wind speeds) at the mean roof height for the wind directions of 0^{o} and 15^{o} wind directions are 56 and 45 m/s, respectively. Using these two speeds in the numerical calculations yields ground impact locations of x = 175 and 100 m, respectively. These values are much higher than the upper bound of the observed longitudinal impact locations for the wind directions of 0^{o} and 15^{o}, implying that the combination of the effects of initial conditions, boundary layer wind flow, and wake behind the house all reduce the maximum below the uniform, smooth flow result for debris of this size.

Fig. 6.1(a) shows the numerical results of a panel flying with a speed of 45m/s along with all of the experimental data for the wind direction of 15^{o}. The end of the numerical curve is impact with the ground. As can be seen, the calculated horizontal panel velocity provides an upper bound to the experimental panel speeds (although a few panels travel faster, perhaps implying higher wind speeds for those cases). This indicates that the assumed 3 sec gust speed represents a practical and reasonable average as upper-bound flow speed along these trajectories. However, as Fig. 6.1(b) shows, the numerical vertical panel velocity is much smaller in magnitude than the experimental vertical velocities, which are negative (i.e., the plates are falling). This is why the uniform flow calculations over-estimate the impact locations, as compared to the experimental results. As a result, Fig. 6.1(a) shows that the uniform smooth flow calculations are much better at estimating the upper bound of the debris horizontal speeds than the impact locations.

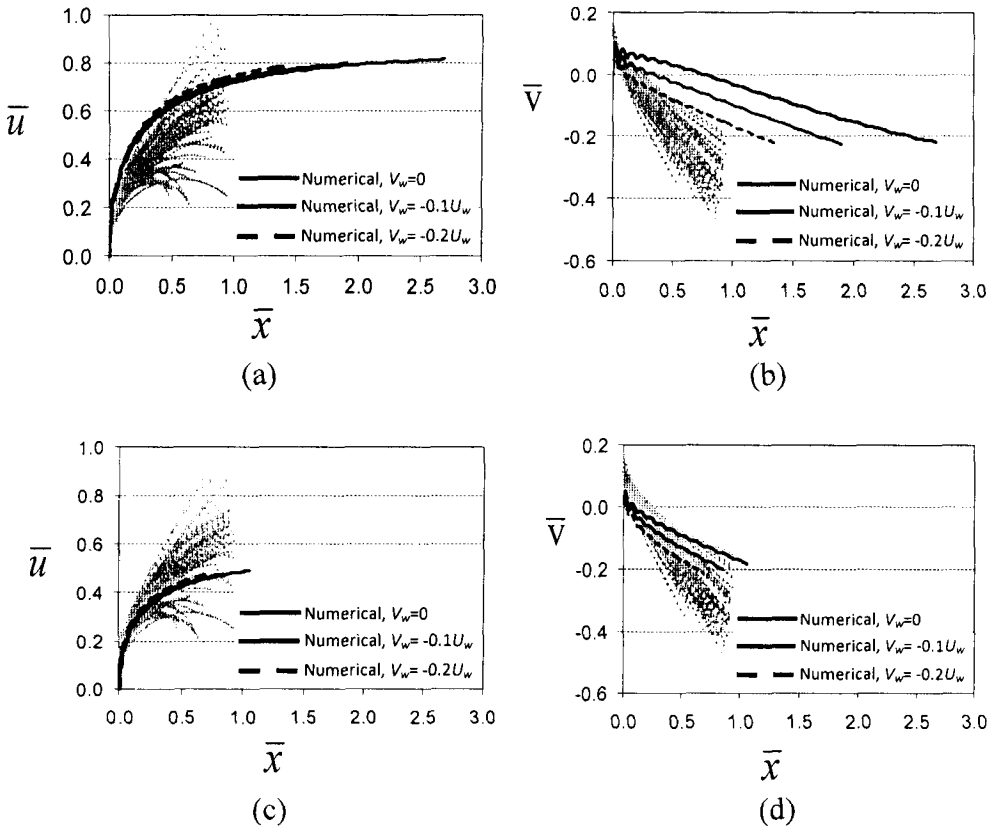

Fig. 6.1: Non-dimensional horizontal and vertical velocities versus horizontal distance for wind direction of 15°, ▲ ; (a-b) Non-dimensional horizontal and vertical velocity for a panel flying in a uniform, smooth flow with 3 sec gust speed of 45m/s and with three downward vertical wind velocities; (c-d) Non-dimensional horizontal and vertical velocity for a panel flying in a uniform, smooth flow with 10-min mean wind speed of 32m/s and with three downward vertical wind velocities.

In the real wind flow, the vertical wind velocity, V_w, is not zero along the typical panel trajectories, particularly in the wake of the house, and should be significantly negative as the flow reattaches. However, in the numerical calculations, the vertical wind speed was assumed to be zero, causing the over-estimation of the impact location. Thus, two additional vertical wind speeds were considered. Fig. 13(a) shows the numerical results again using a horizontal wind speed of 45m/s but with two downward vertical wind

velocities, namely 10% and 20% of the horizontal wind speed. As expected, the computed vertical velocity of the panel and consequently the impact location were decreased. For instance, the impact locations of the panels flying in winds with speeds of 56 and 45 m/s, with the downward vertical wind speed for 20% of the horizontal wind speed, were decreased to 80m and 55m, respectively.

Following Tachikawa (1988), the effect of initial angle of attack is also examined. Varying the initial angle of attack in the range of $0^{o} - 55^{o}$ was found to yield a vertical velocity with the same trend as that of experimental results. The variation in the initial angle of attack mostly affects the vertical panel velocity, consequently changing the impact location. For example, the impact location for the panels travelling with speeds of 56 and 45 m/s, with the initial angle of attack in the range of $0^{o} - 55^{o}$, is found to be in the range of 175-120m and 100-65m, respectively.

Due to the response time of the panels, as well as effects of the initial flow conditions and the flow field in the wake of the house, it is also possible that the sheathing panels missed the gust and flew in an average wind speed that is substantially lower than the assumed 3-sec gust wind speed. A lower bound of the wind speed, not considering wake effects, would be the mean (10 min) speed. For wind directions of 0^{o} and 15^{o}, the observed 10-min (failure) wind speeds were 39 and 32 m/s, respectively. Using the numerical procedure, the impact locations for the panels with these speeds are 70 and 42 m, respectively. Fig. 6.1(c) shows the numerical results for a sheathing panel flying in a uniform, smooth 32 m/s wind, along with the experimental results, for the wind direction of 15^{o}. To match the numerical results with the presented experimental results, the numerical translational velocity is non-dimensionalized by the associated 3-sec gust

speed, which is 45m/s in this case. Again, the end of the numerical curve is impact with ground. As can be observed, the numerical horizontal velocity provides something approaching a lower bound to the horizontal velocity data. The numerical results for a panel flying with the 10-min horizontal wind speed and two downward vertical wind velocities, namely, 10% and 20% of the horizontal wind speed, are also shown in Fig. 6.1(c,d). As shown previously, the computed vertical velocity of the panel and consequently the impact location were decreased. The impact locations of the panels flying in the wind speed of 39 and 32 m/s, with a downward vertical wind speed of 20% of the horizontal wind speed, were decreased to 40m and 26m, respectively.

Thus, to obtain the range of the horizontal speed of debris for this particular configuration and wind directions of 0^o – 15^o, it appears reasonable to use the uniform flow results with horizontal wind speeds in the range from the mean (10 min) to 3 sec gust speed. However, the range of the impact locations is sensitive to the local flow field (above the roof, especially when they don't fly; and wake, when they do fly). It seems unlikely that numerical modelling will be able to successfully model generally the range of trajectories without much greater knowledge of the flow fields around source structures.

6.2.2 Roof Tiles and Shingles

Looking at Fig. 4.9 indicates that the tiles velocity tends to increase continuously during the trajectory while almost half of the shingles have reached to their asymptotic velocity. This is also consistent with the point was made earlier in Chapter 2 that plate debris elements flying longer than $\bar{x} \sim 3$ are expected to reach to the asymptotic limit. This

is equivalent to $176m$, $27m$ in full scale for tiles and shingles, respectively. The longest impact location for the tiles experiments was at the point $\bar{x}$ ~2 (Fig. 4.3).

As discussed before, the shingle flights in undisturbed wind speeds are in the range from the 3-sec gust speed to the 10-min gust speed. The 3-sec gust speeds associated with the shingle tests are mostly in the range of 90-165 km/hr, thus, the 10-min mean speeds are in the range of 60-115 km/hr (based on ASCE 7-05). Fig. 6.2(a,b) shows the numerical results for a shingle flying in uniform flow with a 3-sec gust speed of 165 km/hr, as an upper limit, and Fig. 6.2(c-d) shows the numerical results for a shingle flying in uniform flow with a 10-min gust wind speed of 60 km/hr (at roof height), as a lower limit. As discussed before, the effect of a downward vertical wind velocity of 20% of the horizontal velocity is also shown in the figures. The end of the numerical curve is impact with ground. Since all of the shingles tests have rotated clockwise, the results related to the clockwise rotation with an initial angle of attack of 30^{o} are chosen here. To have the numerical results matched with the presented experimental results, the numerical translational velocity is non-dimensionalized by the associated 3-sec gust speed. The associated 3-sec gust speed for the lower limit is 90 km/hr. As the figures show, it appears reasonable to use the uniform flow results with horizontal wind speeds in the range from the mean (10 min) to 3 sec gust speed to predict the range of the horizontal speeds. On the other hand, the uniform flow calculation over-estimates the range of impact locations. This can be modified by considering a downward vertical wind velocity throughout a debris trajectory.

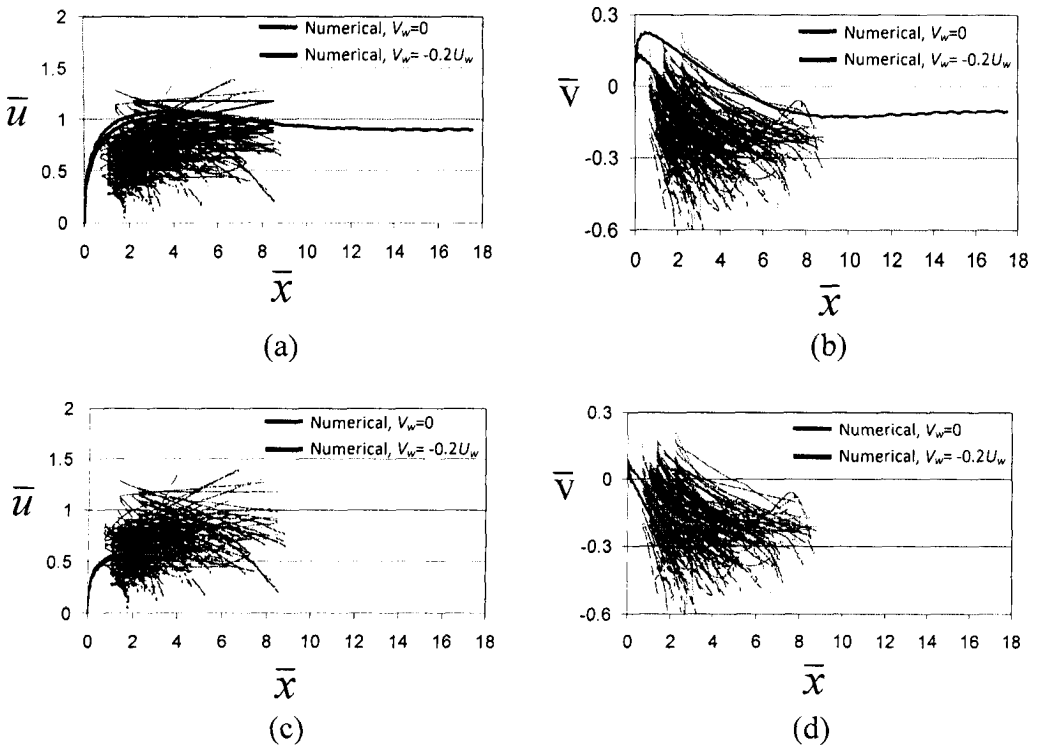

Fig. 6.2: Non-dimensional horizontal and vertical velocities versus horizontal distance for all of the shingle tests, ▲ ; (a-b) Non-dimensional horizontal and vertical velocity for a shingle flying in a uniform, smooth flow with 3 sec gust speed of 165 km/hr and with two downward vertical wind velocities; (c-d) Non-dimensional horizontal and vertical velocity for a shingle flying in a uniform, smooth flow with 10-min mean wind speed of 60m/s and with two downward vertical wind velocities.

6.3 Conclusions

For the configurations studied here, it appears that tiles do not reach to their asymptotic limit, while the vast majority of shingles probably fly at the asymptotic limit over a significant portion of their trajectory. It was also observed that some of the sheathing panels reach to their asymptotic limit.

In all tests, the sheathing panels are observed to travel on shorter trajectories compared to those estimated by uniform, smooth flow computations with similar 3-sec gust speeds. However, the uniform smooth flow calculations appear to be useful for determining panel speeds. It appears from the numerical analysis that the average horizontal wind speeds along the panel trajectories is in range from the 10-min mean wind speed to the 3-sec gust speed at the mean roof height. It was also observed that the addition of a downward vertical wind speed of about 20% of the horizontal wind speed to the numerical calculations improves the numerical predictions of the trajectory length for the particular panel location investigated here. The same observation was also made for shingles.

References

ASCE 7-05, Minimum Design Loads for Buildings and Other Structures, American Society of Civil Engineers, Reston, Virginia, 2005.

Richards, P.J., Williams, N., Laing, B., McCarty, M., and Pond M. (2008). "Numerical calculation of the three-dimensional motion of wind-borne debris." *J. Wind Eng. Ind. Aerodyn.* 96, 2188-2202.

Tachikawa, M. (1983). "Trajectories of flat plates in uniform flow with application to wind-generated missiles." *J. Wind Eng. Ind. Aerodyn.* 14, 443–453.

Tachikawa, M. (1988). A method for estimating the distribution range of trajectories of wind-borne missiles, Journal of Wind Engineering and Industrial Aerodynamics, vol. 29, pp. 175-184.

7 CONCLUSIONS AND RECOMMENDATIONS

7.1 Conclusions

In the numerical part of the work, a quasi-steady model to predict the trajectories and speeds of wind-driven 3D plates was suggested. The model incorporates the effects of rotational lift, drag, and pitching moment using single degree of freedom autorotation data for thin plates. There are four independent non-dimensional parameters which are required to determine the trajectory of windborne plate debris. It was observed that plate rotational speeds are not well predicted by the quasi-steady model when these speeds are large, such as occurs during falling in a still fluid. However, the trajectories when the plates are dominated by a uniform free stream show excellent agreement when compared with existing experimental data. An important aspect is that the rotational drag plays a significant role and should be included in the model. In fact, the developed model captured the physics sufficiently in order that some of the scatter observed in the experimental data of Lin et al. (2006) could be explained via the model. Additionally, it was shown that the initial horizontal plate speeds are largely dependent on the buoyancy parameter, φ, so that non-dimensionalization of spatial coordinates with this parameter collapses the data well in the early stages of flight. The asymptotic limit at large times showed that wind-driven plates will always rotate, the direction of which is determined in a complex way by the four governing parameters.

In the experimental part of the work, the flight of roof tile, shingle, and sheathing panel originating from a typical house in typical neighbourhoods, is examined. Earlier research has primarily focussed on the three degree-of-freedom flight of debris elements

in uniform, smooth flow, but, the objective of the present work is to determine how realistic initial conditions, surroundings, and turbulence affect the flight of two common types of 'plate' debris. Details on the modes of flight, distance travelled and flight speeds were examined for a range of initial locations, hold down forces and wind angles. As might be anticipated, given the large number of parameters governing the problem, there are complex relationships between initial location on the roof, hold down force, failure wind speed and flight distance. The main conclusions of the work are:

- Three-dimensional spinning flight was by far the most common mode of flight. Relatively few cases were observed where the primary rotation was aligned to cause additional lift through the Magnus effect.
- The second most common mode of flight, following failure, is for the element not to fly from the roof. This is due to the flow field at the point of failure being governed by the building aerodynamics. For example, (i) many of the tiles and shingles located at the flow separations and reattachments above the roof remain on the roof after failure. This is because the flow below the separation streamline is a vortex with the flow near the roof surface being in a direction against the main stream. In this local flow field, flight of elements is often not possible. (ii) Almost all of the sheathing panels for wind directions of 60^{o} – 90^{o} landed on the roof immediately following "failure". This is because these panels are located in the low speed region of the separated vortex on the roof and the direction and magnitude of wind speed does not provide significant aerodynamic forces to the panels.

- In situations where shingles are able to escape from the separation region, they move upstream and get caught up in the high speed flow associated with the separated shear layer near the point of flow separation. In this case, high speed, high elevation, trajectories are observed.
- Because of the effects of the flow field above the roof, the debris failing in the highest wind speeds did not always travel the furthest.
- Debris that travels higher, also travels faster and further. In general, debris initiating from a building with no structures upstream results in a higher, longer, and faster trajectory.
- Debris with a higher fixture strength integrity, from a particular location, travels farther.
- Sheathing panels with shorter trajectories, but which flew off of the roof, were caught in the wake of the house so that the horizontal and net panel speed was dropping towards impact with the ground. Otherwise, they continued to increase, all the way to impact. However, sheathing panels, with the current hold down force and thickness, did not reach the asymptotic limiting speeds.
- The typical flight speeds range for shingles is between 50 – 120% of the estimated, mean roof height, (undisturbed) gust speed at failure. For tiles, the range is 30 – 60% and for sheathing panels the range is 30 – 90%.
- It was shown that shingles which travel the same dimensional distances as sheathing panels gain higher flight speed.
- The response time of the tiles and sheathing panels was much lower than the integral time scale of the upstream flow at the mean roof height while the

response time of the shingles is higher than the integral time scale of the upstream flow at the mean roof height, in the current experiment. Thus, none of the tiles and sheathing panels, but many of the shingles, tended to travel with the gust.

- For the configurations studied here, it appears that the vast majority of shingles probably fly at the asymptotic limit over a significant portion of their trajectory. However, tiles and sheathing panels do not. This is the result of the different response times of these elements.
- In all tests, the sheathing panels are observed to travel on shorter trajectories than those estimated by uniform, smooth flow computations with similar 3-sec gust speeds. It appears that, for panels which are aligned with the wind direction (0^{o}-15^{o} in the current case), the 10-min mean wind speed represents an effective average value to give equivalent impact locations, both for auto-rotational and translational flight modes. The effects of the initial panel orientations, combined with house wake effects, limits the use of the uniform, smooth flow results for more oblique wind angles (60^{o}-90^{o} in the current case).

•For the configurations studied here, it appears that tiles do not reach to their asymptotic limit, while the vast majority of shingles probably fly at the asymptotic limit over a significant portion of their trajectory. It was also observed that some of the sheathing panels reach to their asymptotic limit.

•In all tests, the sheathing panels are observed to travel on shorter trajectories compared to those estimated by uniform, smooth flow computations with similar 3-sec gust speeds. However, the uniform smooth flow calculations

appear to be useful for determining panel speeds. It appears from the numerical analysis that the average horizontal wind speeds along the panel trajectories is in range from the 10-min mean wind speed to the 3-sec gust speed at the mean roof height. It was also observed that the addition of a downward vertical wind speed of about 20% of the horizontal wind speed to the numerical calculations improves the numerical predictions of the trajectory length for the particular panel location investigated here. The same observation was also made for shingles.

7.2 Recommendations

The numerical work presented in this study looked at the two-dimensional flight of plate debris. It is mostly applicable to debris flying in a uniform wind flow when the wind direction is aligned with the normal to the plate. As observed herein, the debris flight is mostly three-dimensional in a realistic situation. To better predict the flight of such debris, (i) a model of static and rotational forces on a plate with six degrees of freedom is required (This was done to some extent by Richards et al. (2008)); (ii) The effect of the initial condition (e.g., local velocity, initial hold down force) should also be modelled. As shown before, the initial flight of the debris is governed by the initial conditions while the flight afterward depends on the aerodynamics of the debris. To apply the effects of the initial conditions to the flight model we need to understand how and when the forces from phase I (initial condition) should be transformed to forces in phase II (aerodynamics of the debris). To apply the effect of initial condition further investigation of the problem is required.

The experimental study conducted herein is useful to address the complication of the three-dimensional flight of plate debris originated from a gable roof model house in a realistic boundary layer flow. It should be emphasized that the failure mechanism of the tile and shingle tests were not modelled in the current study. It is also important to realize that the impact locations and translational velocities of the debris presented herein do not show the trends and effects of any other combinations or arrangements.

During each experiment presented herein, the 10-min mean wind speed was measured, not the wind velocity at the time of failure. The failure wind velocity was assumed to be the 3-sec gust speed and was estimated based on Durst research (ASCE 7-05). To measure the failure wind speed, we need to conduct a simultaneous series of time-resolved PIV experiments with the failure model test in place.

Moreover, the pressure distribution around the model debris at the time of failure has never been investigated. To do a more thorough investigation, a simultaneous series of time-resolved PIV experiments with failure model test and pressure measurement around the debris can be conducted.

References

ASCE 7-05, Minimum Design Loads for Buildings and Other Structures, American Society of Civil Engineers, Reston, Virginia, 2005.

Lin, N., Letchford, C., and Holmes, J.D. (2006). "Investigation of plate-type windborne debris. Part I. Experiments in wind tunnel and full scale." *J. Wind Eng. Ind. Aerodyn.* 94, 51-76.

Richards, P.J., Williams, N., Laing, B., McCarty, M., and Pond M. (2008). "Numerical calculation of the three-dimensional motion of wind-borne debris." *J. Wind Eng. Ind. Aerodyn.* 96, 2188-2202.

APPENDIX I

- Permission from the ASCE journal of Engineering Mechanics for reuse.

From: PERMISSIONS

To: Bahareh Kordi

Sent: Thursday, December 17, 2009 6:59 AM

Subject: RE: permission-reuse author's own material

Dear Bahareh Kordi:

Permission is granted for you to reuse "Evaluation of the quasi-steady theory applied to windborne flat plates in uniform flow" in your doctoral dissertation. Please add a full credit line to the material being reprinted: With permission from ASCE.

Xi Van Fleet
Senior Manager, Information Services
Publication Division
American Society of Civil Engineers
1801 Alexander Bell Drive
Reston, VA 20191
(703) 295-6278-FAX
PERMISSIONS@asce.org

From: Bahareh Kordi
Sent: Wednesday, December 16, 2009 1:26 PM
To: PERMISSIONS
Subject: permission-reuse author's own material

Dear Sir/Madam,

I have published an article in the ASCE Journal of Engineering Mechanics and I would like to reuse my paper in my doctoral thesis.
It is written in the ASCE's website that by using the Rightslink one can obtain an instant permission for reuse of his/her own work. Unfortunately, after using Rightslink, I receive the following message: " The order details you specified are not permitted for licensing by ASCE."

Would you please tell me how I can obtain a permission for reusing my own paper in my doctoral thesis. The information about my paper is as follow:
- Kordi, B., and Kopp, G.A. (2009). "Evaluation of the quasi-steady theory applied to windborne flat plates in uniform flow" ASCE J. Eng. Mech., 135, No. 7, 657-668.

Regards,
Bahareh Kordi